

Alma Mater Studiorum – Università di Bologna

DOTTORATO DI RICERCA IN
ASTRONOMIA

Ciclo XXIV

Settore Concorsuale di afferenza: 02/C1

Settore Scientifico disciplinare: FIS/05

TITOLO TESI

An optimal estimator for the correlation of CMB anisotropies
with Large Scale Structures and its application to WMAP-
7years and NVSS

Presentata da: FRANCESCA SCHIAVON

Coordinatore Dottorato

Chiar.mo Prof.
Lauro Moscardini

Relatore

Chiar.mo Prof.
Gabriele Giovannini

Co-relatori:

Dott. Fabio Finelli
Dott. Alessandro Gruppuso

Esame finale anno 2012

This thesis has been carried out
at INAF/IASF-Bologna as part of
the institute research activity.

Contents

1	The cosmological model	7
1.1	Standard Hot Big Bang model	7
1.2	Thermal history of the Universe	10
1.3	The Dark Energy models	13
1.3.1	The cosmological constant	14
1.3.2	Chaplygin-type gas	15
1.3.3	Quintessence	16
1.3.4	Modified Gravity	17
1.4	Observational evidences for Dark Energy	18
1.4.1	Type Ia Supernovæ	18
1.4.2	Baryonic acoustic oscillations (BAO)	19
1.4.3	Gravitational lensing	20
1.5	Inflation	21
1.5.1	Horizon Problem	21
1.5.2	Flatness problem	22
1.5.3	Monopole problem	23
1.6	Cosmological perturbation theory	23
1.6.1	Metric perturbations	24
1.6.2	Structure formation	25
1.6.3	Non-linear perturbations	26
2	Cosmological Microwave Background	29
2.1	Primordial anisotropies	30
2.1.1	Acoustic peaks	32
2.2	Polarization	36
2.3	Secondary anisotropies	38

2.3.1	Gravitational Secondaries	39
2.3.2	Scattering Secondaries	42
2.3.3	Foregrounds	44
3	Late Integrated Sachs-Wolfe Effect	45
3.1	Cross-correlation	47
3.2	Information on Dark Energy constraint in the ISW-LSS cross-correlation	52
4	CMB and LSS data	61
4.1	Cosmic Microwave Background Data	61
4.2	Large Scale Structures Data	62
4.3	NVSS	64
4.3.1	Systematics and pre-processing	65
4.3.2	Source redshift distribution	69
4.3.3	Shot noise	73
5	BolISW code	75
5.1	QML algebra	75
5.2	<i>BolPol</i>	77
5.3	<i>BolISW</i>	78
5.3.1	Numerical optimization	80
5.4	Validation	82
6	Application to WMAP 7 year and NVSS data	91
6.1	TT auto-spectrum	91
6.2	Galaxy distribution model with constant b	91
6.2.1	No shot-noise removal	92
6.2.2	Shot-noise removal	93
6.2.3	Declination correction	94
6.2.4	$C_\ell^{TG} \neq 0$ effect on the cross-power spectrum	95
6.3	Galaxy distribution model with $b(z)$	95
7	Quantitative assessment of the cross-correlation detection	109
7.1	Likelihood computation	109

<i>CONTENTS</i>	1
7.2 Results	110
A Fisher matrix	125

Introduction

The understanding of the nature of dark energy is one of the outstanding question for observational cosmology. Since the discovery of the present acceleration of the Universe by the measurement of the luminosity distance of distant type Ia supernovæ (SN Ia) ([Riess et al.1998, Perlmutter et al.,1999]), several observations have sharpened a cosmological concordance model in which an unknown component - dark energy - with a negative pressure density shares $\sim 2/3$ of the total energy budget of the Universe ([Tegmark et al.2004]). At present the nature of dark energy can be hardly constrained by different cosmological observations, with the main indication that its parameter of state w_{DE} is close to a cosmological constant's one. The key strategy to constrain the nature of dark energy with current data is to combine as many different observations as possible, as luminosity distance of SN Ia, baryonic acoustic oscillations (BAO) from galaxy surveys, Cosmic Microwave Background (CMB) anisotropies, weak lensing surveys, etc ...

One of the key predictions of the presence of dark energy is the late Integrated Sachs Wolfe effect (Sachs & Wolfe 1968) in the CMB pattern. The ISW effect is a contribution to CMB anisotropies caused by the gravitational interaction of the CMB photons with the forming large scale structures. It is related to a time evolving gravitational potential, as occurs on large scales when the Universe enters in a late accelerated expansion (late ISW). The late ISW is a small contribution to the total CMB anisotropies and is maximum on the largest scales (Kofman & Starobinsky 1985), but therefore blurred by cosmic variance: however it can be detected by its cross-correlation with large scale structures (LSS) (Crittenden & Turok 1995) and this non vanishing cross-correlation is an independent probe of dark energy, complementary to the distance to the last scattering surface which fixes the position of the acoustic peaks in the angular power spectrum of CMB anisotropies.

In the current era of precision cosmology, an accurate analysis of the CMB-

LSS cross-correlation and a scientifically soundful cosmological interpretation are required, despite its modest signal-to-noise ratio (SNR), the quality of current data and data analysis issues. Until now there is no consensus among results in literature, then we choose to use the best look on the ISW-LSS cross-correlation by using an optimal method.

In this thesis we present the implementation of a quadratic maximum likelihood (QML) code, ideal to estimate the ISW-LSS cross-power spectrum, together with the auto-power spectra of CMB and LSS: such tool goes beyond all the previous harmonic analysis of the ISW-LSS cross-power spectrum present in the literature.

The thesis is divided into the following chapters.

- The first chapter deals with the basic concepts of the current cosmological model, starting from the Big Bang theory to pass through Dark Energy observational evidences and models. It will be introduced the Inflation models and reviewed the cosmological perturbation theory.
- The second chapter will focus on the CMB anisotropies, we will start from primordial ones and then we will report all the secondary anisotropies, including the ISW effect. We will obtain the temperature power spectrum from the perturbation equations of a relativistic fluid, in order to take into account the most important features of the spectrum and their cosmological implications.
- The third chapter will be entirely dedicated to the ISW effect. We will derive the cross power spectrum from the LSS matter density (δ_g) and CMB temperature ($\Delta T/T$) cross-correlation. We will report the ISW detection history, the current controversy on the statistical significance of the ISW-LSS cross-correlation, generated by several different results which span from no detection at all to a positive at a maximum of 4.5σ .
- The fourth chapter deals with the real map description of CMB temperature (WMAP-7year) and galaxy distribution (NVSS) which will be used in Chap.(6) analysis. We will introduce the shotnoise and one of the systematics in the LSS map. We will describe two different galaxy distributions which could characterize the NVSS map.

- The fifth chapter deals with the QML method to estimate the cross correlation ISW-LSS, going into a detailed description of the algebra. We will report the implementation of the BolISW code based on the QML method and its Monte Carlo validation with 1000 WMAP7-like and NVSS-like simulated maps.
- The sixth chapter deals with the applications of the BolISW code on real data. We will show the estimates for all the three power spectra (temperature-temperature, temperature-galaxy and galaxy-galaxy correlations), comparing also estimates from different galaxy distribution models.
- The seventh chapter deals with the quantitative assessment of the cross-correlation detections by using three different likelihood perspectives. We will give constraints on the Ω_Λ parameter, fixing all the other cosmological parameters. We will compare our results with other ISW-LSS signal detections.

Throughout the whole thesis, natural units $c = \hbar = 1$ are assumed.

Chapter 1

The cosmological model

Today the concordance cosmological model is the Λ CDM (Cold Dark Matter) model, based on the Einstein's relativity and taking into account the ideas of the Standard Hot Big Bang model, the presence of the Dark Matter and the Dark Energy and the Inflation model. The observations have on many occasions been in disagreement with the previously accepted theory, leading to the subsequent replacement or addition of the standard model.

1.1 Standard Hot Big Bang model

The Standard Hot Big Bang model suggests a homogeneous, isotropic Universe whose evolution is governed by the Friedmann equations based on Einstein's General Relativity and the Copernican principle.

All the informations about matter density and the geometry of the Universe are contained in the Einstein field equations

$$G_{\mu\nu} \equiv R_{\mu\nu} - \frac{1}{2}Rg_{\mu\nu} = 8\pi GT_{\mu\nu} \quad (1.1)$$

where $G_{\mu\nu}$ is the Einstein tensor, which describes the space-time geometry through the metric tensor $g_{\mu\nu}$, the Ricci tensor $R_{\mu\nu}$ and Ricci scalar R , depending on metric derivatives; the other side of the equation contains the stress-energy tensor $T_{\mu\nu}$ which describes the matter-energy content in the space-time.

The $T_{\mu\nu}$ tensor takes this form:

$$T_{\mu\nu} = (\rho + p)u_{\mu}u_{\nu} + pg_{\mu\nu} \quad (1.2)$$

where ρ and p are, respectively, the energy and the pressure density of the fluid and u_μ is the fluid four-velocity. If the fluid is ideal, $T_{\mu\nu}$ takes a diagonal form with ρ on the time coordinate and p on the space coordinates.

Assuming the Friedmann-Robertson-Walker (FRW) metric ($c = \hbar = 1$)

$$ds^2 = -dt^2 + a^2(t) \left[\frac{dr^2}{1 - kr^2} + r^2(d\theta^2 + \sin^2\theta d\phi^2) \right] \quad (1.3)$$

where $a(t)$ is the scale factor with respect to the cosmic time t ; r , θ and ϕ are the comoving coordinates; the constant k describes the geometry of the space-time ($k = +1, 0, -1$, respectively corresponding to a closed, flat and open Universe); the Einstein's equation split into the two Friedmann equations

$$H^2 \equiv \left(\frac{\dot{a}}{a} \right)^2 = \frac{8\pi G\rho}{3} - \frac{k}{a^2} \quad (1.4)$$

$$\dot{H} = -4\pi G(\rho + p) + \frac{k}{a^2} \quad (1.5)$$

where H is the Hubble parameter depending on time, and ρ and p are the total matter and energy density of all the constituents of the Universe at a given time.

The mass conservation equation is

$$\dot{\rho} + 3H(\rho + p) = 0, \quad (1.6)$$

and combining Eq.s 1.4 and 1.5 we find the equation for the acceleration of the scale-factor

$$\frac{\ddot{a}}{a} = -\frac{4\pi G}{3}(\rho + 3p). \quad (1.7)$$

The evolution of the total energy density of the Universe is governed by

$$d(\rho a^3) = -pd(a^3); \quad (1.8)$$

which is the First Law of Thermodynamics for a particular fluid in the expanding Universe.

If the we consider a fluid with equation of state $p = \gamma\rho$, it follows that $\rho \propto a^{-3(1+\gamma)}$ and $a \propto t^{2/3(1+\gamma)}$.

For $p = \rho/3$, ultra-relativistic matter, $\rho \propto a^{-4}$ and $a \sim t^{1/2}$; for $p = 0$, very nonrelativistic matter, $\rho \propto a^{-3}$ and $a \sim t^{2/3}$; and for $p = -\rho$, vacuum energy, $\rho = \text{const.}$

We can use the Friedmann equation to relate the curvature of the Universe to the energy density and expansion rate:

$$\Omega - 1 = \frac{k}{a^2 H^2}; \quad (1.9)$$

$$\Omega = \frac{\rho}{\rho_{\text{crit}}}; \quad (1.10)$$

where the critical density today $\rho_{\text{crit}} = 3H^2/8\pi G = 1.88h^2 \text{ g cm}^{-3} \simeq 1.05 \times 10^4 \text{ eV cm}^{-3}$. There is a one to one correspondence between Ω and the spatial curvature of the Universe: positively curved, $\Omega_0 > 1$; negatively curved, $\Omega_0 < 1$; and flat ($\Omega_0 = 1$). Model universes with $k \leq 0$ expand forever, while those with $k > 0$ necessarily recollapse. The curvature radius of the Universe is related to the Hubble radius and Ω by

$$R_{\text{curv}} = \frac{H^{-1}}{|\Omega - 1|^{1/2}}. \quad (1.11)$$

Then the curvature radius sets the scale for the size of spatial separations. And in the case of the positively curved model it is just the radius of the 3-sphere.

Today we know this model has many shortcomings, as the *flatness* and the *horizon problems* or the cosmological constant problem (solved by introducing some Dark Energy or Modified Gravity models). However, this standard model provide us a framework within it is possible to study the emergence of structures from the small fluctuations in the density of the early Universe, like the observed galaxies, clusters and the cosmic microwave background.

Over the last decades, observations have significantly increase the idea that: the Universe is spatially flat and accelerating; it passed through an accelerated expansion in the early Universe (inflation epoch); today the energy content consists principally of $\sim 27\%$ of Dark Matter, $\sim 76\%$ of Dark Energy and few % of baryonic matter, whereas the radiation and neutrinos contributions are negligible to the total energy density

$$\Omega_0 = \Omega_{0\text{DM}} + \Omega_{0\text{B}} + \Omega_{0\Lambda} = \Omega_{0\text{M}} + \Omega_{0\Lambda}. \quad (1.12)$$

$\Omega_{0\text{M}}$ is the energy density of the Dark Matter and the baryonic matter together, all considered in their actual value.

If we consider a flat Universe, $\Omega_0 = 1$

$$\Omega_{0\Lambda} = 1 - \Omega_{0\text{M}}. \quad (1.13)$$

The combined data from high redshift supernovae (SN1), large scale structures (LSS) and cosmic microwave background give

$$\Omega_0 = 1.00_{-0.03}^{+0.07}, \text{ trovainumerigiusti}$$

meaning that the present Universe is spatially flat (or at least very close to being flat). Then restricting to $\Omega_0 = 1$, the dark matter density is

$$\Omega_{\text{DM}} h^2 = 0.1334_{-0.0055}^{+0.0056},$$

the baryon density

$$\Omega_B h^2 = 0.02258_{-0.00056}^{+0.00057}.$$

and the substantial dark (unclustered) energy is inferred,

$$\Omega_\Lambda \approx 0.734 \pm 0.029.$$

In the next section we will see how all components contribute to the thermal history of the Universe, considering a Λ -CDM model.

1.2 Thermal history of the Universe

RADIATION ERA.

AFTER PLANCK TIME, $t_P \equiv \sqrt{\hbar G/c^5} \approx 10^{-43}$ s, $T_P \equiv \sqrt{\hbar c^5/Gk^2} \approx 1.42 \times 10^{19}$ GeV.

In this era the energy density of the expanding Universe was dominated by the radiation component and made up of photons, neutrinos and matter (protons, electrons, helium nuclei and non-bayonic dark matter). At high temperatures both the hydrogen and the helium are fully ionised. In this phase the Thomson scattering occurs on a timescale much less than the expansion timescale, resulting in a tight coupling between matter and radiation.

At time $t = 10^{-35}$ s, the GUT (Grand Unification Theory) phase transition occurs, all the three gauges interactions - electromagnetic, weak and strong - become no longer unified. The inflation epoch also occurs in this era, exponentially expanding the Universe from to in the time range of $10^{-34} - 10^{-32}$ s, during which quantum noise was stretched to astrophysical size seeding cosmic structures. At a temperature of $T \approx 1$ MeV the neutrinos decouple from matter and at $T \approx 0.1$ MeV the first light elements form during the primordial nucleosynthesis (or BBN, Big Bang

Nucleosynthesis).

We know the energy densities for radiation and matter evolves according to:

$$\rho_m = \rho_{0m}(1+z)^3 \quad (1.14)$$

$$\rho_r = \rho_{0r}(1+z)^4 \quad (1.15)$$

When those densities are equal the matter-radiation equivalence occurs and the matter domination begins.

MATTER ERA. $t \approx 10^5$ yrs, $T \approx 10^4$ K, $z_{eq1} \approx 3200$.

In the beginning of this era the radiation and matter temperatures are equivalent

$$T_r = T_{0r}(1+z) \quad (1.16)$$

and remain approximately equal until $z \simeq 300$, thanks to the residual ionisation which allows an exchange of energy between matter and radiation via Compton diffusion. After this redshift the thermal interaction between matter and radiation becomes insignificant, so that the matter component cools adiabatically with a law

$$T_m \propto (1+z)^2. \quad (1.17)$$

With the cooling of the temperature, the Universe reach the epoch of recombination corresponding to a temperature of around $T_{rec} \simeq 4000K$, when 50% of the matter is in the form of neutral atoms. Because of the recombination, around $z_{dec} \simeq 1100$, a no-instantaneous process of decoupling occurs and matter and radiation begin to evolve separately.

After decoupling any primordial fluctuations in the matter component that survive the radiation era grow under the influence of Dark Matter gravitational potential wells and eventually give rise to cosmic structures: star, galaxies and clusters of galaxies. The part of the gas that does not end up in such structures may be reheated and partly reionised by star and galaxy formation, during the reionization period at about $z \approx 10.5$.

After $z_{dec} \simeq 1100$ also the radiation begins free to evolve independently, because the optical depth $\tau_{\gamma e}$ of the Universe due to Compton scattering decreases. This quantity describes the attenuation of the photon flux N_γ as it traverses a certain

length. The probability that a given photon scatters with an electron while travelling a distance $c dt$ is given by

$$-\frac{dN_\gamma}{N_\gamma} = -\frac{dI}{I} = \frac{dt}{\tau_{\gamma e}} = n_e \sigma_T c dt = -\frac{x\rho_m}{m_p} \sigma_T c \frac{dt}{dz} dz = -d\tau \quad (1.18)$$

where n_e is the number electron density, σ_T is the Thompson scattering section, ρ_m is the matter density and m_p is the proton mass; so that

$$I(t_0, z) = I(t) \exp\left(-\int_0^z \frac{x\rho_m}{m_p} \sigma_T c \frac{dt}{dz} dz\right) = I(t) \exp[-\tau(z)] \quad (1.19)$$

$I(t_0, z)$ is the intensity of the background radiation reaching the observer at time t_0 with a redshift z ; $\tau(z)$ is the optical depth of such a redshift; the $x(z)$ is the ionisation fraction from the known *Saha equation*. The probability that a photon, which arrives at the observer at the present epoch, suffers its last scattering event between z and $z-dz$ is

$$-\frac{d}{dz}\{1 - \exp[-\tau(z)]\} dz = \exp[-\tau(z)] d\tau = g(z) dz. \quad (1.20)$$

The quantity $g(z)$ is the effective width of the *surface of last scattering (ls)* and is well approximated by a Gaussian with peak at $z_{ls} \simeq 1100$ and width $\Delta z \simeq 400$. So at redshift z_{ls} we also have $\tau(z) \simeq 1$, because the Universe is transparent to photons.

The photons begin to travel from the last scattering surface creating what is the radiation background of the Universe, called now the *Cosmic Microwave Background*.

DARK ENERGY ERA. $z_{eq2} \approx 0.4$.

Very late with respect to the age of the Universe the energy density of the Dark Energy begins to dominate, accelerating the cosmic expansion, until today, $z = 0$; in the meanwhile large scale structures formed from the primordial fluctuations and by interacting with dark matter potential wells. The nature of this dark component is still unknown and many observational probes have been proposed to test its properties and redshift evolution either in the standard Λ -Cold Dark Matter (Λ CDM), modified gravity or quintessence models (next section for details).

1.3 The Dark Energy models

The Dark Energy component does not interact through any of the fundamental forces other than gravity and assuming the Λ -CDM model it causes the accelerated expansion of the universe. From Eq. 1.7 we know the Dark Energy must have a negative pressure in order to accelerate the expansion, i.e.

$$p < -\frac{1}{3}\rho \quad (1.21)$$

If we parametrize the equation of state of a perfect fluid in this way

$$p = w\rho \quad (1.22)$$

the equation-of-state parameter for Dark Energy will be $w < -1/3$. Nevertheless, the perfect fluid model with a constant state parameter does not work, because if we consider the perturbation theory relation $\delta P = c_s^2 \delta \rho$, where c_s is the speed of sound of Dark Energy, $c_s^2 = w$, a negative state parameter implies negative value for c_s^2 . Therefore it is necessary to describe dark energy with different models: as a fluid with non-linear relation between P and ρ which leads to negative w but positive value of c_s^2 , or a scalar field with an auto interaction potential. We can focus on some of these models. Establishing whether the dark energy is constant or evolving is one of the main challenges for modern cosmology. For example the expected EUCLID mission in 2019 will have as main aims measuring the DE equation of state parameters w_0 and w_1 to a precision of 2% and 10%, respectively, using both expansion history and structure growth; measuring the growth factor exponent γ with a precision of 2%, enabling to distinguish General Relativity from the modified gravity theories; testing the CDM paradigm for structure formation, and measure the sum of the neutrino masses to a precision better than 0.04 eV when combined with Planck.

The time dependence of the Dark Energy equation has been constrained by fitting various forms of $w(z)$ to the SNIa data, often in combination with CMB and the LSS measurements.

One of the most popular two-parameter formula is the linear change in the scale factor $a = (1 + z)^{-1}$ given by,

$$w(a) = w_0 + w_1 a(1 - a) \quad (1.23)$$

where w_0 is the value today and w_1 the value at some early time a .

For general $w(a)$, the dynamical expansion of the Universe is specified by the Friedmann equation

$$E(a) = \frac{H^2(a)}{H_0^2} = \Omega_M a^{-3} + \Omega_K a^{-2} + \Omega_{DE} a^{f(a)}, \quad (1.24)$$

where $\Omega_K \equiv (1 - \Omega_m - \Omega_X)$ is the curvature constant, $H(a) \equiv \dot{a}/a$ is the Hubble parameter with present day value H_0 . $f(a)$ is calculated by solving the conservation of energy equation for the Dark Energy $d(\rho_X a^3)/da = -3p_X a^2$ giving $\rho_X \propto a^{f(a)}$, where

$$f(a) = \frac{-3}{\ln a} \int_0^{\ln a} [1 + w(a')] d \ln a'. \quad (1.25)$$

For constant w , $f(a) = -3(1 + w)$.

For the parameterisation $w(a) = w_0 + w_1 a(1 - a)$,

$$f(a) = -3(1 + w_0) + \frac{3w_1}{2 \ln a} (1 - a)^2. \quad (1.26)$$

1.3.1 The cosmological constant

A cosmological constant was originally introduced by Einstein in 1917 in Eq. 1.1, in order to obtain a static solution for a spatially closed universe

$$R_{\mu\nu} - \frac{1}{2} R g_{\mu\nu} + \Lambda g_{\mu\nu} = 8\pi G T_{\mu\nu}, \quad (1.27)$$

after the discovery of the acceleration expansion of the Universe it was regained as possible candidate for the Dark Energy.

The Friedmann eq.s 1.4 and 1.7 becomes:

$$H^2 \equiv \left(\frac{\dot{a}}{a}\right)^2 = \frac{8\pi G \rho}{3} - \frac{k}{a^2} + \frac{\Lambda}{3} \quad (1.28)$$

$$\frac{\ddot{a}}{a} = -\frac{4\pi G}{3}(\rho + 3p) + \frac{\Lambda}{3}. \quad (1.29)$$

It is a time independent and spatially uniform dark component, which may classically be interpreted as a relativistic perfect simple fluid. If we consider the observational evidences of $\ddot{a} > 0$, from Eq. (1.29) we find the cosmological constant contributes negatively to the pressure term and hence exhibits a repulsive effect, as the Dark Energy does. Introducing the modified energy density and pressure

$$\tilde{\rho} = \rho + \frac{\Lambda}{8\pi G}, \quad \tilde{P} = P - \frac{\Lambda}{8\pi G} \quad (1.30)$$

we find that equations 1.28 and 1.29 reduce to equations 1.4 and 1.7, and that the cosmological constant obeys the equation of state $w = -1$.

The cosmological constant Λ is the oldest and simplest candidate from a mathematical viewpoint, but there is a fundamental problem related to such a theoretically favored candidate which is usually called the cosmological constant problem. The present cosmological upper bound ($\Lambda_o/8\pi G \sim 10^{-47} GeV^4$) differs from natural theoretical expectations ($\sim 10^{71} GeV^4$) by more than 100 orders of magnitude.

We can consider now some others candidates appearing in the literature.

1.3.2 Chaplygin-type gas

It is widely known that the main distinction between the pressureless CDM and Dark Energy is that the former agglomerates at small scales whereas the Dark Energy is a smooth component. Such properties seems to be directly linked to the equation of state of both components. It refers to an exotic fluid, the so-called Chaplygin type gas, whose equation of state is

$$p_X = -\frac{A}{\rho_X^\alpha}, \quad (1.31)$$

where A is constant with dimension $[M^{4(1+\alpha)}]$ and α is constant in the range $[0, 1]$. The $\alpha \neq 1$ constitutes a generalization of the original Chaplygin gas equation of state proposed in [Bento et al, 2004] whereas $\alpha = 0$ gives a model which behaves as Λ CDM. The idea of a Unified Dark-Matter-Energy (UDME) scenario inspired by an equation of state like (1.31) comes from the fact that the Chaplygin type gas can naturally interpolate between non-relativistic matter (CDM) and negative-pressure Dark Energy regimes [Bento et al, 2004]. The Jeans instability of Chaplygin perturbations is at first similar to CDM fluctuations (when the Chaplygin gas has a negligible pressure) and then disappears (when the Chaplygin gas behaves as a cosmological constant). Both this late suppression of Chaplygin fluctuations and the appearance of a non-zero Jeans length leave a large integrated Sachs Wolfe (ISW, see Chap. 3) imprint on the CMB anisotropies.

Motivated by these possibilities, there has been growing interest in exploring the theoretical and observational consequences of the Chaplygin gas, not only as a possibility for unification of the dark sector (dark matter/Dark Energy) but also as a

new candidate for Dark Energy only. The imprint of a Chaplygin gas is also present on the matter power spectrum, since Chaplygin gas perturbations affect both CMB anisotropies and structure formation.

1.3.3 Quintessence

The idea of quintessence originates from an attempt to understand the smallness of the “cosmological constant” or Dark Energy in terms of the large age of the universe [Wetterich, 1988]. As a characteristic consequence, the amount of Dark Energy may be of the same order of magnitude as radiation or dark matter during a long period of the cosmological history, including the present epoch. Today, the inhomogeneous energy density in the universe (dark and baryonic matter) is about $\rho_{inhom} \approx (10^{-3}\text{eV})^4$. This number is tiny in units of the natural scale given by the Planck mass $M_p = 1.22 \cdot 10^{19}$ GeV. Nevertheless, it can be understood easily as a direct consequence of the long duration of the cosmological expansion: a dominant radiation or matter energy density decreases $\rho \sim M_p^2 t^{-2}$ and the present age of the universe is huge, $t_0 \approx 1.5 \cdot 10^{10}$ yr. It is a natural idea that the homogeneous part of the energy density in the universe (the Dark Energy) also decays with time and therefore turns out to be small today. A simple realization of this idea, motivated by the anomaly of the dilatation symmetry, considers a scalar field ϕ with an exponential potential [Wetterich, 1988]

$$\mathcal{L} = \sqrt{g} \left\{ \frac{1}{2} \partial^\mu \phi \partial_\mu \phi + V(\phi) \right\} \quad (1.32)$$

where

$$V(\phi) = M^4 \exp(-\alpha\phi/M), \quad (1.33)$$

with $M^2 = M_p^2/16\pi$. In the simplest version ϕ couples only to gravity, not to baryons. Cosmology is then determined by the coupled field equations for gravity and the scalar “cosmon” field in presence of the energy density ρ of radiation or matter. For a homogeneous and flat universe ($n = 4$ for radiation and $n = 3$ for nonrelativistic matter)

$$\begin{aligned} H^2 &= \frac{1}{6M^2} \left(\rho + \frac{1}{2} \dot{\phi}^2 + V \right), \\ \ddot{\phi} + 3H\dot{\phi} + \frac{\partial V}{\partial \phi} &= 0, \\ \dot{\rho} + nH\rho &= 0. \end{aligned} \quad (1.34)$$

This model predicts a fraction of Dark Energy or homogenous quintessence (as compared to the critical energy density $\rho_c = 6M^2H^2$) which is constant in time

$$\Omega_h = \left(V + \frac{1}{2}\dot{\phi}^2 \right) / \rho_c = \rho_\phi / \rho_c \quad (1.35)$$

both for the radiation-dominated ($n = 4$) and matter-dominated ($n = 3$) universe ($(\Omega_h + \rho/\rho_c) = 1$). This would lead to a natural explanation why today's Dark Energy is of the same order of magnitude as dark matter. For a large value of $V(\phi)$ the force term in Eq.1.34 is large and the Dark Energy decreases faster than matter or radiation. In the opposite, when the matter or radiation energy density is much larger than $V(\phi)$, the force is small as compared to the damping term $3H\dot{\phi}$ and the scalar waits until the radiation or matter density is small enough such that the over-damped regime ends. Stability between the two extreme situations is reached for $V \sim \rho$. For this model, the equation of state parameter w is given by

$$w_Q = \frac{\frac{\dot{\phi}^2}{2} - V(\phi)}{\frac{\dot{\phi}^2}{2} + V(\phi)} \quad (1.36)$$

and can be varied in the range $-1 < w_Q < 1$.

1.3.4 Modified Gravity

In the simplest alternatives to Dark Energy, the present cosmic acceleration is caused by a modification to general relativity, the so called *Modified Gravity*. The General theory of relativity founded by Einstein at the end of 1915 has been successfully verified as modern theory of gravity for the Solar System.

Attempts to modify general relativity started already at its early times and it was mainly motivated by research of possible mathematical generalizations. Recently there has been an intensive activity in gravity modification, motivated by discovery of accelerating expansion of the Universe, which has not yet generally accepted theoretical explanation. The general relativity has not been verified at the cosmic scale (low curvature regime) and Dark Energy has not been directly detected. This situation has motivated a new interest in modification of general relativity, which should be some kind of its generalization. There is not a unique way how to modify general relativity. Among many approaches there are two of them, which have been much investigated: 1) $f(R)$ theories of gravity and 2) nonlocal gravities.

In the case of $f(R)$ gravity, the Ricci scalar R in the action is replaced by a function

$f(R)$. This is extensively investigated for the various forms of function $f(R)$. We have had some investigation when $f(R) = R \cosh \frac{\alpha R + \beta}{\gamma R + \delta}$ and, after completion of research, the results will be presented elsewhere.

1.4 Observational evidences for Dark Energy

There are many observational evidences of the Dark Energy effect. Historically, the acceleration expansion was revealed for the first time by Ia supernovæ observations. In 1998 two groups of astronomers [Perlmutter et al., 1999] estimated the distance-redshift relation using Type Ia supernovæ (SNe), a class of exploding stars whose distance can be measured with $\sim 15\%$ accuracy, much better than for other distant sources. They found the $\dot{a}(t)$ is increasing, i.e. the universe is not merely expanding, the expansion is accelerating.

Many other indirect supporting evidences come from different measurements. Now galaxy clustering, weak lensing, baryonic acoustic oscillation (BAO) on the CMB anisotropies, ages of the oldest stars are generally considered the most powerful observational probes of Dark Energy.

Another method also provides additional cross-checks on Dark Energy constraints, the late time anisotropy in the CMB, the Integrated Sachs-Wolfe effect (ISW), can be detected and used to constrain cosmology.

It is important to take into account the results from all different observations, because individually they do not allow to determine matter and Dark Energy density, since they always involve a combination of these two parameters (“Cosmic Degeneracy”).

The data from all these observations are not accurate enough to distinguish between the cosmological constant and many forms of dynamical Dark Energy. Moreover degeneracies between Dark Energy parameters strongly limit the possibility to test whether w is constant or not.

1.4.1 Type Ia Supernovæ

Type Ia Supernovæ are generally believed to have homogeneous intrinsic luminosity of peak magnitude. So SNe Ia are usually known as standard candles which could be used to measure the expansion history of the Universe. The analysis of their

distance modulus versus redshift could provide direct evidence for the acceleration of the Universe and the analysis also put a constraint on dark energy models. The luminosity distance d_L of SNe Ia is defined by

$$d_L(z) = \frac{c(1+z)}{H_0} F(z) \approx \frac{c}{H_0} \left[z + \frac{1}{2}(1-q_0)z^2 + \dots \right]. \quad (1.37)$$

The function $F(z)$ is

$$F(z) = \int_0^z \frac{1}{E(z')} dz'. \quad (1.38)$$

where, if we consider a flat Universe with constant w , $E(z)$ is given by the Friedmann equation written as Eq.1.24.

q_0 is the deceleration parameter, given by

$$q_0 \equiv -\frac{\ddot{a}a}{\dot{a}^2} = \left[-\frac{\dot{H} + H^2}{H^2} \right]_0 \simeq \frac{\Omega_{0M}}{2} + \Omega_{0DE} \quad (1.39)$$

if $q_0 < 0$ the Universe is accelerating. The distance modulus is defined by

$$\mu \equiv m - M = 5 \log \frac{d_L}{\text{Mpc}} + 25, \quad (1.40)$$

where m and M are the apparent and absolute magnitudes, respectively; from the first observations the Universe seems to accelerate because $q_0 > 0$, then we can constrain the combination between the two cosmological parameters Ω_{DE} and Ω_M

$$2\Omega_{DE} > \Omega_M \quad (1.41)$$

1.4.2 Baryonic acoustic oscillations (BAO)

The Baryonic Acoustic Oscillations signatures in the large-scale clustering of galaxies could act as additional tests for constraining Dark Energy cosmology, because the acoustic oscillations in the relativistic plasma of the early Universe could be imprinted onto the late-time power spectrum of the non-relativistic matter, as galaxy clusters. The BAO relevant distance measure is modelled by volume distance, which is defined as

$$D_V(z) = \left[\frac{d_A^2(z)z}{H(z)} \right]^{1/3}, \quad (1.42)$$

where $H(z)$ is the Hubble parameter and $d_A(z) = \int_0^z \frac{1}{H(z')} dz'$ is the comoving angular diameter distance. BAO measurements provide both $d_A(z)$ and $H(z)$ using almost completely linear physics, i.e. measuring the sound horizon today from clustering

galaxies. Then $D_V(z)$ can be computed essentially from the growth factor (1.65) of perturbation theory which contains the cosmological parameters. Combining the information from BAO and from the first peak position of the CMB power spectrum which sets the Universe to be flat

$$\ell_{fp} \simeq 220\Omega_0^{-1/2}, \quad (1.43)$$

$$\Omega_0 = \Omega_M + \Omega_{DE} \simeq 1. \quad (1.44)$$

it is possible to constrain separately values of Ω_{DE} and Ω_M .

1.4.3 Gravitational lensing

The gravitational lensing is regarded as an independent tool that complements SNe Ia as a probe on Dark Energy. The statistics of gravitational lensing of quasars (QSOs) by intervening galaxies can constrain on the cosmological constant. Lensed images of distant galaxies in cluster, arcs or rings, may provide a bound on the equation of state parameter of Dark Energy. The gravitational lensing system can be used measure the ratio of angular diameter distances. However, the lensing observations primarily depend on the parameters of lens models with minor dependence on cosmological parameters. There is the lens model degeneracy in both the projected mass density profile and the circular velocity profile. It is shown that we need to measure the Einstein radius and the velocity dispersion within $\mathcal{O}(1)\%$ accuracy in order to put a constraint on ω_{DE} .

In the gravitational lensing, one of the observable quantities without having any model dependence is the Einstein radius (θ_E), which is proportional to the velocity dispersion squared (σ_v^2) and the ratio of the angular distances D_{ds}/D_s , where D_{ds} is the distance from the lens to the source and D_s is that from the source to the observer. With different values of cosmological parameters, we can have different values of D_{ds}/D_s , *i.e.* different values of θ_E . Thus, it might be used for probing the property of Dark Energy, ω_{DE} . However, there is an ambiguity in measuring σ_v . If the error of σ_v measurement is not within the differences of D_{ds}/D_s between different cosmological models, then we cannot distinguish the differences between models by measuring θ_E .

1.5 Inflation

In 1980 Guth and Starobinsky developed the theory of inflation in order to solve the shortcomings of the Big Bang theory, as the horizon, flatness and magnetic monopole problems. We forementioned that an exponential accelerating expansion occurs during the primordial phases of the evolution of the Universe, with the scale factor evolves as

$$a = a_i e^{H_I(t-t_i)}, \quad (1.45)$$

where t_i denotes the time at which inflation starts and H_I the value of the Hubble rate which remains constant during a inflationary (de Sitter) epoch. During inflation, the horizon

$$r_H(t) = a(t) \int_0^t \frac{dt}{a(t)} \quad (1.46)$$

grows more slowly than the scale factor, therefore, regions that were in causal connection before this period are pushed outside the Hubble radius

$$r_{Hubble} = \frac{1}{H} \quad (1.47)$$

An accelerating period is obtainable only if the overall pressure p of the universe is negative: $p < -\rho/3$. Neither a radiation-dominated phase nor a matter-dominated phase (for which $p = \rho/3$ and $p = 0$, respectively) satisfy such a condition. From theory we know the inflation is driven by the vacuum energy of the inflaton field.

This period of exponential expansion solved some of the shortcomings of the standard Big Bang Theory.

1.5.1 Horizon Problem

The horizon problem is related to the fact that every Big Bang model have a cosmological horizon which delimits regions in causal connection one with the others. In the Big Bang theory the horizon is too small to explain the high isotropy observed in the CMB where very far emission regions seem to be in causal connection and inside the cosmological horizon. If inflation lasts long enough, all the physical scales that have left the horizon during the radiation-dominated or matter-dominated phase can re-enter the horizon in the past: this is because such scales are exponentially reduced. This explains the problem of the homogeneity of CMB and the initial condition problem of small cosmological perturbations. Once

the physical length is within the horizon, microphysics can act, the universe can be made approximately homogeneous and the primaeval inhomogeneities can be created.

If t_i and t_f are, respectively, the time of beginning and end of inflation, we can define the corresponding number of e-foldings N as

$$N = \ln [H_I(t_e - t_i)]. \quad (1.48)$$

A necessary condition to solve the horizon problem is that the largest scale we observe today, the present horizon H_0^{-1} , was reduced during inflation to a value $\lambda_{H_0}(t_i)$ smaller than the value of horizon length H_I^{-1} during inflation. This gives

$$\lambda_{H_0}(t_i) = H_0^{-1} \left(\frac{a_{t_f}}{a_{t_0}} \right) \left(\frac{a_{t_i}}{a_{t_f}} \right) = H_0^{-1} \left(\frac{T_0}{T_f} \right) e^{-N} \lesssim H_I^{-1},$$

where for simplicity the short period of matter-domination is neglected and we have called T_f the temperature at the end of inflation. We get

$$N \gtrsim \ln \left(\frac{T_0}{H_0} \right) - \ln \left(\frac{T_f}{H_I} \right) \approx 67 + \ln \left(\frac{T_f}{H_I} \right).$$

Apart from the logarithmic dependence, we obtain $N \gtrsim 70$.

1.5.2 Flatness problem

The flatness problem is related to the fact that although cosmological data are in agreement with a flat Universe, the Big Bang model requires a fine tuning on the density parameter that has to be

$$\Omega^{-1} - 1 \simeq 10^{-60} \quad (1.49)$$

not only at present time but at all times. Inflation also solves elegantly the flatness problem. Since during inflation the Hubble rate is constant

$$\Omega - 1 = \frac{k}{a^2 H^2} \propto \frac{1}{a^2}.$$

On the other end reproduce a value of $(\Omega_0 - 1)$ of order of unity today the initial value of $(\Omega - 1)$ at the beginning of the radiation-dominated phase must be $|\Omega - 1| \sim 10^{-60}$. Since we identify the beginning of the radiation-dominated phase with the beginning of inflation, we require

$$|\Omega - 1|_{t=t_f} \sim 10^{-60}.$$

During inflation

$$\frac{|\Omega - 1|_{t=t_f}}{|\Omega - 1|_{t=t_i}} = \left(\frac{a_i}{a_f}\right)^2 = e^{-2N}. \quad (1.50)$$

Taking $|\Omega - 1|_{t=t_i}$ of order unity, it is enough to require that $N \approx 70$ to solve the flatness problem. Inflation does not change the global geometric properties of the spacetime. If the universe is open or closed, it will always remain flat or closed, independently from inflation. What inflation does is to magnify the radius of curvature R_{curv} defined in Eq. (1.11) so that locally the universe is flat with a great precision.

1.5.3 Monopole problem

The magnetic monopole problem is related with the GUT [Buras et al., 1978], the Big Bang theory predicts the creation of a number n_m of magnetic monopoles during the GUT phase transition

$$n_m > 10^{-10} n_\gamma \quad (1.51)$$

where n_γ is the number density of photon at that time. None of the processes in the Universe history can destroy monopoles, then today they should be $n_{m0} > 10^{-10} n_\gamma \simeq n_{b0}$. These monopoles are very massive particles ($m_m \simeq 10^{16}$ GeV) and according to their predicted abundance they should be the dominant component of the cosmological fluid

$$\Omega_m = \frac{\rho_{m0}}{\rho_{c0}} = \frac{m_m n_{m0}}{\rho_{c0}}, \quad (1.52)$$

$$\Omega_m > 10^{16} \Omega_b \quad (1.53)$$

The measured total density Ω_0 and the lack of positive magnetic monopole detections deny all the previous assumptions. Considering the inflation epoch, we find the magnetic monopoles are created before inflation and therefore their density is diluted by the exponential expansion up to a point where their contribution to the cosmological fluid is irrelevant and it is extremely improbable to observe them.

1.6 Cosmological perturbation theory

The theory of structure formation studies how the primordial fluctuations in matter and radiation grow into galaxies and clusters of galaxies due to self gravity. Structures were generated by the gravitational instability mechanism from tiny

perturbations present at very early times and produced from quantum fluctuations during the inflation period. CMB observations indicate that the anisotropies at the epoch of decoupling were rather small (one part in 10^5), implying that their amplitudes were even smaller at earlier epochs. Then the generation and the evolution of the perturbations can be studied using linear perturbation theory.

1.6.1 Metric perturbations

In a Friedmann background, the metric perturbations can be decomposed according to their behavior under local rotation of the spatial coordinates on hyper-surfaces of constant time. Therefore, the perturbations are classified into scalars, vectors and tensors. Scalar perturbations are invariant under rotations and are the main responsible for the anisotropies and the inhomogeneities in the Universe.

In the following we use only scalar perturbations in order to obtain, in the linear regime, the evolution equations of the matter fluctuations created in the inflation period.

We start deriving the perturbed continuity, Euler and Poisson equations in the matter domain, inserting a generic small perturbation on the homogeneous density ρ_b , velocity v_b , pressure p_b and the gravitational potential Φ_b values

$$\rho = \rho_b + \rho_i, \quad v = v_b + v_i, \quad p = p_b + p_i, \quad \Phi = \Phi_b + \Phi_i \quad (1.54)$$

in the continuity and Euler equations

$$\frac{\partial \rho}{\partial t} + \nabla(\rho v) = 0 \quad (1.55a)$$

$$\frac{\partial v}{\partial t} + (v \nabla)v = -\frac{\nabla p}{\rho} - \nabla \Phi \quad (1.55b)$$

$$\nabla^2 \Phi = 4\pi G \rho \quad (1.55c)$$

We have to take into account also the equation of state, $c_s^2 = \partial p / \partial \rho$. Then the perturbed equations are

$$\frac{\partial \rho_i}{\partial t} + \rho_b \nabla(\rho v_i) + \rho_i \nabla v_b = 0 \quad (1.56a)$$

$$\frac{\partial v_i}{\partial t} + (v_i \nabla)v_b = -\frac{\nabla p_i}{\rho_b} - \nabla \Phi_i \quad (1.56b)$$

$$\nabla^2 \Phi_i = 4\pi G \rho_{i..} \quad (1.56c)$$

We introduce the density contrast $\delta = (\rho - \rho_b)/\rho_b$ and change in comoving coordinates

$$\nabla_r = \frac{\nabla_x}{a}, \quad \dot{r} = \dot{a}x + a\dot{x}, \quad (1.57)$$

where the first term in \dot{r} is the expansion velocity $v_b = \dot{a}x$ and the second one is the peculiar velocity of the perturbation $v_i = a\dot{x}$; we define $u = \dot{x}$ as the comoving velocity of the perturbation. Therefore, the continuity equation becomes

$$\dot{\delta} = -\nabla_x u, \quad (1.58)$$

and the Euler

$$\ddot{\delta} + 2\frac{\dot{a}}{a}\dot{\delta} = \frac{\nabla_x^2 p_i}{\rho_b a^2} + \frac{\nabla_x^2 \Phi_i}{a^2}. \quad (1.59)$$

Finally, by using the equation of state and Eq. (1.56c), assuming a typical Fourier transformation given by

$$f(\mathbf{k}, t) = \frac{1}{(2\pi)^{3/2}} \int d^3k e^{i\mathbf{k}\cdot\mathbf{x}} f(\mathbf{x}, t), \quad (1.60)$$

we obtained the perturbation equation

$$\ddot{\delta} + 2\frac{\dot{a}}{a}\dot{\delta} = \frac{c_s^2}{a^2} \nabla_x^2 \delta + 4\pi G \rho_b \delta. \quad (1.61)$$

This equation has the typical harmonic oscillator form, the second term in the left side is the damping term containing the expansion rate of the Universe in opposition to the gravitational collapsing. From this equation, it is possible to write the evolution equation for all kinds of fluid and Ω .

1.6.2 Structure formation

Now we know where the primordial fluctuations come from, we can study how these perturbations become structures under the influence of the gravity only. Then we can assume the matter pressure term is negligible with respect to the gravitational potential one

$$k^2 c_s^2 \ll 4\pi G \rho_b. \quad (1.62)$$

In the following analysis we consider a Universe with $\Omega_{0\text{DE}} \neq 0$ and $w = -1$.

From Eq. (1.14) and Eq. (1.10) we find

$$4\pi G \rho_b = \Omega_0 \frac{3H_0^2}{2a^3}, \quad (1.63)$$

therefore, the Eq. (1.64) becomes

$$\ddot{\delta} + 2\frac{\dot{a}}{a}\dot{\delta} = \Omega_{0M}\frac{3H_0^2}{2a^3}\delta. \quad (1.64)$$

One of the two solutions is

$$\delta(a) = \frac{5\Omega_M}{2}E(a) \int_0^a \frac{da'}{[a'E(a')]^3} \equiv D(a), \quad (1.65)$$

where $E(a)$ is given by Eq. 1.24. It defines the growth factor $D(a)$ of the matter perturbations, a function of the natural logarithm of the scale factor. The linear growth factor is strongly dependent on w , with $w > -1$ models behaving more like open Universes than $w < -1$ models as the effect of the Dark Energy diminishes.

Although this integral can be easily solved numerically, it is common to use the approximation of [Carroll et al., 1992]

$$D(a) \simeq \frac{5\Omega_M(a)a}{2} \left[\Omega_M(a)^{4/7} - \Omega_\Lambda(a) + \left(1 + \frac{\Omega_M(a)}{2}\right) \left(1 + \frac{\Omega_\Lambda(a)}{70}\right) \right]^{-1}. \quad (1.66)$$

1.6.3 Non-linear perturbations

Now we deal with the non-linear perturbations in order to find the power spectrum which also characterizes the CMB anisotropies.

We can start considering a volume V_u in which there is significant structure due to the perturbations and also denote by $\langle\rho\rangle$ the mean density in the volume, by $\rho(\mathbf{x})$ the density at a point specified by the position vector \mathbf{x} with respect to some arbitrary origin. We define the fluctuation $\delta(\mathbf{x}) = [\rho(\mathbf{x}) - \langle\rho\rangle]/\langle\rho\rangle$. As usual is more expressible as a Fourier series:

$$\delta(\mathbf{x}) = \sum_{\mathbf{k}} \delta_{\mathbf{k}} \exp(i \mathbf{k} \cdot \mathbf{x}) = \sum_{\mathbf{k}} \delta_{\mathbf{k}}^* \exp(i \mathbf{k} \cdot \mathbf{x}). \quad (1.67)$$

The Fourier coefficients $\delta_{\mathbf{k}}$ are complex quantities given by

$$\delta_{\mathbf{k}} = \frac{1}{V_u} \int_{V_u} \delta(\mathbf{x}) \exp(i \mathbf{k} \cdot \mathbf{x}) d\mathbf{x}. \quad (1.68)$$

Now we can imagine a large number N of such volumes, i.e. a large number of ‘realisations’ of the Universe, one will find that $\delta_{\mathbf{k}}$ varies from one to the other in both amplitude and phase. If the phases are random, the density field has Gaussian

statistics: so the mean value of perturbation is identically zero by definition, its mean square value, i.e. its variance σ^2 , is not but

$$\sigma^2 \equiv \langle \delta^2 \rangle = \sum_{\mathbf{k}} \langle |\delta_{\mathbf{k}}|^2 \rangle = \frac{1}{V_u} \sum_{\mathbf{k}} \delta_{\mathbf{k}}^2. \quad (1.69)$$

If we now take the $V_u \rightarrow \infty$ and assume that density field is statistically homogeneous and isotropic, so that there is no dependence on the direction of \mathbf{k} but only on $k = |\mathbf{k}|$, we find

$$\sigma^2 = \frac{1}{V_u} \sum_{\mathbf{k}} \delta_{\mathbf{k}}^2 \rightarrow \frac{1}{2\pi^2} \int_0^{+\infty} P_{\Phi}(k) k^2 dk, \quad (1.70)$$

where, for simplicity, $\delta_{\mathbf{k}}^2 = P_{\Phi}(k)$. The quantity $P_{\Phi}(k)$ is called the power spectral density function of the field Φ , or *power spectrum*, and σ^2 tells us about the amplitude of perturbations.

The perturbation power spectrum $P_{\Phi}(k)$, at least within a certain interval in k , is given by the following power law

$$P_{\Phi}(k) = Ak^n, \quad (1.71)$$

the exponent n is usually called the spectral index.

The equation 1.70 can also be written in the form

$$\sigma^2 = \frac{1}{2\pi^2} \int_0^{\infty} P_{\Phi}(k) k^2 dk = \int_{-\infty}^{\infty} \Delta(k) d \ln k \quad (1.72)$$

where the dimensionless quantity

$$\Delta(k) = \frac{1}{2\pi^2} P_{\Phi}(k) k^3. \quad (1.73)$$

It is more convenient to construct a statistical description of the fluctuation field as a function of some scale R . In this way it is possible to define a mass variance inside a spherical volume V of radius R with mass M

$$\sigma_M^2 = \frac{\langle \delta M^2 \rangle^2}{\langle M \rangle} \quad (1.74)$$

Using the usual Fourier decomposition as before we find

$$\sigma^2 = \frac{1}{V_u} \sum_{\mathbf{k}} \delta_{\mathbf{k}}^2 W^2(k R); \quad (1.75)$$

the function $W(k R)$ is called the *window function*. We shall use this expression when we define the cross-correlation power spectra for the ISW effect (Chapter 3).

Chapter 2

Cosmological Microwave Background

The cosmic microwave background was first predicted by Alpher and Herman [Alpher & Herman, 1998] in 1948 as a thermal relic isotropic radiation with an estimated mean temperature of 5 K. The first detection of the microwave background comes in 1965 by Penzias and Wilson [Penzias & Wilson, 1965], for which they later won the Nobel Prize, who observed an excess of 3.5K in their antenna temperature noise on the $\lambda = 7.35\text{cm}$. From that discovery the field of cosmic microwave background (CMB) anisotropies has advanced over the years, especially thanks to the instruments like COBE (the NASA satellite COsmic Background Explorer, launched in 1989) and WMAP (the NASA satellite Wilkinson Microwave Anisotropy Probe, 2001-2012 activity). Their observations have turned some of initial speculations about the Universe into the current cosmological model: namely, that the Universe is spatially flat, consists mainly of dark matter and dark energy, with the small amount of ordinary matter necessary to explain the light element abundances products of nucleosynthesis, and large scale structures formed through gravitational instability from primordial perturbations which might be explained as originated by quantum mechanical fluctuations during inflation. COBE confirmed the cosmological origin predictions of the CMB, measuring an almost perfect blackbody spectrum peaked at 2.725 ± 0.002 K and a temperature anisotropies of the order of $\Delta T/T \sim 10^{-5}$ at the angular scale of 7 degrees. From these observations we learn that the CMB is remarkably uniform except for the dipole induced by the motion of the Solar Sistem [Smoot et al, 1977]. This is in contrast to the matter in the Universe, organized in very non-linear structures like galaxies and clusters. The smooth photon distribution observed in CMB with respect to the clumpy matter distribution is due to the radiation pressure. Matter inhomogeneities grow due to

gravitational instability, but pressure prevents the same process from occurring in the photons. Thus, even though both inhomogeneities in the matter in the Universe and anisotropies in the CMB apparently originated from the same source, these appear very different today.

Since the photon distribution is very uniform, perturbations are small, and linear response theory applies. This is perhaps the most important fact about CMB anisotropies. If the sources of the anisotropies are also linear fluctuations, anisotropy formation falls in the domain of linear perturbation theory (/ref.capitolo primo). There are then essentially no phenomenological parameters that need to be introduced to account for non-linearities or gas dynamics or any other of a host of astrophysical processes that typically afflict cosmological observations.

CMB anisotropies in the working cosmological model fall almost entirely under linear perturbation theory. The most important observables of the CMB are the power spectra of temperature and polarization maps. Theory predicts, and now observations confirm, that the temperature power spectrum has a series of prominent peaks and troughs. In 2.1.1, we discuss the origin of these acoustic peaks and their cosmological uses.

2.1 Primordial anisotropies

In order to study the CMB we consider its intensity as a function of frequency and direction on the sky $\hat{n}(\theta, \phi)$. Since the CMB spectrum is an extremely good blackbody [Fixen & Mather, 2002], generally the observable T is described in terms of a temperature fluctuation

$$\frac{\Delta T}{T}(\theta, \phi) = \frac{T(\theta, \phi) - T_0}{T_0}. \quad (2.1)$$

By using the spherical harmonics expansion

$$\frac{\Delta T}{T}(\theta, \phi) = \sum_{\ell} \sum_m a_{\ell m} Y_{\ell m}(\theta, \phi), \quad (2.2)$$

if these fluctuations are Gaussian, then the multipole moments of the temperature field

$$a_{\ell m} = \int d\hat{n} Y_{\ell m}^*(\hat{n}) \frac{\Delta T}{T}(\hat{n}) \quad (2.3)$$

are fully characterized by their power spectrum

$$\langle a_{\ell m}^* a_{\ell' m'} \rangle = \delta_{\ell\ell'} \delta_{mm'} C_{\ell}, \quad (2.4)$$

whose values as a function of the multipoles ℓ are independent in a given realization. For this reason predictions and analyses are typically performed in harmonic space.

Since the angular wavelength $\theta \simeq 2\pi/\ell$, large multipole moments corresponds to small angular scales. Likewise, since in this limit the variance of the field is $\int d^2\ell C_\ell/(2\pi)^2$, the power spectrum is usually displayed as

$$\Delta_T^2 \equiv \frac{\ell(\ell+1)}{2\pi} C_\ell T^2. \quad (2.5)$$

Whereas COBE first detected anisotropy on the largest scales, observations in the last decade have pushed the frontier to smaller and smaller scales. The WMAP satellite, launched in June 2001, went out to $\ell \sim 1000$, while the ESA satellite, Planck, launched in 2009, went a factor of two higher.

The power spectra (mettere plot pogosian per cosmic variance) exhibit large uncertainty at low multipoles. The reason is that the predicted power spectrum is the average power in the multipole moment ℓ an observer would see in an ensemble of universes. However a real observer is limited to one Universe and one sky with its one set of $a_{\ell m}$'s, $2\ell+1$ numbers for each ℓ . This is particularly problematic for the monopole and dipole ($\ell = 0, 1$). If the monopole were larger in our vicinity than its average value, we would have no way of knowing it. Likewise for the dipole, we have very little hope of distinguishing a cosmological dipole from our own peculiar motion with respect to the CMB rest frame.

In this way low ℓ 's are dominated by ‘‘cosmic variance’’ because there are only $2\ell+1$ m -samples of the power in each multipole moment

$$\Delta C_\ell = \sqrt{\frac{2}{2\ell+1}} C_\ell. \quad (2.6)$$

By averaging over ℓ in bands of $\Delta\ell \approx \ell$, the precision in the power spectrum determination scales as ℓ^{-1} , i.e. $\sim 1\%$ at $\ell = 100$ and $\sim 0.1\%$ at $\ell = 1000$.

Of course, any source of noise, instrumental or astrophysical, increases the errors. If the noise is also Gaussian and has a known power spectrum, one simply replaces the power spectrum on the right hand side of Eq. (2.6) with the sum of the signal and noise power spectra [Knox, 1995]. Because astrophysical foregrounds are typically non-Gaussian it is usually also necessary to remove heavily contaminated regions, e.g. the galaxy. If the fraction of sky covered is f_{sky} , then the errors increase by a factor of $f_{\text{sky}}^{-1/2}$ and the resulting variance is usually called ‘‘sample variance’’. Taking

into account these caveats, the Eq.(2.6) becomes the Knox equation [Knox, 1995]

$$\Delta C_\ell = \sqrt{\frac{2}{f_{sky}(2\ell + 1)}} \left(1 + \frac{A_{pix}\sigma_{pix}^2}{C_\ell e^{-\ell^2 FWHM/\sqrt{8\log 2}}} \right) C_\ell. \quad (2.7)$$

where A_{pix}, σ_{pix} are the area of the pixel and the sensitivity per pixel and $FWHM$ is the full width half maximum.

2.1.1 Acoustic peaks

As we have seen in Chap. 1, when the temperature of the Universe was at $T_{rec} \sim 4000\text{K}$ and a redshift $z_{rec} \approx 1100$, electrons and protons combined to form neutral hydrogen, in the recombination time. Before this epoch, free electrons acted as glue between the photons and the baryons through Thomson and Coulomb scattering, so the cosmological plasma was a tightly coupled *photon-baryon fluid* [Peebles & Yu, 1970]. At $\ell > 100$ the CMB power spectrum can be explained almost completely by analyzing the behavior of this pre-recombination fluid.

We can start from the general evolution equation, Eq.(1.64), for perfect photon fluid, neglecting for the first approximation the dynamical effects of gravity and the baryons. Since perturbations are very small, we assume a linear approximation for the evolution equations and different Fourier modes evolving independently.

$$\ddot{\delta} = \frac{c_s^2}{a^2} \nabla_x^2 \delta \quad (2.8)$$

The photon pressure is $p_\gamma = \rho_\gamma/3$, the temperature density $\rho_\gamma \propto T^4$ and the density contrast is given by $4\delta_T = \rho_\gamma/\bar{\rho} - 1$.

where $c_s \equiv \sqrt{\dot{p}/\dot{\rho}} = 1/\sqrt{3}$ is the sound speed in the (dynamically baryon-free) fluid. We find the pressure gradients act as a restoring force to any initial perturbation in the system which thereafter oscillate at the speed of sound. Physically these temperature oscillations represent the heating and cooling of a fluid that is compressed and rarefied by a standing sound or acoustic wave. This behavior continues until recombination. Assuming negligible initial velocity perturbations, we have a temperature distribution at recombination of

$$\delta(\eta_{rec}) = \delta(0) \cos(k s_{rec}), \quad (2.9)$$

where $s = \int c_s d\eta \approx \eta/\sqrt{3}$ is the distance sound can travel by η (called sound horizon).

In the limit of scales large compared to the sound horizon $ks_{rec} \ll 1$, the perturbation is frozen into its initial conditions, so the large-scale anisotropies measured mainly by satellites directly measure the initial conditions. On small scales, the amplitude of the Fourier modes will exhibit temporal oscillations. Modes that are caught at maxima *or* minima of their oscillation at recombination correspond to peaks in the power, i.e. the variance of $\delta(k, \eta_{rec})$. Because sound takes half as long to travel half as far, modes corresponding to peaks follow a harmonic relationship $k_n = n\pi/s_{rec}$, where n is an integer. A spatial inhomogeneity in the CMB temperature of wavelength λ appears as an angular anisotropy of scale $\theta \approx \lambda/d$ where $d(z)$ is the comoving angular diameter distance from the observer to redshift z .

In a spatially curved universe, the angular diameter distance no longer equals the coordinate distance, making the peak locations sensitive to the spatial curvature of the Universe [Doroshkevich et al, 1978, Kamionkowski et al, 1994].

At present, observations of the location of the first peak of the CMB anisotropies strongly point to a flat universe, in combination with other cosmological constraints.

The inflationary paradigm postulates that an early phase of near exponential expansion of the Universe was driven by a form of energy with negative pressure. In most models, this energy is usually provided by the potential energy of a scalar field. The inflationary era brings the observable universe to a nearly smooth and spatially flat state. Nonetheless, quantum fluctuations in the scalar field are unavoidable and also carried to large physical scales by the expansion. Because an exponential expansion is self-similar in time, the fluctuations are scale-invariant, i.e. in each logarithmic interval in scale the contribution to the variance of the fluctuations is equal. Since the scalar field carries the energy density of the Universe during inflation, its fluctuations induce variations in the spatial curvature [Guth & Pi, 1985, Hawking, 1982].

In order to understand the formation of CMB primordial anisotropies, we have to relate the inflationary prediction of nearly scale-invariant curvature fluctuations to the initial temperature fluctuations. General relativity says the Newtonian potential is also a time-time fluctuation in the metric and it corresponds to a temporal shift of $\delta t/t = \Psi$. The CMB temperature varies as the inverse of the scale factor, which in turn depends on time as $a \propto t^{2/[3(1+p/\rho)]}$. Therefore, the fractional change in the

CMB temperature

$$\frac{\Delta T}{T} = -\frac{\delta a}{a} = -\frac{2}{3} \left(1 + \frac{p}{\rho}\right)^{-1} \frac{\delta t}{t}. \quad (2.10)$$

Thus, a temporal shift produces a temperature perturbation of $-\Psi/2$ in the radiation dominated era (when $p_\gamma = \rho_\gamma/3$) and $-2\Psi/3$ in the matter dominated epoch ($p = 0$) ([Peacock, 1991]; [White & Hu, 1997]).

Also, for a fluctuation Φ in the gravitational potential, the effect of a gravitational redshift is to cause a fractional variation of the temperature $\Delta T/T = \Phi$. In the simplest case of a flat universe described by a matter-dominated Friedmann model, the net effect is therefore given by $\Delta T/T = \Phi/3$. The initial temperature perturbation is therefore linked with the initial gravitational potential perturbation.

The primordial density fluctuations have left their imprint on the cosmic microwave background radiation in the form of small variations in the temperature in different directions on the sky. After recombination between electron and photons, when the decoupling photons-baryons occurred, photons begin to travel in the *last scattering surface* (hereafter *lss*) of thickness Δz and encounter variations in the metric which correspond to variations in the gravitational potential in Newtonian gravity. This process during the *lss* is called Sachs-Wolfe effect ([Sachs & Wolfe, 1967]). The effect is essentially gravitational in origin. According to general relativity, photons climbing out of a potential well will suffer a gravitational redshift which tends to make the region from which they come appear colder.

The ripples seen by the COBE satellite were caused by the Sachs-Wolfe effect and it fixes the amplitude of the initial power spectrum ($P(k)$) of the primordial density fluctuations that are needed to start off the gravitational Jeans instability on which these theories are based.

Now it is necessary to take into account the gravitational influence because the Newtonian potential and the spatial curvature alter the acoustic oscillations by providing a gravitational force on the oscillator. The simplified Euler equation (2.8) gains a term on the right hand side due to the gradient of the potential $k\Psi$. The main effect of gravity then is to make the oscillations a competition between pressure gradients $k\delta$ and potential gradients $k\Psi$ with an equilibrium when $\delta + \Psi = 0$.

The oscillator equation (2.8) becomes

$$\ddot{\delta} + c_s^2 k^2 \delta = -\frac{k^2}{3} \Psi. \quad (2.11)$$

In a flat universe and in the absence of pressure, Ψ is constant. Also, in the absence of baryons, $c_s^2 = 1/3$ so the new oscillator equation is identical to Eq. (2.8) with δ replaced by $\delta + \Psi$. The solution in the matter dominated epoch is then

$$\begin{aligned} [\delta + \Psi](\eta) &= [\delta + \Psi](\eta_{\text{md}}) \cos(ks) \\ &= \frac{1}{3} \Psi(\eta_{\text{md}}) \cos(ks). \end{aligned} \quad (2.12)$$

where η_{md} represents the start of the matter dominated epoch, assuming large scales, $ks_{\text{md}} \ll 1$. The quantity $\delta + \Psi$ is the *effective temperature* and can be thought of as an effective temperature in another way: after recombination, photons must climb out of the potential well to the observer and thus suffer a gravitational redshift of $\Delta T/T = \Psi$. The effective temperature fluctuation is therefore also the observed temperature fluctuation. Therefore, the large scale limit of Eq. (2.12) recovers the Sachs-Wolfe result that the observed temperature perturbation is $\Psi/3$ and overdense regions correspond to cold spots on the sky [Sachs & Wolfe, 1967] (assuming adiabatic initial conditions). Taking into account both gravity compressions and pressure enlargement, the fluid is rarefied and compressed continually. The first peak corresponds to the mode that is caught in its first compression by recombination. The second peak at roughly half the wavelength corresponds to the mode that went through a full cycle of compression and rarefaction by recombination.

The presence of baryons is not negligible in the dynamics of the acoustic oscillations.

If we consider the photon-baryon momentum density ratio $R = (p_b + \rho_b)/(p_\gamma + \rho_\gamma) \approx 30\Omega_b h^2 (z/10^3)^{-1}$. For typical values of the baryon density this number is of order unity at recombination and so we expect baryonic effects to begin appearing in the oscillations just as they are frozen in.

The baryons momentum density provides extra inertia in the joint Euler equation for pressure and potential gradients. We can put again the oscillator equation in the form of Eq. (2.8) with $\delta \rightarrow \delta + (1 + R)\Psi$ and then obtain the following solution

$$[\delta + (1 + R)\Psi](\eta) = [\delta + (1 + R)\Psi](\eta_{\text{md}}) \cos(ks). \quad (2.13)$$

Aside from the lowering of the sound speed which decreases the sound horizon, baryons have two distinguishing effects: they enhance the amplitude of the oscillations and shift the equilibrium point from zero to $\delta = -(1 + R)\Psi$.

The shifting of the zero point of the oscillator has significant phenomenological consequences. Since it is still the effective temperature $\delta + \Psi$ that is the observed temperature, the zero point shift breaks the symmetry of the oscillations and the baryons enhance only the compressional phase, i.e. every other peak. For the working cosmological model these are the first, third, fifth... Physically, the extra gravity provided by the baryons enhance compression into potential wells.

In the previous analysis we neglect the presence of imperfections in the fluid, as viscosity and heat conduction, which damp acoustic oscillations. Damping can be thought of as the result of the random walk in the baryons that takes photons from hot regions into cold and vice-versa [Silk, 1968] and the the damping scale is of order $k_d s_{rec} \approx 10$ leading to a substantial suppression of the oscillations beyond the third peak.

2.2 Polarization

The polarization field can be analyzed in a way very similar to the temperature field, save for one complication. In addition to its strength, polarization also has an orientation, depending on relative strength of two linear polarization states. Instead of using the usual Stokes parameters Q and U to describe polarization locally, the scalar E and pseudo-scalar B , linear but no-local combinations of Q and U , provide a more useful description. In complete analogy with Eq. (2.3), we can decompose E and B in terms of multipole moments, and then, following Eq. (2.4), consider the power spectra,

$$\langle E_{\ell m}^* E_{\ell' m'} \rangle = \delta_{\ell\ell'} \delta_{mm'} C_\ell^{EE}, \quad (2.14)$$

$$\langle B_{\ell m}^* B_{\ell' m'} \rangle = \delta_{\ell\ell'} \delta_{mm'} C_\ell^{BB}, \quad (2.15)$$

$$\langle a_{\ell m}^* E_{\ell' m'} \rangle = \delta_{\ell\ell'} \delta_{mm'} C_\ell^{TE}. \quad (2.16)$$

Parity invariance demands that the cross correlation between the pseudoscalar B and the scalars T or E vanishes.

The polarization spectra have several notable features. First, the amplitude of the EE spectrum is indeed down from the temperature spectrum by a factor of ten. Second, the oscillatory structure of the EE spectrum is very similar to the temperature oscillations, only they are apparently out of phase but correlated with each other. Both of these features are a direct result of the simple physics of acoustic oscillations. The final feature of the polarization spectra is the comparative smallness of the BB signal. Indeed, density perturbations do not produce B modes to first order.

Also the polarization of CMB is signed by the dissipation of the acoustic oscillations. Thomson scattering induces a linear polarization in the scattered radiation.

The E and B decomposition is simplest to visualize in the small scale limit, where spherical harmonic analysis coincides with Fourier analysis [Seljak, 1997]. Then the wavevector k picks out a preferred direction against which the polarization direction is measured. Since the linear polarization remains unchanged upon a 180° rotation, the two numbers E and B that define it represent polarization aligned or orthogonal with the wavevector (positive and negative E) and crossed at $\pm 45^\circ$ (positive and negative B).

In linear theory, scalar perturbations like the gravitational potential and temperature perturbations have only one intrinsic direction associated with them, that provided by k , and the orientation of the polarization inevitably takes its cue from that one direction, thereby producing an E -mode. The generalization to an all-sky characterization of the polarization changes none of these qualitative features. The E -mode and the B -mode are formally distinguished by the orientation of the Hessian of the Stokes parameters which define the direction of the polarization itself. This geometric distinction is preserved under summation of all Fourier modes as well as the generalization of Fourier analysis to spherical harmonic analysis.

The acoustic peaks in the polarization appear exclusively in the EE power spectrum (Eq. 2.14). This distinction is very useful as it allows a clean separation of this effect from those occurring beyond the scope of the linear perturbation theory of scalar fluctuations.

2.3 Secondary anisotropies

Beneath the peaks lies a wealth of information about the evolution of structure in the Universe and its origin in the early universe, but the CMB photons traverse the large scale structure of the Universe on their journey from the decoupling epoch, so they pick up *secondary* temperature and polarization *anisotropies*.

These anisotropies depend on all components of the Universe: dark matter, dark energy, baryonic gas density and temperature distributions, and even the existence of primordial gravity waves. Unfortunately, it is difficult to make precise predictions and measurements because of the uncertain and/or non-linear physics and because of the cosmic variance of the primary anisotropies and the relatively greater importance of galactic and extragalactic foregrounds.

Secondaries can be divided into two classes: those due to gravitational effects and those induced by scattering off of electrons.

The same balance between pressure and gravity that is responsible for acoustic oscillations determines the power spectrum of fluctuations in the non-relativistic matter.

After recombination, without the pressure of the photons, the baryons simply fall into the Newtonian potential wells with the cold dark matter.

Because the potential is constant in the matter dominated epoch, the large-scale observations set the overall amplitude of the potential power spectrum today.

On scales below the horizon at matter-radiation equality, we have seen from 2.1.1 that pressure gradients from the acoustic oscillations themselves impede the clustering of the dominant component, i.e. the photons, and lead to decay in the potential. Dark matter density perturbations remain but grow only logarithmically from their value at horizon crossing, which (just as for large scales) is approximately the initial potential, $\delta_m \approx -\Psi_i$. The potential for modes that have entered the horizon already will therefore be suppressed by $\Psi \propto -\delta_m/k^2 \sim \Psi_i/k^2$ at matter domination again according to the Poisson equation. The ratio of Ψ at late times to its initial value is called the *transfer function*. On large scales, then, the transfer function is close to one, while it falls off as k^{-2} on small scales. If the baryons fraction ρ_b/ρ_m is substantial, baryons alter the transfer function in two ways. First their inability to cluster below the sound horizon causes further decay in

the potential between matter-radiation equality. Secondly the acoustic oscillations in the baryonic velocity field kinematically cause acoustic wiggles in the transfer function [Hu & Sugiyama, 1996]. These wiggles in the matter power spectrum $P(k)$ are related to the acoustic peaks in the CMB spectrum and are visible on the largest galaxy surveys [Percival et al, 2001].

The matter transfer function and the near scale-invariant initial spectrum of fluctuations tell that by the present fluctuations in the cold dark matter or baryon density fields will have gone non-linear for all scales $k \sim 10^{-1}h\text{Mpc}^{-1}$. So there is just enough growth between $z_{rec} \approx 1100$ and $z = 0$ to explain structures in the Universe across a wide range of scales.

In particular, since this non-linear scale also corresponds to galaxy clusters and measurements of their abundance yields a robust measure of the power near this scale for a given matter density Ω_M .

More generally, the comparison between large-scale structure and the CMB is important in that it breaks degeneracies between effects due to deviations from power law initial conditions and the dynamics of the matter and energy contents of the Universe. Any dynamical effect that reduces the amplitude of the matter power spectrum corresponds to a decay in the Newtonian potential that boosts the level of anisotropy. Massive neutrinos are a good example of physics that drives the matter power spectrum down and the CMB spectrum up.

The combination is even more fruitful in the relationship between the acoustic peaks and the baryon wiggles in the matter power spectrum. Our knowledge of the physical distance between adjacent wiggles provides the ultimate standard candle for cosmology. For example, at very low z , the radial distance out to a galaxy is cz/H_0 . The unit of distance is therefore h^{-1} Mpc, and a knowledge of the true physical distance corresponds to a determination of h . At higher redshifts, the radial distance depends sensitively on the background cosmology (especially the dark energy).

2.3.1 Gravitational Secondaries

Gravitational secondaries arise from two sources: the differential redshift from time-variable metric perturbations [Sachs & Wolfe, 1967] and gravitational lensing. The former gravitational potential effects are usually called the integrated Sachs-Wolfe

(ISW) effect in linear perturbation theory, the Rees-Sciama effect in the non-linear regime, and the gravitational wave effect for tensor perturbations. Gravitational waves and lensing also produce B -modes in the polarization (see 2.2) by which they may be distinguished from acoustic polarization.

REES-SCIAMA EFFECT. This effect is due to CMB photons traversing a non-linear gravitational potential, usually associated with gravitational collapse. The relevant scales are those of galaxy clusters and superclusters, corresponding to angular scales of 5-10 arc minutes.

When we consider linear perturbations the effect is called Integrated Sachs-Wolfe (IWS) effect. It will be the key argument of the thesis and it will be dealt with in Chap. 3.

GRAVITATIONAL WAVES. A time-variable tensor metric perturbation similarly leaves an imprint in the temperature anisotropy [Sachs & Wolfe, 1967]. A tensor metric perturbation can be viewed as a standing gravitational wave and produces a quadrupolar distortion in the spatial metric. If its amplitude changes, it leaves a quadrupolar distortion in the CMB temperature distribution. Inflation predicts a nearly scale-invariant spectrum of gravitational waves. Their amplitude depends strongly on the energy scale of inflation and its relationship to the curvature fluctuations discriminates between particular models for inflation.

Gravitational waves, like scalar fields, obey the Klein-Gordon equation in a flat universe and their amplitudes begin oscillating and decaying once the perturbation crosses the horizon. While this process occurs even before recombination, rapid Thomson scattering destroys any quadrupole anisotropy that develops. This fact dictates the general structure of the contributions to the power spectrum: they are enhanced at $\ell = 2$ the present quadrupole and sharply suppressed at multipole larger than that of the first peak. As is the case for the ISW effect, confinement to the low multipoles means that the isolation of gravitational waves is severely limited by cosmic variance.

The signature of gravitational waves in the polarization is more distinct. Because gravitational waves cause a quadrupole temperature anisotropy at the end of recombination, they also generate a polarization. The quadrupole generated by a gravitational wave has its main angular variation transverse to the wavevector

itself. The resulting polarization that results has components directed both along or orthogonal to the wavevector and at 45° degree angles to it. Gravitational waves therefore generate a nearly equal amount of E and B mode polarization when viewed at a distance that is much greater than a wavelength of the fluctuation.

GRAVITATIONAL LENSING. The gravitational potentials of large-scale structure also lens the CMB photons. Since lensing conserves surface brightness, it only affects anisotropies and hence is second order in perturbation theory. The photons are deflected according to the angular gradient of the potential projected along the line of sight. This angular gradient of the projected potential peaks at a multipole $\ell \sim 60$ corresponding to scales of a $k \sim \text{few } 10^{-2} \text{ Mpc}^{-1}$. The deflections are therefore coherent below the degree scale.

This large coherence and small amplitude ensures that linear theory in the potential is sufficient to describe the main effects of lensing. Since lensing is a one-to-one mapping of the source and image planes it simply distorts the images formed from the acoustic oscillations in accord with the deflection angle. This warping naturally also distorts the mapping of physical scales in the acoustic peaks to angular scales and hence smooths features in the temperature and polarization. The smoothing scale is the coherence scale of the deflection angle $\Delta\ell \approx 60$ and is sufficiently wide to alter the acoustic peaks with $\Delta\ell \sim 300$.

For the polarization, the remapping not only smooths the acoustic power spectrum but actually generates B -mode polarization. Remapping by the lenses preserves the orientation of the polarization but warps its spatial distribution in a Gaussian random fashion and hence does not preserve the symmetry of the original E -mode. The B -modes from lensing sets a detection threshold for gravitational waves for a finite patch of sky.

Gravitational lensing also generates a small amount of power in the anisotropies on its own but this is only noticeable beyond the damping tail where diffusion has destroyed the primary anisotropies. On these small scales, the anisotropy of the CMB is approximately a pure gradient on the sky and the inhomogeneous distribution of lenses introduces ripples in the gradient on the scale of the lenses [Seljak & Zaldarriaga, 2000].

Because the lensed CMB distribution is not linear in the fluctuations, it is not

completely described by changes in the power spectrum. It is possible to use the non-Gaussianity to isolate lensing effects and their cross-correlation with the ISW effect [Seljak & Zaldarriaga, 1999]. In particular, there is a quadratic combination of the anisotropy data that optimally reconstructs the projected dark matter potentials for use in this cross-correlation. The cross correlation is especially important in that in a flat universe it is a direct indication of dark energy and can be used to study the properties of the dark energy beyond a simple equation of state.

2.3.2 Scattering Secondaries

From the observations both of the lack of a Gunn-Peterson trough [Gunn & Peterson, 1965] in quasar spectra and its preliminary detection, we know that hydrogen was reionized at $z_{ri} \simeq 6$ (Chap. 1). This is thought to occur through the ionizing radiation of the first generation of massive stars. The consequent recoupling of CMB photons to the baryons causes a few percent of them to be rescattered. Linearly, rescattering induces three changes to the photon distribution: suppression of primordial anisotropy, generation of large angle polarization, and a large angle Doppler effect..

PEAK SUPPRESSION. Like scattering before recombination, scattering at late times suppresses anisotropies in the distribution that have already formed. Reionization therefore suppresses the amplitude of the acoustic peaks by the fraction of photons rescattered, approximately the optical depth $\sim \tau_{ri}$. Unlike the plasma before recombination, the medium is optically thin and so the mean free path and diffusion length of the photons is of order the horizon itself. New acoustic oscillations cannot form. On scales approaching the horizon at reionization, inhomogeneities have yet to be converted into anisotropies and so large angle fluctuations are not suppressed.

The rescattered radiation becomes polarized since temperature inhomogeneities become anisotropies by projection, passing through quadrupole anisotropies when the perturbations are on the horizon scale at any given time. The result is a bump in the power spectrum of the E -polarization on angular scales corresponding to the horizon at reionization. Because of the low optical depth of reionization and the finite range of scales that contribute to the quadrupole, the polarization contributions are

on the order of tenths of μK on scales of $\ell \sim \text{few}$. As in the ISW effect, cancellation of contributions along the line of sight guarantees a sharp suppression of contributions at higher multipoles in linear theory.

DOPPLER EFFECT. Naively, velocity fields of order $v \sim 10^{-3}$ and optical depths of a few percent would imply a Doppler effect that rivals the acoustic peaks themselves. Since the Doppler effect comes from the peculiar velocity along the line of sight, it retains no contributions from linear modes with wavevectors perpendicular to the line of sight and these are the only modes that survive cancellation. Consequently, the Doppler effect from reionization is strongly suppressed and is entirely negligible below $\ell \sim 10^2$ unless the optical depth in the reionization epoch approaches unity.

The Doppler effect can survive cancellation if the optical depth has modulations in a direction orthogonal to the bulk velocity. This modulation can be the result of either density or ionization fluctuations in the gas and include the effect in clusters, and linear as well as non-linear large-scale structures.

SUNYAEV-ZEL'DOVICH EFFECT. Internal motion of the gas in dark matter halos also give rise to Doppler shifts in the CMB photons. Shifts that are first order in the velocity are canceled as photons scatter off of electrons moving in different directions. At second order in the velocity, there is a residual effect. For clusters of galaxies where the temperature of the gas can reach $T_e \sim 10\text{keV}$, the thermal motions are a substantial fraction of the speed of light $v_{\text{rms}} = (3T_e/m_e)^{1/2} \sim 0.2$. The second order effect represents a net transfer of energy between the hot electron gas and the cooler CMB and leaves a spectral distortion in the CMB where photons on the Rayleigh-Jeans side are transferred to the Wien tail. This effect is called the thermal Sunyaev-Zel'dovich (SZ) effect [Sunyaev & Zel'dovich, 1972]. Like all CMB effects, once imprinted, distortions relative to the redshifting background temperature remain unaffected by cosmological dimming, so one might hope to find clusters at high redshift using the SZ effect. However, the main effect comes from the most massive clusters because of the strong temperature weighting and these have formed only recently in the standard cosmological model.

The SZ effect is expected to dominate the power spectrum of secondary anisotropies, but the other secondaries are measurable. Its distinct frequency signature can be used to isolate it from other secondaries. Additionally, it mainly

comes from massive clusters which are intrinsically rare. Hence contributions to the power spectrum are non-Gaussian and concentrated in rare, spatially localized regions. Removal of regions identified as clusters through X-rays and optical surveys or ultimately high resolution CMB maps themselves can greatly reduce contributions at large angular scales where they are unresolved.

2.3.3 Foregrounds

In the CMB observations we also have to take into account the foreground emission which is not primordial.

There are three primary mechanisms for diffuse Galactic radio emission. Relativistic electrons interact with the Galactic magnetic field to produce synchrotron emission, for which the standard template is 408 MHz data. Less energetic electrons scatter from each other and ionized nuclei to produce free-free radiation (also known as thermal Bremsstrahlung), which can be traced with $H\alpha$ line emission. Finally, dust grains emit a modified blackbody spectrum through excitation of their vibrational modes, for which the standard template is the fit to data from the *Infrared Astronomical Satellite (IRAS)* and the *Cosmic Background Explorer (COBE)*. Dust grains may also emit radiation through rotational modes or other excitations.

Chapter 3

Late Integrated Sachs-Wolfe Effect

As I have aforementioned in Chap.s 1 and 2 the key subject of this thesis is the Integrated Sachs-Wolfe (ISW) effect.

This effect is due to the interactions of photons with the galaxy gravitational potentials along the line of sight from the last scattering surface to present. CMB photons pass through peaks and wells of the gravitational potential and when they fall into a potential well, photons gain energy; if the well is not evolving, the photons lose the same energy when they climb out, leaving no net change.

If the gravitational potentials decay while the photons pass through, then the energy that they lose climbing out is less than what they gained falling in, leaving a net shift in the photon temperature, a red shifting of photons which must ‘climb out’ of a different potential than they ‘fell into’. The Rees-Sciama (RS) effect arises in the same way but the ISW effect is generally taken to be the contribution from the linear evolution of the gravitational potential, while the Rees-Sciama effect arises from the non-linear evolution of the gravitational potential. While the non-linear effect (RS) is inevitable, the linear effect (ISW) depends on the cosmological model and requires that the background equation of state changes.

In a flat dark energy dominated universe the gravitational potentials associated with the large scale structures decay as consequence of the accelerated phase of expansion. In a universe with a significant cosmological constant, however, Φ becomes time dependent even in linear theory and an appreciable amount of anisotropy can be created at quite modest redshifts. CMB photons which cross these regions acquire a shift which generates temperature anisotropies. This also happens at early times as the universe goes from being radiation dominated to matter dominated (*Early* ISW effect); the effect at late times as the dark energy (or curvature) takes over from the

matter is called (*Late* ISW effect).

The ISW temperature fluctuations, $\Delta T/T$, in a particular direction \hat{n} is given by:

$$\frac{\Delta T}{T}(\hat{n}) = -2 \int_{z_i}^f e^{-\tau(z)} \frac{d\Phi}{dz}(\hat{n}, z) dz, \quad (3.1)$$

where Φ is the Newtonian gauge gravitational potential, the integral is over the redshift z , $z_f = 0$ being today and z_i being recombination and $e^{-\tau(z)}$ is the visibility function to account for a possible suppression due to early reionization (τ is the conformal time).

As we have seen, since the matter density is proportional to $\rho_m \propto a^{-3}$, the gravitational potential evolves as $\Phi \propto \delta_m/a$. In the matter dominated regime, the growth of the perturbations is given by $\delta_m \propto a$, meaning the gravitational potential is constant in time: the collapse of the perturbations is exactly balanced by the dilution of the matter.

When dark energy or curvature begins to dominate, the growth of perturbations is slowed, and the gravitational potentials begin to decay, giving rise to the late time ISW effect. Unlike the ISW perturbations generated at the earlier radiation-matter transition, the ISW anisotropies generated at late times are virtually uncorrelated with the CMB fluctuations generated at the *lss*.

In this way, the CMB sky is effectively almost composed of two independent maps, those fluctuations created at last scattering or soon afterwards, and those created at low redshifts when dark energy or curvature has become dynamically important (see Fig. 3.1, see also the simulated maps of the ISW and the total signal on the CMB created by the ISW group of Planck in Santander [Barreiro et al., 2008], Fig. 3.2). The linear effect is predominantly on very large scales, and for typical models, it is not as large as the anisotropies from the last scattering surface. It is dominated by modes which are of the horizon size, because it is these modes which will have the most time for the potential to change as the photons pass through. For smaller scale perturbations, photons can get many positive and negative smaller amplitude contributions which will tend to cancel out.

Considering the simplest model of Dark Energy, i.e. the Λ CDM model, we know that as the ρ_Λ increases, it comes to dominate the total energy density at earlier and earlier redshifts. The effect on the evolution of the potential is thus more

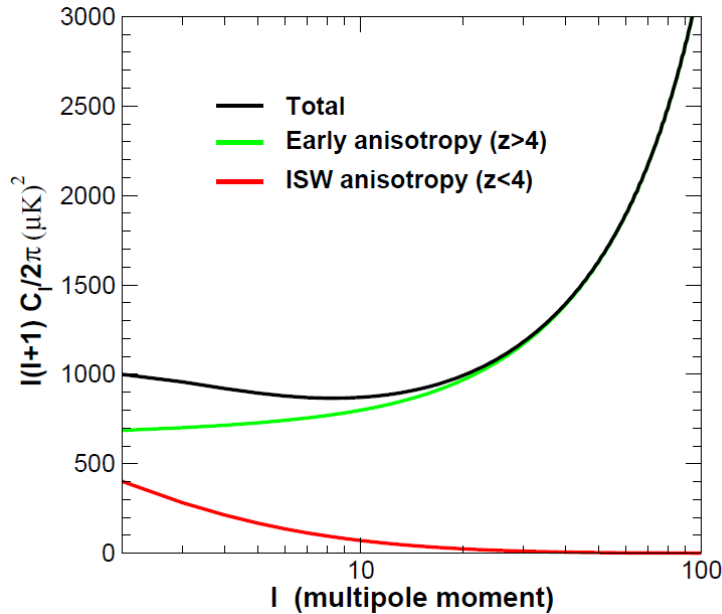


Figure 3.1: [Crittenden, 2006] Typical auto.correlation function for the ISW effect in a cosmological constant model. The late ISW adds a small amount of large scale power to the temperature maps, largely uncorrelated with the anisotropy arising from early times.

pronounced, as is the corresponding anisotropy generated at late times. For smaller values of Λ the opposite is true; the correlated anisotropy is less, but it is more concentrated at very late epochs. The cosmological constraints of Λ have also an indirect effect on the degree scale anisotropy, because in a flat universe the presence of Λ alters the matter-radiation balance at last scattering. In contrast, the large scale Rees-Sciama effect is independent of physics at high redshifts (e.g. reionization).

3.1 Cross-correlation

The direct ISW signal is very difficult to detect: unlike many foregrounds, the ISW fluctuations have the same frequency spectrum as the primordial anisotropies, so different frequency observations cannot isolate them; the attempt to search the additional power in the CMB auto-correlation spectrum also fails, because the ISW amplitude is small with respect to the SW effect; where it is largest, the cosmic variance is also large and prevails (see Fig. 3.3). If we compute the signal to noise ratio, considering all the signal is not ISW like the noise

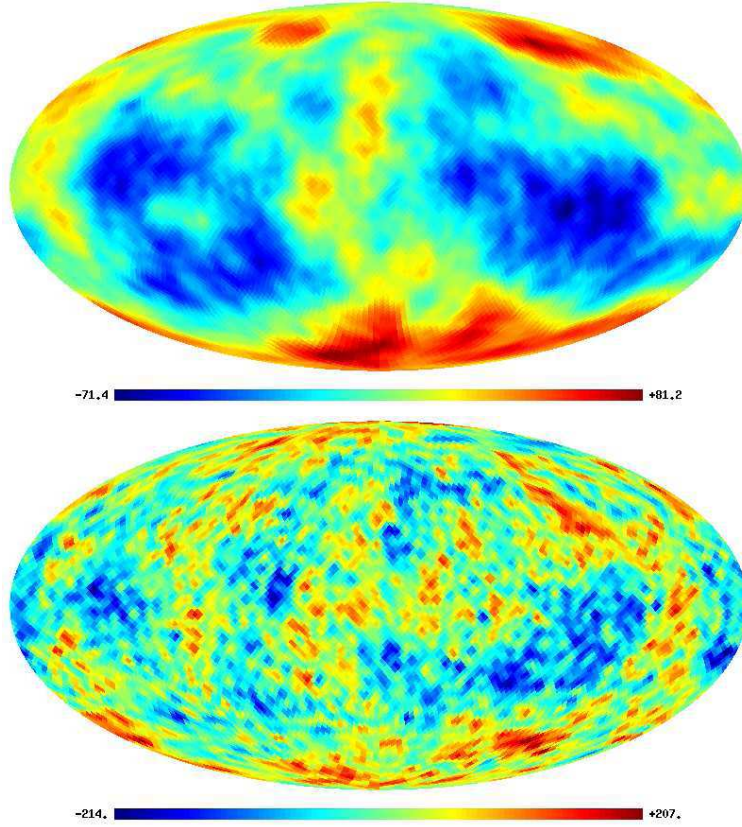


Figure 3.2: In the first panel: simulated map of the ISW signal. In the second panel: Simulated map of the total CMB signal (ISW + SW signal). We can note the difference in the scales of intensity.

$$\left(\frac{S}{N}\right)^2 = \sum_l \frac{[C_l^{ISW}]^2}{[C_l^{TT}]^2} \rightarrow \frac{S}{N} \approx 0.68 < 1 \quad (3.2)$$

we can safely confirm the ISW signal is not detectable from the total CMB map.

This problem can be overcome by considering how the Late ISW effect was produced and by examining how the ISW temperature correlates with the density of galaxies ([Crittenden & Turok1995]), which should trace the potential wells and hills which bring about the anisotropies.

The Late ISW anisotropies are produced by local ($z \leq 4$) fluctuations in the gravitational potential due to the presence of dark energy so it can be determined if it is known how the matter is distributed on large scales.

If the gravitational potential is decaying, statistically we expect overdensities of galaxies to align with temperature hot spots and under densities with temperature

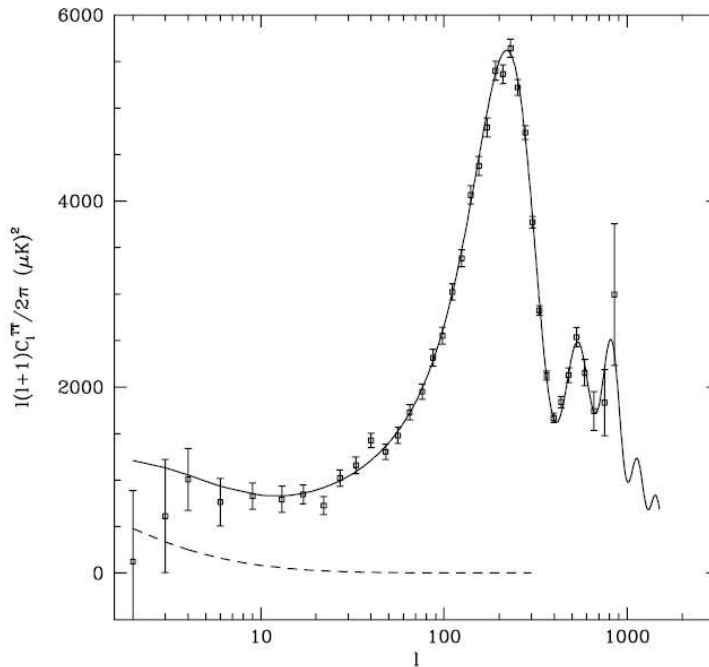


Figure 3.3: The larger error bars on the low ℓ 's are due to the maximum influence of the cosmic variance cold spots.

In order to quantify the cross-correlation between the galaxy distribution and the CMB anisotropies, the sky temperature can be expanded in the usual spherical harmonics

$$\frac{\Delta T}{T}(\hat{n}) \equiv \sum_{l,m} a_{lm} Y_{lm}(\theta, \phi), \quad (3.3)$$

where in an isotropic ensemble the a_{lm} 's coefficients obey $\langle a_{lm} a_{l'm'} \rangle = \delta_{ll'} \delta_{mm'} C_l$ where C_l is the angular power spectrum.

If there is a clump of matter, such as a cluster of galaxies in a given direction of the sky, we are likely to observe a spot in the corresponding direction of the CMB provided that the CMB photons have crossed that region during the accelerated epoch. We therefore expect to measure a positive angular correlation between CMB temperature anisotropy maps and surveys of the large scale structures.

Since part of the CMB anisotropy is associated with the gravitational potential at low redshift, it must be correlated with the matter distribution in our vicinity.

The evolution of the gravitational potential can be related to the linear density perturbation via the Poisson's equation in Fourier space. The observed galaxy

density contrast in a given direction \hat{n} will be

$$\delta_g(\hat{n}) = \int b_g(z) \frac{dN}{dz}(z) \delta_m(\hat{n}, z) dz, \quad (3.4)$$

where dN/dz is the selection function of the survey, $b_g(z)$ its galaxy bias relating the visible matter distribution to the underlying dark matter and δ_m the matter density perturbations.

The galaxy bias, $b_g(z)$, can evolve in time or as a function of scale. In our analysis we use at first a time and scale independent bias for simplicity (as [Giannantonio et al., 2008, Ho et al., 2008, Vielva, Martinez-Gonzalez & Tucci2006]) and then a redshift dependent bias (xia10b). From the point of view of the ISW-LSS cross-correlation, time dependent bias is equivalent to changing the selection function of the survey. Scale dependence of the bias is also problematic, but on the very large scales (> 10 Mpc), the scale dependence is expected to be weak.

Given a map of the CMB and a survey of galaxies, the angular auto-correlation and cross-correlation functions are defined as

$$C^{Tg}(\theta) \equiv \left\langle \frac{\Delta T}{T}(\hat{n}_1) \delta_g(\hat{n}_2) \right\rangle \quad (3.5)$$

$$C^{gg}(\theta) \equiv \langle \delta_g(\hat{n}_1) \delta_g(\hat{n}_2) \rangle, \quad (3.6)$$

with the average carried over all the pairs at the same angular distance $\theta = |\hat{n}_1 - \hat{n}_2|$ and $\Delta T/T$ and δ_g given respectively by Eq. 3.3 and Eq. 3.4.

It is possible to express these quantities in the harmonic space with the use of the Legendre polynomials P_l :

$$C^{Tg}(\theta) = \sum_{l=2}^{\infty} \frac{2l+1}{4\pi} C_l^{Tg} P_l[\cos(\theta)], \quad (3.7)$$

and the auto- and cross-correlation power spectra are given by

$$C_l^{Tg} = 4\pi \int \frac{dk}{k} \Delta^2(k) I_l^{ISW}(k) I_l^g(k) \quad (3.8)$$

$$C_l^{gg} = 4\pi \int \frac{dk}{k} \Delta^2(k) I_l^g(k) I_l^g(k), \quad (3.9)$$

where $\Delta(k)$ is the matter power spectrum $\Delta^2(k) \equiv 4\pi k^3 P(k)/(2\pi)^3$ and the two integrands are respectively

$$I_l^{ISW}(k) = -2 \int e^{-\tau(z)} \frac{d\Phi_k}{dz} j_\ell[k\chi(z)] dz \quad (3.10)$$

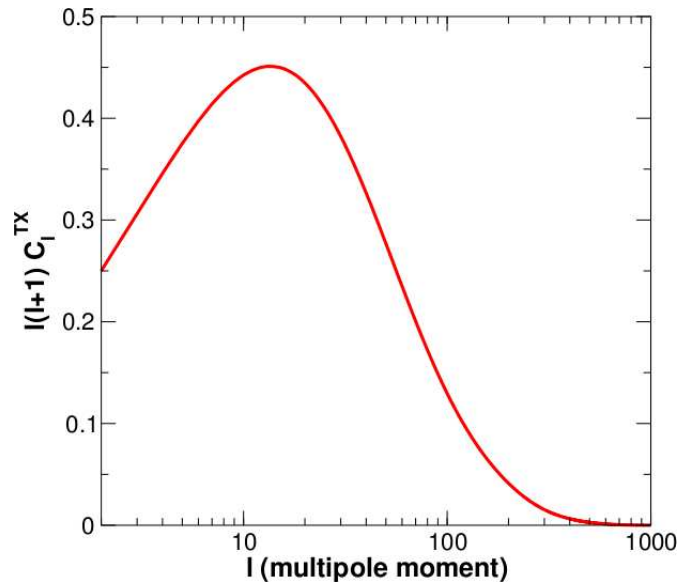


Figure 3.4: Typical cross-correlation function for the ISW effect in a cosmological constant model. The cross-correlation (here shown in arbitrary units) peaks on scales of a few degrees.

$$I_\ell^g(k) = \int b_g(z) \frac{dN}{dz}(z) \delta_m(k, z) j_\ell[k\chi(z)] dz, \quad (3.11)$$

where $\Phi_k, \delta_m(k, z)$ are the Fourier components of the gravitational potential and matter perturbations, $j_\ell(x)$ are the spherical Bessel functions and χ is the comoving distance.

The ISW effect thus generically shows up only at the lowest ℓ 's in the power spectrum ([Kofman & Starobinskii, 1985]). The ability to detect the cross-correlation is limited because the signal falls off on small scales. Not only is cosmic variance an important factor, but there is also the problem of accidental correlations between the galaxy surveys and the CMB anisotropies produced at last scattering. Many independent measurements are needed to reduce the impact of such accidental correlations. The theoretical signal to noise ratio of the cross-correlation ([Crittenden & Turok 1995], for ISW effect) is given by

$$\left(\frac{S}{N}\right)^2 = \sum_\ell (2\ell + 1) \frac{[C_\ell^{Tg}]^2}{C_\ell^{gg} C_\ell^{TT} + [C_\ell^{Tg}]^2} \approx 6.8 \quad (3.12)$$

and then by using the cross-correlation we can obtain an indirectly detection of the Late ISW signal.

Note that in this formula, the noise in the measurement of C_ℓ^{TT} and C_ℓ^{GG} is neglected.

Whereas neglecting noise in C_ℓ^{TT} for intermediate multipoles is correct - since WMAP is already essentially cosmic variance dominated on large scales -, neglecting the noise for C_ℓ^{GG} is an ideal assumption for current surveys.

3.2 Information on Dark Energy constraint in the ISW-LSS cross-correlation

As we have seen in the previous section, the ISW depends on the cosmological model and requires that the background equation of state changes. The cosmological model can be constrained estimating the cross correlations between the CMB maps and large scale distribution of matter. Detecting the cross correlations is difficult, as it requires a map of the galaxy distribution which is both deep and covers a large fraction of the sky ([Crittenden & Turok1995]). Large sky coverage is essential because the primordial fluctuations act effectively like noise when searching for anisotropies generated recently, and so the measurements are always ‘noise’ dominated (Eq. 3.2). If the sky fraction f_{sky} is small, the error to reconstruct the lower modes is large.

The first attempts of detecting the correlation using the COBE data and maps of the X-ray background (believed to trace AGN) or radio galaxy distribution produced no detections (Boughn et al. 1998; Boughn & Crittenden 2002). However, the picture improved greatly with the WMAP observations. Correlations were quickly seen with the hard X-ray background ([Boughn & Crittenden2004]), the NVSS radio galaxy survey ([Boughn & Crittenden2004]; [Nolta et al. 2004]), the APM galaxy survey [Fosalba & Gaztanaga, 2004], the SDSS ([Fosalba et al., 2003]; [Scranton et al. 2003]; [Padmanabhan et al. 2005]) and the 2MASS survey [Afshordi et al. 2003]. Whereas all the detections are at a low significance ($2 - 3\sigma$), it is encouraging that they are seen in such a broad range of surveys, from the radio and infrared to the optical and X-ray.

A Dark Energy model as the cosmological constant term Λ causes the Newtonian potential Φ to start evolving at late times, producing a significant amount of CMB anisotropy [Kofman & Starobinskii, 1985]. Since Λ comes to dominate rather suddenly, this effect is most important at rather modest redshifts. Observations of the density field allow to reconstruct the local potential which should be correlated with the CMB. Measuring this correlation thus would constrain Λ . The Poisson’s

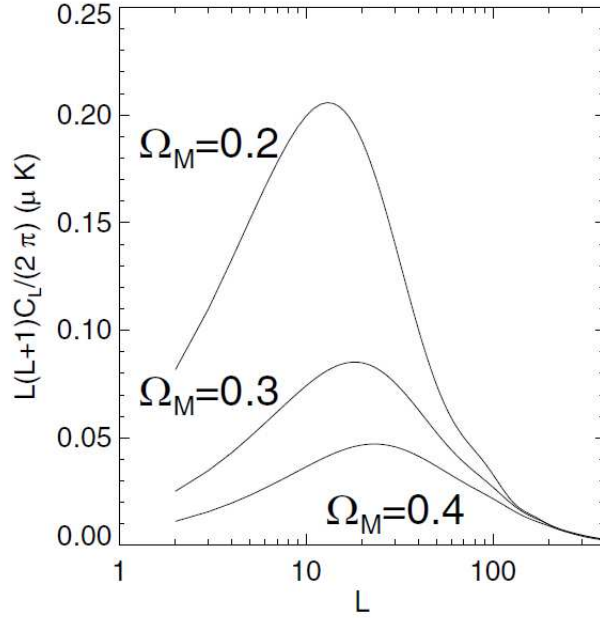


Figure 3.5: Predictions for ISW signal given the redshift distribution LRGs, $b_g = 1$, $\sigma_8 = 0.9$, and a flat universe. The different curves show the effect of changing the matter density. In particular, the effect becomes stronger as the matter density decreases ([Padmanabhan et al., 2005]).

equation contains the matter parameter Ω_M :

$$k^2\Phi = \frac{3}{2}H_0^2\Omega_M\frac{\delta_m}{a} \quad (3.13)$$

where in the assumption of a flat universe, $\Omega_M + \Omega_{DE} = 1$. The cosmological information is also contained in δ_m in the growth factor $D(a)$, as the time evolution of the matter distribution is

$$\delta_m(k, a) = D(a)\delta_m(k) \quad (3.14)$$

In Fig. 3.5 ([Padmanabhan et al., 2005]) it is possible to see how the cross-correlation power-spectrum changes with the Ω_M parameter.

As we have seen in the previous chapter, the potential on a given scale decays whenever the expansion is dominated by a component whose effective density is smooth on that scale. This occurs at late times in an $\Omega_M < 1$ model at the end of matter domination and the onset Dark Energy (or spatial curvature) domination. If the potential decays between the time a photon falls into a potential well and when it climbs out it gets a boost in temperature of $\delta\Psi$ due to the differential gravitational

Author	CMB	LSS Tracer	Wavelength	Method	Claimed Detection
Boughn & Crittenden (2002)	COBE	XRB	Xray	D2	No
Giannantonio et al. (2008)	W3			D2	2.7σ
Boughn & Crittenden (2004, 2005)	W1	XRB/NVSS	Xray/Radio	D2	'tentative' ($2-3\sigma$)
Fosalba et al. (2003)	W1	SDSS DR1		D2	2σ (low z) 3.6σ (high z)
Cabr�e et al. (2006)	W3	SDSS DR4	Optical	D2	$> 2\sigma$
Giannantonio et al. (2008)	W3	SDSS DR6		D2	2.2σ
Sawangwit et al. (2010)	W5	SDSS DR5		D2	'marginal'
L�opez-Corredoira et al. (2010)	W5	SDSS DR7		D2	'No detection'
Giannantonio et al. (2006)	W3	SDSS Quasars	Optical	D2	2σ
Giannantonio et al. (2008)	W3	SDSS Quasars		D2	2.5σ
Xia et al. (2009)	W5	SDSS Quasars		D2	2.7σ
Scranton et al. (2009)	W1			D2	$> 2\sigma$
Padmanabhan et al (2004)	W1			D1	2.5σ
Granett et al. (2009)	W3	SDSS LRG	Optical	D1	2σ
Giannantonio et al. (2008)	W3			D2	2.2σ
Sawangwit et al. (2010)	W5	SDSS LRG, 2SLAQ		D2	'marginal'
Sawangwit et al. (2010)	W5	AAOmega LRG		D2	Null
Fosalba & Gazta�naga (2004)	W1	APM	Optical	D2	2.5σ
Afshordi et al. (2004)	W1			D1	2.5σ
Rassat et al. (2007)	W3	2MASS	NIR	D1	2σ
Giannantonio et al. (2008)	W3			D2	0.5σ
Francis & Peacock (2010)	W3			D1	'weak'
Boughn & Crittenden (2002)	COBE			D2	No
Nolta et al. 2004	W1			D2	2.2σ
Pietrobon et al. (2006)	W3	NVSS	Radio	D3	$> 4\sigma$
Vielva et al. 2006	W3			D3	3.3σ
McEwen et al. (2006)	W3			D3	$> 2.5\sigma$
Raccanelli et al. (2008)	W3			D2	2.7σ
McEwen et al. (2008)	W3			D3	$\sim 4\sigma$
Giannantonio et al. (2008)	W3			D2	3.3σ
Hern�andez-Montea�gudo (2009)	W3			D1	$< 2\sigma$
Sawangwit et al. (2010)	W5			D2	'marginal' ($\sim 2\sigma$)
Corasaniti et al. (2005)	W1			D2	$> 2\sigma$
Gazta�naga (2006)	W1			D2	2σ
Ho et al. (2008)	W3	Combination	Combination	D1	3.7σ
Giannantonio et al. (2008)	W3			D2	4.5σ

Table 3.1: From [Dup e et al, 2011] Meta-analysis of ISW detections to date and their reported statistical significance. The 'Method' describes the space in which the power spectrum analysis is done (configuration, spherical harmonic, etc . . .), not the method for measuring the significance level of the detection. **D1** corresponds to spherical harmonic space, **D2** to configuration space, **D3** to wavelet space. The highest detections are made in wavelet space. Regarding the survey used, the highest detections are made using NVSS (though weak and marginal detections using NVSS are also reported) or using combinations of LSS surveys as the matter tracer.

redshift and $-\delta\Phi \approx \delta\Psi$ due to an accompanying contraction of the wavelength.

The potential decay due to Dark Energy or curvature at late times induces much different changes in the anisotropy spectrum.

The ISW effect is especially important because it is extremely sensitive to the Dark Energy: its amount, equation of state and clustering properties.

At small angles the angular cross-correlation is characterized by a nearly constant plateau, while it rapidly vanishes at larger angles ($\theta > 10^\circ$, $\ell < 20$). The overall amplitude of the signal up to small angles is particularly sensitive to the equation of state, w . In Chap. 1 we consider the case for a perfect fluid Dark Energy model in which $\delta p_X = c_X^2 \delta \rho_X$. Dark Energy, if it is not a plain cosmological constant, possesses small inhomogeneities which interact gravitationally with the inhomogeneities in baryons, dark matter and relativistic matter. The physical properties of DE perturbations constitute additional ingredients which can impact the CMB anisotropies and LSS. Then the general pressure perturbation equation is

$$\delta p_X = c_s^2 \delta \rho_X + 3H(1+w) \frac{\theta_X \rho_X}{k^2} \left(c_s^2 - \frac{\dot{p}_X}{\dot{\rho}_X} \right), \quad (3.15)$$

where ρ_X , $\delta \rho_X$, c_s^2 and θ_X are respectively the DE density, density perturbation, sound speed and velocity potential [Abramo, Finelli & Pereira, 2004]. In Fig. 3.6 we consider the Dark Energy speed of sound $c_s = 1$, the amplitude has a maximum around $w = -1$ and slowly decreases for decreasing values of w , while it rapidly falls to zero for $w \rightarrow 0$, this is because the Dark Energy contribution to the ISW effect is mainly due to the background expansion. In fact for models with $w > -1$, as $w \rightarrow 0$ the Dark Energy driven expansion is less accelerated and tends to the matter dominated behavior. Hence the variation of the gravitational potentials is smaller and consequently produces a negligible amount of ISW as $w \rightarrow 0$. Similarly for models with $w < -1$, the Dark Energy affects the expansion later than in models with $w \geq -1$. This effectively extends the period of matter domination which leads to a lower ISW signal.

Since a smaller ISW signal can be compensated by increasing the amount of Dark Energy density Ω_{DE} , a precise degeneracy line in the $\Omega_{DE} - w$ plane is expected. In particular lower negative values of w will be counterbalanced by higher values of Ω_{DE} .

In Fig. 3.7, on the contrary for $c_s = 0$, the amplitude of the cross-correlation is a monotonic decreasing function of w . In this case the decay of the gravitational

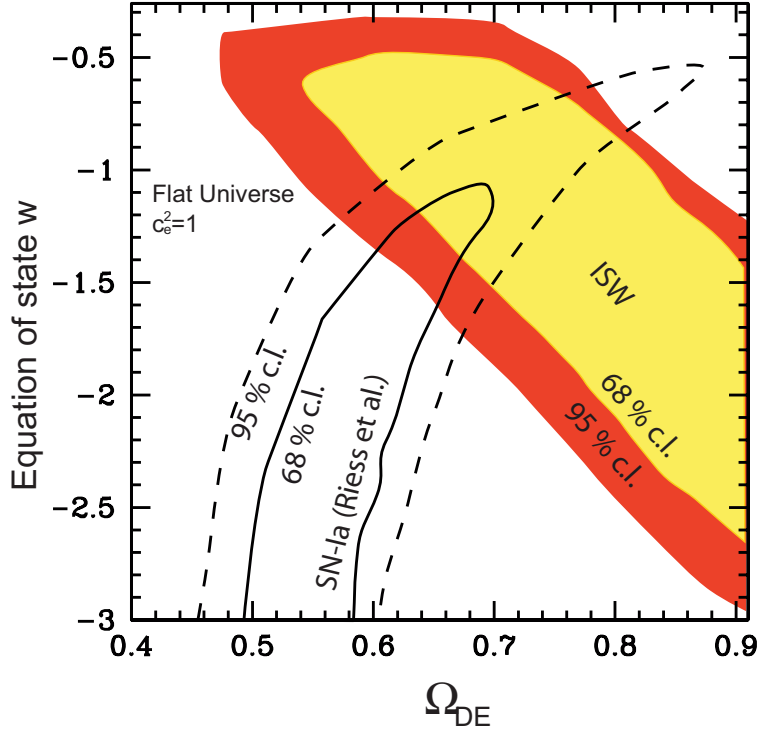


Figure 3.6: Two-dimensional marginalized likelihoods on $\Omega_{DE} - w$. The yellow and red area correspond to 1 and 2σ limits inferred from the ISW data for $c_s^2 = 1$. Solid and dash lines represent the 1 and 2σ contours from the SN-Ia data [Corasaniti et al., 2005].

potential is sensitive to the clustering of Dark Energy which is more effective as w decreases. Thus the amplitude of the ISW increases as w decreases. Again the degeneracy in the $\Omega_{DE} - w$ plane is expected to be orthogonal to the previous case. In fact increasing Ω_{DE} will compensate for larger values of w .

This trend hold independently of the selection function as long as it is centered in a range of redshifts up $z \sim 0.7 - 0.8$ for models with $w \geq -1$. However one might expect this to not be the general situation in the case of Dark Energy models with a time dependent equation of state.

In [Giannantonio et al., 2008] it can be seen that for $z > 0.2$ the signal decreases with the redshift in way that is strongly dependent on the Dark Energy parameters. Note that these plots extend in a phenomenological way across $w = -1$ line which divides very different theoretical proposals for Dark Energy.

Therefore redshift measurements of the cross-correlation are a potentially powerful tool to distinguish between different dark energy models.

Hence a sharper selection function gives a smaller cross-correlation signal,

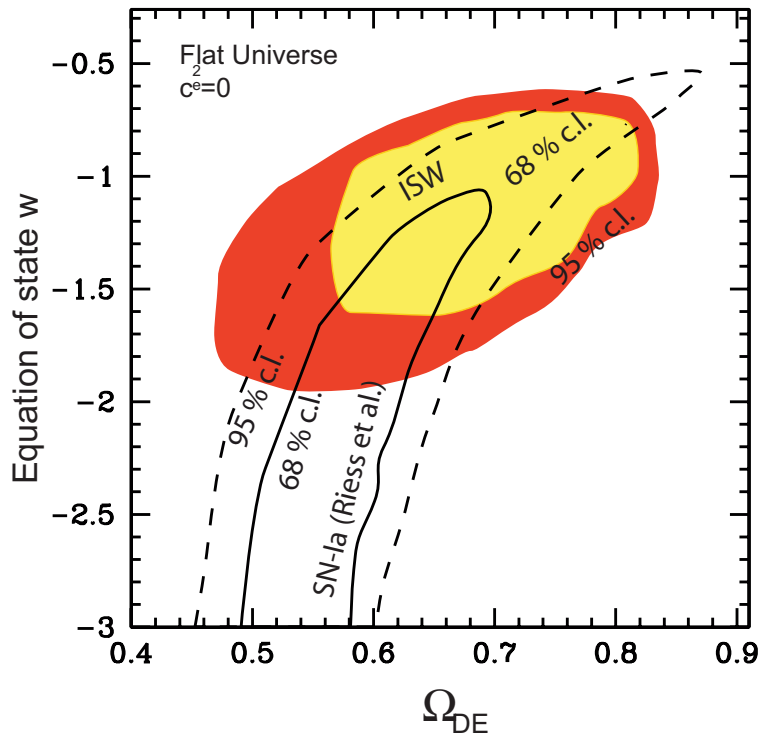


Figure 3.7: As in Fig. 3.6 with $c_s^2 = 0$ prior ([Corasaniti et al., 2005]).

eventually leading to larger uncertainties. On the other hand increasing the number of uncorrelated redshift bins would allow a better reconstruction of the redshift evolution of the cross-correlation.

A redshift dependent bias can also in principle mimic the redshift evolution of the cross-correlation predicted by different Dark Energy models.

One of the advantages of testing Dark Energy with the cross-correlation is that it is insensitive to other parameters which limits common Dark Energy parameter extraction analyses involving CMB temperature and polarization anisotropy spectra. For instance the ISW correlation is not affected by a late reionization or by an extra background of relativistic particles which change the CMB spectra through the early-ISW. The ISW-correlation is also independent of the amplitude of tensor modes and depends uniquely on the scalar perturbations, since a primordial background of gravity waves is uncorrelated with present large scale structure distribution.

There is little sensitivity to the scalar spectral index n_s , while the dependence on the baryon density Ω_b can be non-negligible. In fact the presence of baryons inhibits the growth of CDM fluctuations between matter-radiation equality and photon-

baryon decoupling causing the matter power spectrum to be suppressed on scales $k > k_{eq}$ for increasing values of Ω_b (k_{eq} is the scale which enters the horizon at the first equality). Over the range of scales which contribute to the ISW-correlation ($k \sim 0.01$) the sensitivity on Ω_b is still present.

The measure of the ISW signal can be done in various statistical spaces. In Table 3.1, [Dupé et al, 2011] classify detection into three measurement ‘domains’: D1 corresponds to spherical harmonic space; D2 to configuration space and D3 to wavelet space.

There are only two analyses which use COBE as CMB data with XRB and NVSS data,[Boughn & Crittenden, 2002], and both report null detections, which can reasonably be due to the low angular resolution of COBE even at large scales. The rest are done correlating WMAP data from years 1, 3 and 5 (respectively ‘W1’, ‘W3’ and ‘W5’ in Tab. 3.1).

Most ISW detections reported in Tab. 3.1 are relatively ‘weak’ ($< 3\sigma$) and this is expected from theory for a concordance cosmology. Higher detections are reported for the NVSS survey [Pietrobon et al. 2006, McEwan et al. 2007, Giannantonio et al. 2008], though weak and marginal detections using NVSS data are also reported [Hernández-Monteagudo 2009, Sawangwit et al. 2010]. High detections are often made using a wavelet analysis [Pietrobon et al. 2006, McEwan et al. 2007], though a similar study by the same authors using the same data but a different analysis method finds a weaker signal [McEwan et al. 2006]. The highest detection is reported using a tomographic combination of all surveys XRB, SDSS galaxies, SDSS QSOs, 2MASS and NVSS, Giannantonioetal2008, as expected given the larger redshift coverage of the analysis.

Several analyses have been revisited to seek confirmation of previous detections. In some cases, results are very similar ([Padmanabhan et al. 2004, Granett et al. 2009, Giannantonio et al. 2008], for SDSS LRGs; [Giannantonio et al. 2006, Giannantonio et al. 2008] for SDSS Quasars; [Afshordi et al. 2003, Rassat et al 2007], for 2MASS), but in some cases they are controversially different (for e.g. [Pietrobon et al. 2006] and [Sawangwit et al. 2010], for NVSS or [Afshordi et al. 2003] and [Giannantonio et al. 2008], for 2MASS).

We also notice that as certain surveys are revisited, there is a trend for the statistical significance to be reduced: for e.g., detections from 2MASS decrease

from a 2.5σ detection [Afshordi et al. 2003], to 2σ [Rassat et al 2007], to 0.5σ [Giannantonio et al. 2008] to ‘weak’ [Francis et al. 2010]. Detections using SDSS LRGs decrease from 2.5σ [Padmanabhan et al. 2004], to $2 - 2.2\sigma$ [Granett et al. 2009, Giannantonio et al. 2008], to ‘marginal’ [Sawangwit et al. 2010]. Furthermore, there tends to be a ‘sociological bias’ in the interpretation of the confidence on the signal detection. The first detections interpret a $2 - 3\sigma$ detection as ‘tentative’ [Boughn & Crittenden, 2003, 2004], while further studies with similar detection level report ‘independent evidence of dark energy’ [Afshordi et al. 2003, Gaztañaga et al. 2004].

Chapter 4

CMB and LSS data

In this chapter we present the data used to estimate the cross-correlation ISW-LSS and which theoretical models characterize the angular power spectra. It is very important to have a good knowledge of the theoretical temperature and galaxy distributions.

4.1 Cosmic Microwave Background Data

For CMB data we make use of publicly available products ¹. In particular the WMAP-7year release, clean maps at the V and W frequency bands have been co-added, using a weighting procedure that accounts for the instrumental noise variance per pixel. These frequency maps have been cleaned following a template fitting approach [Gold et al.2011], and are those used by the WMAP team to perform cosmological tests, such as constraining non-Gaussianity [Komatsu et al., 2011]. The co-added map has been degraded from its original $N_{side} = 1024$ down to $N_{side} = 32$, since the angular scales associated to this resolution ($\approx 2^\circ$) is enough to capture almost all the signal in the CMB-LSS cross-correlation expected from the ISW effect. Following this, the WMAP KQ75 Galactic mask (similarly degraded) is applied to the co-added map, in order to mitigate the unavoidable foreground contamination in regions within and near the Galactic plane, and also to remove known and intense extragalactic objects such as the Magellenic clouds and large clusters near the northern Galactic pole. Finally, the remaining monopole and dipole moments outside the mask have been estimated and removed. In Fig. 4.1 we show the masked WMAP7 maps we use in our analysis at the resolution of $N_{side} = 32$ and in mK units.

¹<http://lambda.gsfc.nasa.gov/>

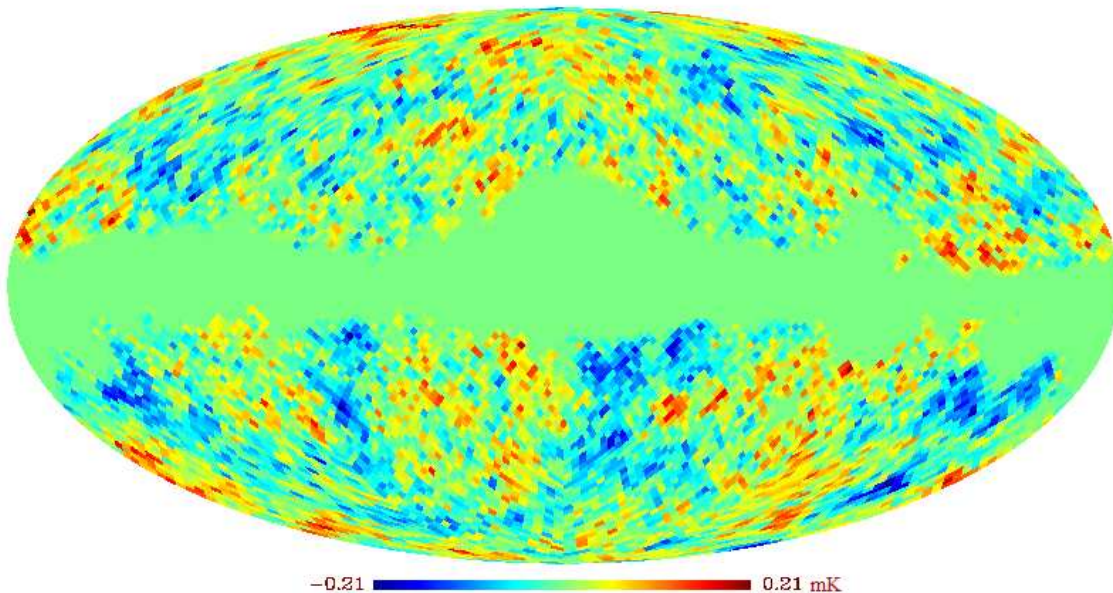


Figure 4.1: WMAP-7year masked map. This map is clean thanks to the previous finicking work of foreground component separation (by WMAP team).

4.2 Large Scale Structures Data

Many large scale structure maps are available in order to quantize the distribution of galaxies dN/dz . As it is shown in Tab. 3.1 many efforts have been done to detect the ISW signal, cross-correlating the CMB map with several large scale structure maps and different methods (the method used in this thesis will be introduced in Chap. 5).

The most common used surveys are:

- 2-Micron All Sky Survey (2MASS), infrared ($2\mu m$) survey of both hemispheres with an observed area of 27191 deg^2 (Mount Hopkins, Arizona, for the northern and Cerro Tololo/CTIO, Chile, for the southern hemisphere); the mean redshift is ~ 0.1 .
- Sloan Digital Sky Survey (SDSS), for photometric Luminous Red Galaxies (LRG) and Quasars (QSO), survey on five optical bands of about 10^4 deg^2 of the high-latitude sky; the redshift range is $0.31 < z < 1.67$.
- NRAO VLA Sky Survey (NVSS), radio survey with the largest sky coverage (27361 deg^2) and the highest number of galaxies (1104983, for a flux cut of

Table 4.1: The large-scale structure data summary.([Ho et al., 2008])

Sample	Area deg ²	Density deg ⁻²	Number of galaxies	b_{eff}	$\langle z \rangle_b$
2MASS, $12.0 < K_s < 12.5$	27 191	1.84	50 096	1.63	0.06
2MASS, $12.5 < K_s < 13.0$	27 191	3.79	103 060	1.52	0.07
2MASS, $13.0 < K_s < 13.5$	27 191	7.85	213 516	1.54	0.10
2MASS, $13.5 < K_s < 14.0$	27 191	16.0	435 570	1.65	0.12
SDSS, LRG, low- z	6 641	35.1	232 888	1.97	0.31
SDSS, LRG, high- z	6 641	93.8	622 646	1.98	0.53
SDSS, QSO, low- z	6 039	20.8	125 407	2.36	1.29
SDSS, QSO, high- z	6 039	18.3	110 528	2.75	1.67
NVSS point sources	27 361	40.3	1 104 983	1.98	1.43

Table 4.2: Signal-to-noise ratio for each survey

Sample	f_{sky}	S/N
2MASS	0.66	0.58
SDSS, LRG	0.16	2.22
SDSS, QSO	0.15	2.68
NVSS	0.85	6.80

2mJ); the mean redshift is 1.43.

Some features for these surveys are summarized in Tab. 4.1 ([Ho et al., 2008]).

In order to study the ISW effect on the largest scales, the most important feature for a LSS map is the f_{sky} , the fraction of the observed sky and consequently the highest number of galaxy. Today the best survey for this aim is the NVSS. We can compute for each survey forementioned above the signal-to-noise ratio of the cross-correlation (see Eq. (3.12))

$$\left(\frac{S}{N}\right)^2 = \sum_{\ell} \frac{f_{\text{sky}}(C_{\ell}^{Tg})^2(\ell+1)^2}{[C_{\ell}^{TT}C_{\ell}^{GG} + (C_{\ell}^{TG})](\ell/2+1)} \quad (4.1)$$

where C_{ℓ}^X is the theoretical angular power spectrum for the X(auto or cross)-correlation. Considering the same known angular power spectrum for the temperature (WMAP7-like autospectrum), the galaxy-galaxy autospectrum (GG) change for each survey, with a particular bias $b_g(z)$ and galaxy distributions dN/dz , as we have seen in Chap. 3, in Eq. (3.11). The Tab. 4.2 shows the different signal-to-noise ratios for each survey, it is clear how the NVSS is the best survey to study the ISW effect.

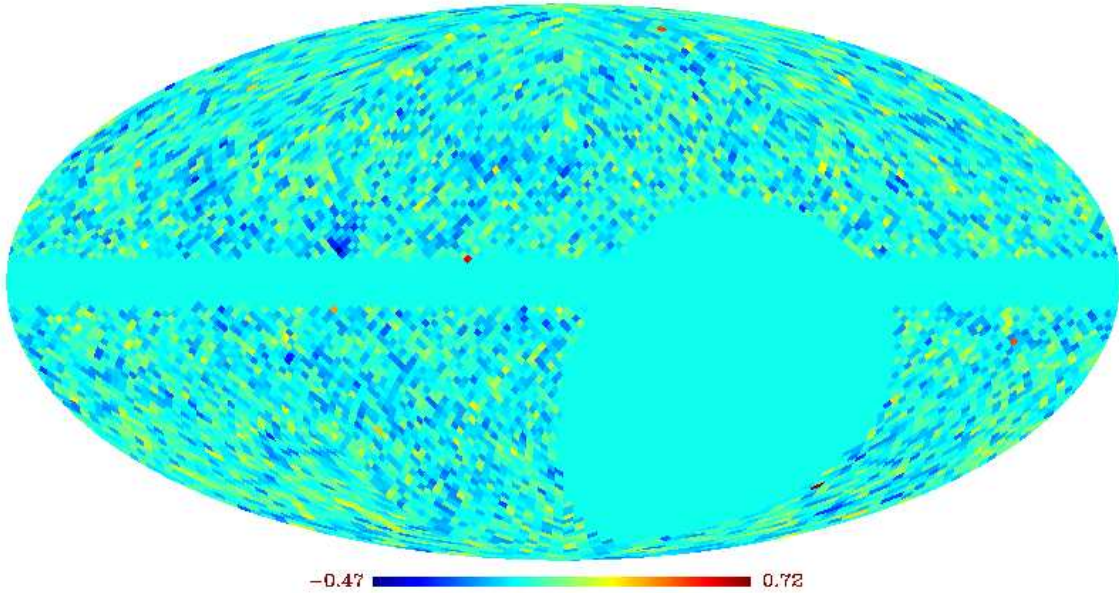


Figure 4.2: Masked NVSS map with 2.5mJy flux cut.

4.3 NVSS

The NRAO VLA Sky Survey (NVSS) is a 1.4 GHz continuum survey covering the entire sky north of -40° declination ($f_{sky} \approx 85\%$) obtained using the compact D and DnC configurations of the Very Large Array (VLA) [Condon et al., 1998]. The images all have 45 arcsec FWHM resolution and nearly uniform sensitivity and yield a catalog of almost 2×10^6 discrete sources stronger than ~ 2.5 mJy.

This survey has been widely used in the context of the ISW studies. It was first used by [Boughn & Crittenden, 2002] to probe the CMB-LSS cross-correlation with the COBE data, and a few years afterwards it was successfully used by the same authors with WMAP data, in the first work reporting such cross-correlation [Boughn & Crittenden2004]; this was soon followed by [Nolta et al. 2004] with a similar analysis by the WMAP team. In Fig. 4.3 we show the NVSS map use in our analysis at resolution $N_{side} = 32$ for a flux cut of 2.5mJy and with no units but counts of sources $(n_{pix} - \bar{n})/\bar{n}$, where n_{pix} is the number of galaxies per pixel and \bar{n} the mean galaxy number of the map given by the ratio between the total number of galaxies and the number of no-masked pixels, $\frac{N_{gal}}{N_{obspixel}}$.

4.3.1 Systematics and pre-processing

This survey has several systematics [Ho et al., 2008]: galactic synchrotron emission, spurious power from bright sources and a declination-dependent striping problem, different configurations of the VLA antennas (Condon 1998). All of these have to be treated properly before one can claim that the power coming from the cross or auto-correlation is not due to some spurious issues.

GALACTIC SYNCHROTRON EMISSION. The Galactic synchrotron emission can in principle be an issue because it contributes significantly to the noise temperature of the VLA, and for realistic number counts, increased noise temperature could change the number of sources with measured flux above some threshold. This issue is treated [Ho et al., 2008] by incorporating a template in the cross-correlation analysis and projecting out the power that are correlated to this template. Even though the Haslam map is at 408 MHz, the frequency dependence of the galactic synchrotron emission is fairly flat, allowing to use it as a template of the Galactic synchrotron radiation.

DOUBLE SOURCES. It was considered the possibility of double counting in NVSS, or the possibility of the existence of sources which are so close each to other that they are the same source. It has been made a NVSS map at $N_{side} = 4096$, where a pixel correspond to a FWHM of 48.4" (assuming a gaussian beam). This value is a little higher than the NVSS FWHM (45"). Then it can be identified the double counts looking at the pixels at $N_{side} = 4096$ with more than one count; the maximum number of counts in a pixel at this resolution is two.

The number of double counts (1589) with respect to the total number of counts (1 657 106) was about 0.1%, most of the double counts were in the galactic plane. It was so proved this issue does not change the angular power spectrum.

DECLINATION-DEPENDENT STRIPING. The survey has a somewhat inhomogenous sensitivity as a function of the equatorial declination, resulting in the mean galaxy density that artificially varies with the declination. Therefore, some pre-processing is needed in order to mitigate this large-scale effect. One of the procedures used in the literature consists in defining iso-latitude bands (in equatorial

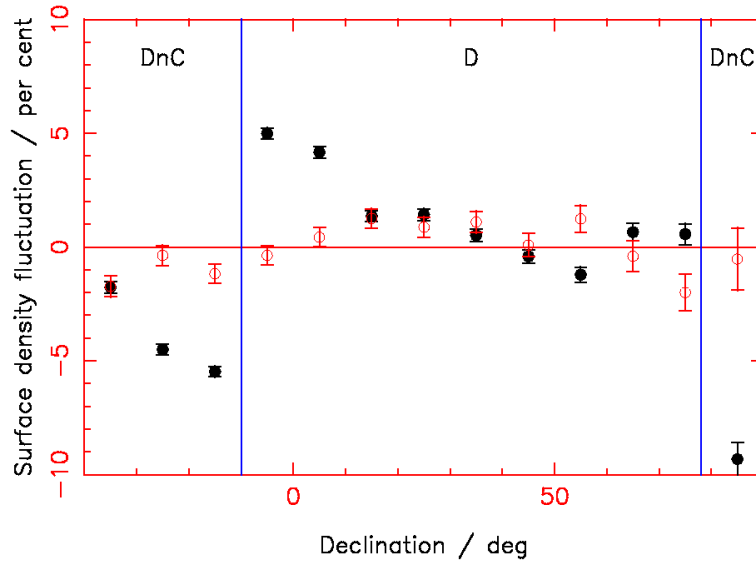


Figure 4.3: Variations in NVSS source density as a function of declination for flux thresholds 2 mJy (filled circles) and 10 mJy (open circles). The declination range of each array configuration is also indicated. The error bar on the number of sources N in a bin is \sqrt{N} . Masked regions are excluded from measurement of [?]

coordinates) and imposing that these bands have the same mean galaxy density. In our case, this pre-processing consists of selecting first the sources above a particular flux cut, and then defining nine bands of equal area, imposing the same mean galaxy density number for each band. Finally, we rotate to Galactic coordinates to compare to WMAP, and then pixelise to a HEALPix (cite Gorski) resolution of $N_{side} = 32$. This declination-dependent striping problem change with the flux cut.

In Fig. 4.3 (Jasper Wall 2002), declination-dependent variations occur at flux densities below 10 mJy, including significant jumps at the declinations at which the array configuration changes.

(For the test on the code see Chap. 6)

ANTENNA CONFIGURATIONS. Observations were conducted by the VLA in two different configurations: the D configuration was used for ecliptic latitudes in the range $b_E \in [-10^\circ, 78^\circ]$, while the DnC configuration was used under large zenith angle ($b_E < -10^\circ, b_E > 78^\circ$). As noted by [Blake & Wall, 2002], this change of configuration introduced some systematics in the galaxy number density. In Fig. 4.4 the fluctuations of the radio galaxy number density (around its mean) are plotted versus ecliptic latitude for NVSS sources after considering three different

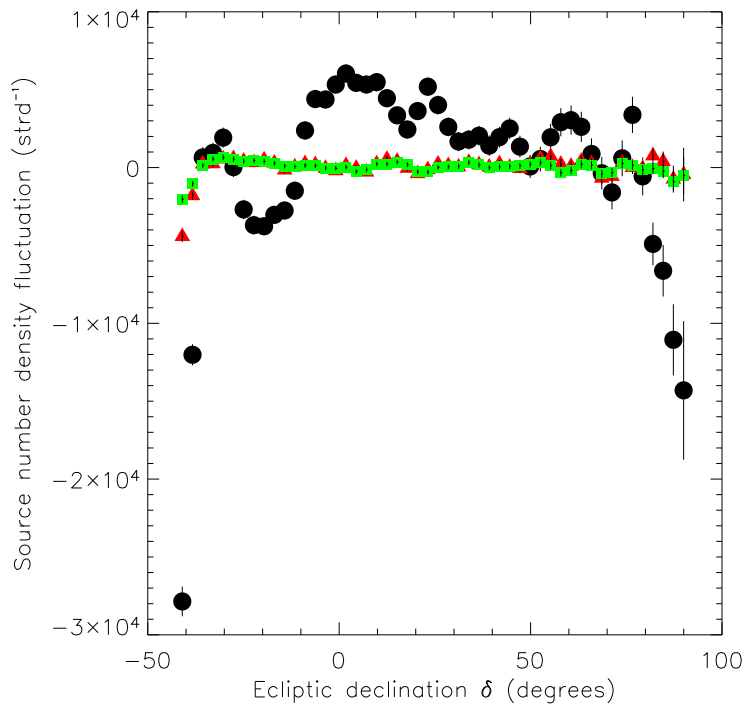


Figure 4.4: Variations of the NVSS radio galaxy fluctuation versus ecliptic declination for sources brighter than 2.5mJy (black circles), 30 mJy (red triangles) and 60mJy (green squares) [Hernandez-Monteaugudo, 2010].

flux thresholds: black circles display the case where the threshold has been imposed at 2.5 mJy, while red triangles and green squares correspond to 30 mJy and 60 mJy, respectively (Monteaugudo 2010). It is clear that dim sources are strongly affected by the VLA configuration, since the number density fluctuations changes dramatically for the declinations $b_E = -10^\circ, 78^\circ$ where the observing configuration is switched. This does not appreciably happen for the brightest sources (thresholds at 30 and 60 mJy), which show a rather flat pattern versus declination. BRIGHT SOURCES. The bright sources are problematic since the VLA has a finite dynamic range (~ 1000 in snapshot mode with limited uv -plane coverage) and thus the identification of faint sources in fields with a bright source is unreliable. This issue is mitigated by masking out all the bright sources. When pointing to a bright radio source, side lobes usually show up surrounding it and being counted as spurious dim sources in the catalog. Although potentially of relevance, this effect should be avoided in the brightest radio sources, since the point source mask built by WMAP team typically cancels a circle of radius 0.6° around the bright radio sources detected by this experiment. To deal

Table 4.3: Number of galaxies for the three considered flux cuts.

Flux cut (mJy)	Galaxy Number	f_{sky}	Galaxy Number per pixel
2.5	1 450 270		161.6
5.0	846 726	0.73	94.4
10.0	509 250		56.8

with the above potential problems, [Ho et al., 2008] impose a flux limit of 2.5 mJy (where NVSS is 50% complete), mask out a 0.6 degree radius around all the bright sources (> 2.5 Jy).

Another reason to use the NVSS in an ISW context is the fact that luminous Active Galactic Nuclei (AGNs) are supposed to be good tracers of the density field at high redshift. However, among NVSS radio galaxies, one should, a priori, distinguish two different source populations, namely high luminosity AGNs and nearby Star Forming Galaxies (SFGs). If the contribution of the latter population is not negligible, then it might distort our template of the high redshift density distribution by adding a very low redshift galaxy sample. It is known most of the ISW signal is generated in the redshift range $z \sim [0.5, 1.1]$, and therefore ideally the galaxy survey should probe this epoch. The SFGs are placed at very low redshift ($z < 0.01$) and for this reason provide no information in terms of ISW studies. They are intrinsically less luminous sources in the radio, and, as shown by Condon et al. (1998), dominate the source counts in the low flux end. According to Condon et al. (1998), they contribute to a $\sim 30\%$ of the total number of weighted source counts at 1 mJy, but this contribution should drop rapidly at larger fluxes measured at 1.4 GHz. However, this constitutes another argument to test how correlation tests depend on the flux cut applied to NVSS sources. In our analyses (Chap. 6), we build three different galaxy templates out of NVSS data, each of them corresponding to flux thresholds at 2.5, 5 and 10 mJy (in Table 5.1 there are the corresponding galaxy number for each flux cut, considering a HEALPix pixelization with $N_{side} = 32$ and so $N_{pix} = 12 \times N_{side}^2 = 12\,288$).

4.3.2 Source redshift distribution

To interpret the results of our measurements, we must assume some redshift distribution dN/dz and potentially redshift dependent bias $b(z)$ for the sample. Historically, the redshift distribution was based on models of the sources by [Dunlop & Peacock, 1990], and a time-independent bias of 1.6 was derived by [Boughn & Crittenden, 2002]. A larger time-independent bias was found by [Blake, Ferreira & Borril, 2004]), albeit with a different redshit distribution with respect to [Boughn & Crittenden, 2002].

In our analysis we use two different galaxy distributions.

- The first and main galaxy distribution we consider in our analysis are the redshift distribution based on a Γ distribution fit which was constrained to give the cross-correlations measured between the NVSS survey and SDSS LRG subsamples ([Ho et al., 2008]):

$$\frac{dN^{\text{Ho}}}{dz} = \frac{\alpha^\alpha}{z_*^{\alpha+1}\Gamma(\alpha)} z^\alpha e^{-\alpha z/z_*}, \quad (4.2)$$

where $z_* = 0.79$ and $\alpha = 1.18$. [Ho et al., 2008] also estimates an effective, redshift independent value for the bias as $b(z) = 1.98$.

In the Eq. (3.4) of Chap. 3 the function dN/dz has to be characterized and for NVSS is the hardest to obtain because there are no spectroscopic samples of NVSS objects that have sufficiently high completeness to obtain the redshift distribution. Past ISW analyses [Boughn & Crittenden2004, Nolta at al. 2004] with the NVSS have been based on the radio luminosity function $\Phi(L, z)$ of Dunlop & Peacock [Dunlop & Peacock, 1990], which itself was fit to a combination of source counts, redshifts for some of the brightest sources, and the local luminosity function. It was assumed a constant bias and the redshift distribution so obtained was reasonable, however it had three major drawbacks: the redshift probability distribution for the faint sources (which make up most of the sample) was constrained only by the functional form used for the luminosity function and not by the data; it did not give the redshift dependence of the bias, which could be very important since the redshift range is broad, and the typical luminosity of the sources varies with redshift; the absolute bias b was constrained using the NVSS autopower spectrum, which is known to contain power of instrumental origin.

The alternative method to measure $f(z)$ is by cross-correlation against the other samples whose redshift distributions are known and it was adopted by [Ho et al., 2008], since it does not have any of the aforementioned problems. Its main drawback is that the other samples only probe the range out to $z \sim 2.6$, and little data is available to constrain $f(z)$ above that.

The redshift distribution was then fit to the cross-power spectra and $f_{\text{NVSS}}(z)$ is the Eq. (6.1) with three free parameters, b_{eff} , z_* , and α . Of these the normalization b_{eff} may be viewed as an effective bias in the sense that $\int f_{\text{NVSS}}(z) dz = b_{\text{eff}}$; in the absence of cosmic magnification this would be the bias averaged over the redshift distribution. The peak of the distribution is at z_* , and α controls the width of the distribution.

There are always some radio sources without optical identifications, however this method enables one to set an upper limit to the number of NVSS sources that can be at high redshift. [Ho et al., 2008] have matched against the COSMOS field, which has a modest solid angle (2 deg^2), multiband imaging allowing good photometric redshifts, and deep high-resolution coverage with the VLA. Area is required due to the low density of NVSS sources (40 deg^{-2}), and high-resolution radio images are required to uniquely identify an NVSS source with an optical counterpart due to the large positional uncertainty in the NVSS ($\sim 7 \text{ arcsec}$ for faint sources) [Condon et al., 1998].

The photometric redshift distribution of the matches is shown in Fig. 4.5. The best-fit $f_{\text{NVSS}}(z)$ (with the Γ distribution) has 24% of the bias-weighted source distribution at $z > 2$ and 8% at $z > 3$; if the source bias increases with redshift, as usually found for optical quasars, this number would be lower. From Fig. 4.5, only 2 out of 64 matches fall at $z > 2$, i.e. the high-redshift tail of the Γ distribution can only exist in reality if (i) most of the 26% of the sources with failed matches to COSMOS optical/NIR data are actually at $z > 2$, or (ii) the sources at $z > 2$ have a large bias.

- The second galaxy distribution we explore is the most recent galaxy redshift distribution proposed by [de Zotti et al., 2010], a fourth order polynomial fit to the CENSORS distribution [Brookes et al., 2008]:

$$\frac{dN^{dZ}}{dz} = 1.29 + 32.37z - 32.89z^2 + 11.13z^3 - 1.25z^4. \quad (4.3)$$

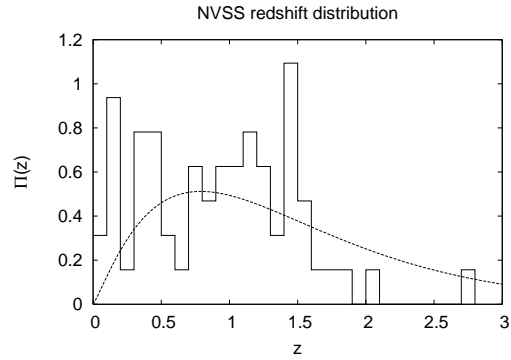


Figure 4.5: The dashed line is the fit three-parameter $f_{\text{NVSS}}(z)$, normalized to unity (i.e. the redshift distribution assuming constant bias and negligible effect from magnification).

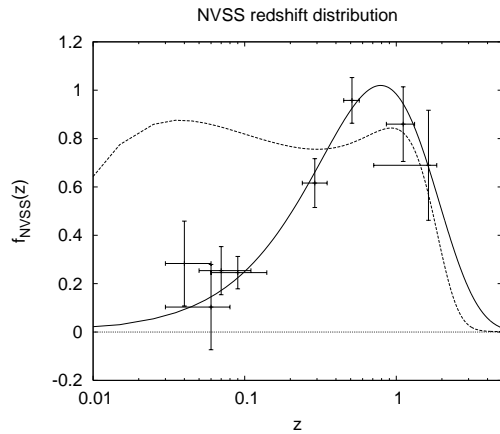


Figure 4.6: The constraints on the NVSS redshift distribution from the cross-correlations with the other eight samples. The horizontal error bars show the redshift window functions as described in the text. The dashed line shows the result of using the redshift distribution based on the [Dunlop & Peacock, 1990] luminosity function assuming constant bias and neglecting magnification, as has been done in most ISW studies.

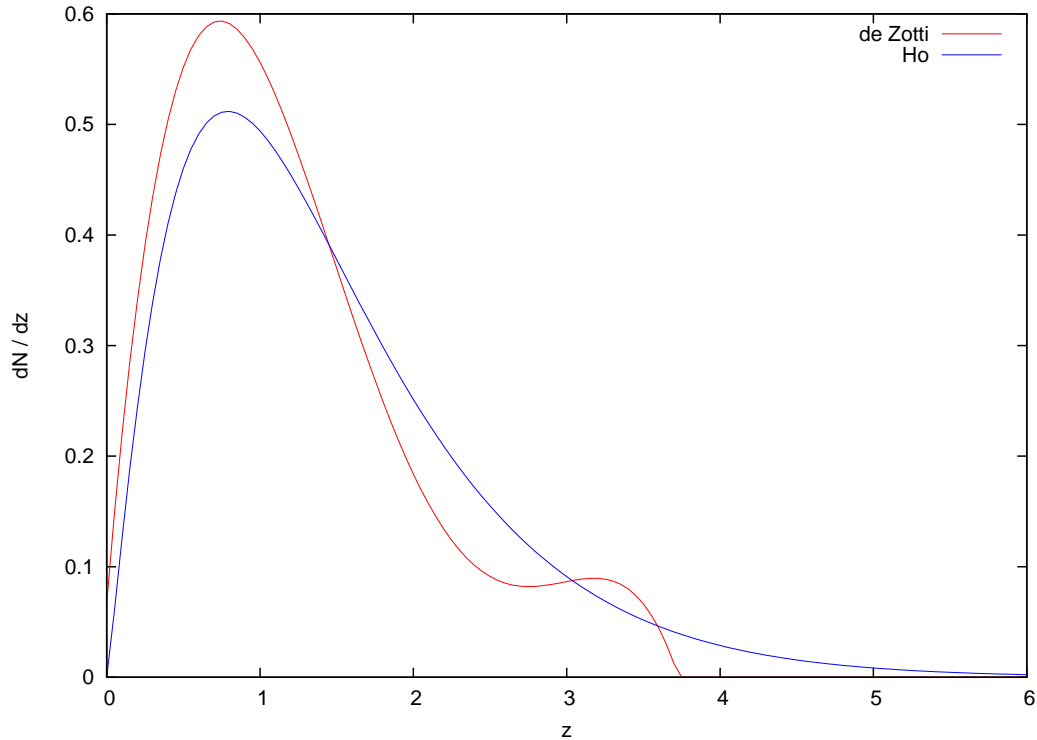


Figure 4.7: Galaxy distributions from CENSORS (red curve) and from the Γ distribution by [Ho et al., 2008] (black curve).

In this model the units are given by the number of galaxies per redshift and square degrees [de Zotti et al., 2010]. This distribution dN/dz is normalized to unity choosing the integration range between 0 and $z_{max} = 3.73$, where z_{max} is the redshift at which model vanishes (Fig. 4.7).

We know the constant bias approach is not physically correct. For this reason this galaxy distribution contains a redshift dependent bias $b(z)$. We use the bias parametrization of [Xia et al., 2010] that consider a model for the Gaussian bias given by

$$b_G(z) = b_1 + \frac{b_2}{D^\gamma(z)} \quad (0 \leq \gamma \leq 2), \quad (4.4)$$

where b_1 and b_2 being free parameters and $D(z)$ is the growth factor (Chap. 1). An “object-conserving” bias model corresponds to $\gamma \approx 1$, while the bias of high-density peaks for objects that have just formed yields $\gamma \approx 2$.

The expression of $b(z)$ requires the knowledge about the mass function, given by

[Xia et al., 2010] by the weighted effective halo bias in a non-Gaussian regime

$$b_{\text{NG}}^{\text{eff}}(M_{\text{min}}, z, k, f_{\text{NL}}) = \frac{\int_{M_{\text{min}}}^{\infty} b_{\text{NG}} n_{\text{NG}} dM}{\int_{M_{\text{min}}}^{\infty} n_{\text{NG}} dM} \quad (4.5)$$

where, in our case, only the minimum halo mass M_{min} is a free parameter. n_{NG} is the number of halos and f_{NL} the non-Gaussianity parameter. In [Xia et al., 2010] the parameters corresponds to $b_0 = 1.1$, $b_1 = 0.6$ and $\gamma = 1$. We choose to rescale these power spectra in order to be coincident with the fiducial from [Ho et al., 2008] at $\ell = 64$.

All the theoretical power spectra in temperature, galaxy or polarization are usually numerically computed with codes as COSMICS, CMBFAST and CAMB (the last two derived from COSMICS).

In this thesis the calculation of all the C_{ℓ}^{GG} and C_{ℓ}^{TG} spectra as well as the ISW part of the temperature power spectrum C_{ℓ}^{ISW} is done using a modified version of the CAMB code [Lewis et al, 2000].

4.3.3 Shot noise

A very important issue to take into account in a galaxy survey is its *shot noise*, a Poissonian uncertainty of measuring a distribution of galaxies. We define the quantity δ_i as the galaxy number density for each pixel i

$$\delta_i = \frac{n_i - \bar{n}}{\bar{n}}, \quad (4.6)$$

and the error on the galaxy number in a pixel as

$$\delta n_i = \sqrt{\bar{n}_i}. \quad (4.7)$$

Then the galaxy number density is affected by an error given by

$$\delta \delta_i = \frac{\delta n_i}{\bar{n}} = \frac{\sqrt{\bar{n}_i}}{\bar{n}}. \quad (4.8)$$

The properly variance for the shot noise is

$$\sigma_{sn}^2 = \frac{\bar{n}_i}{\bar{n}^2}. \quad (4.9)$$

In our analysis we use a uniform shot noise

$$\sigma_{sn}^2 = \frac{1}{\bar{n}}, \quad (4.10)$$

the same for each pixel. Since it depends from the ratio $\bar{n} = \frac{N_{gal}}{N_{obspix}}$, the three flux cuts of the NVSS we consider have different shot noises, in particular when we have a small number of galaxies (high flux cut) the shot noise is high.

Chapter 5

BolISW code

In order to estimate the angular power spectrum (APS) of the cross-correlation between cosmic microwave background and large scale structure maps, seen in the previous chapter, we implemented an optimal method, a Quadratic Maximum Likelihood (QML) method. The QML method for power spectrum estimate of CMB anisotropies was introduced in [Tegmark, 1997] and later was also developed for CMB polarization in [Tegmark & de Oliveira-Costa, 2001]. A different implementation of the method was applied to the cross-correlation between CMB (WMAP1) and LSS (SDSS) by [Padmanabhan et al., 2005] and by [Ho et al., 2008] between WMAP3 and many different LSS maps (2MASS, SDSS LRG, SDSS QSO and NVSS)) were used.

The code *BolISW* described in the following sections has a similar parallel architecture to the *BolPol* code implemented by [Gruppuso et al., 2009], where the QML method was used to cross-correlate the CMB temperature with the CMB polarization E and B modes (see Sec. 5.2).

5.1 QML algebra

Given a CMB map in temperature (T) and a galaxy survey in number of galaxies per pixel (G), we define a vector in pixel space $\mathbf{x} = (\mathbf{T}, \mathbf{G})$ representing in observed maps.

The QML provides an estimator of the angular power spectrum \hat{C}_ℓ^X - where X can be one of TT, TG, GG correlations. This estimator is given by

$$\hat{C}_\ell^X = \sum_{\ell'X'} (F^{-1})_{\ell\ell'}^{XX'} \left[\mathbf{x}^t \mathbf{E}_{\ell'}^{X'} \mathbf{x} - tr(\mathbf{N} \mathbf{E}_{\ell'}^{X'}) \right], \quad (5.1)$$

where the $F_{\ell\ell'}^{XX'}$ components of the Fisher matrix defined as

$$F_{\ell\ell'}^{XX'} = \frac{1}{2} \text{tr} \left[\mathbf{C}^{-1} \frac{\partial \mathbf{C}}{\partial C_{\ell}^X} \mathbf{C}^{-1} \frac{\partial \mathbf{C}}{\partial C_{\ell'}^{X'}} \right], \quad (5.2)$$

and the \mathbf{E} matrix is given by

$$\mathbf{E}_{\ell}^X = \frac{1}{2} \mathbf{C}^{-1} \frac{\partial \mathbf{C}}{\partial C_{\ell}^X} \mathbf{C}^{-1}. \quad (5.3)$$

The $\mathbf{C} = \mathbf{S}(C_{\ell}^X) + \mathbf{N}$ is the total global covariance matrix including the signal \mathbf{S} and noise \mathbf{N} contributions. The \mathbf{S} matrix components are

$$C_{ij}^X = \sum_{\ell} C_{\ell}^X P_{ij}^{\ell} \quad (5.4)$$

where P_{ij}^{ℓ} are the Legendre polynomials

$$P_{ij}^{\ell} = \frac{2\ell + 1}{4\pi} \mathbf{P}^{\ell}(\hat{r}_i, \hat{r}_j) \quad (5.5)$$

and C_{ℓ}^X is called the fiducial theoretical power spectrum (it is used to create the simulated maps useful to test the method in Sec. 5.4).

Then there are three inputs in the QML method: the \mathbf{x} vector that contains the maps and the \mathbf{N} noise matrix; the last input is the C_{ℓ}^X , given by the theoretical cosmological model. It was proven by [Gruppuso et al., 2009] and by the analysis in this thesis that these fiducial spectra are a kind of starting point and that the estimates are not dependent from them, but only from the power spectra which characterizes the real temperature and galaxy distributions, respectively, the CMB and LSS maps. In Fig. 5.1 we show the three used fiducial spectra (curves in blue). For the temperature auto-spectrum the blue line is the total CMB signal, i.e. the ISW (curve in red) effect plus all is not ISW (curve in black). The ISW contribution is higher on the largest scales and gives to the total temperature fiducial model the characteristic rising on the low multipoles.

The QML is an optimal method for two reasons.

- It provides *unbiased* estimates of the power spectrum of the map regardless of this initial guess

$$\langle \hat{C}_{\ell}^X \rangle = C_{\ell}^X. \quad (5.6)$$

Here the average is taken over the ensemble of realizations based on the input spectrum C_{ℓ}^X (see Sec. 5.4). The assumed fiducial power spectra can impact the error estimates through the Fisher matrix.

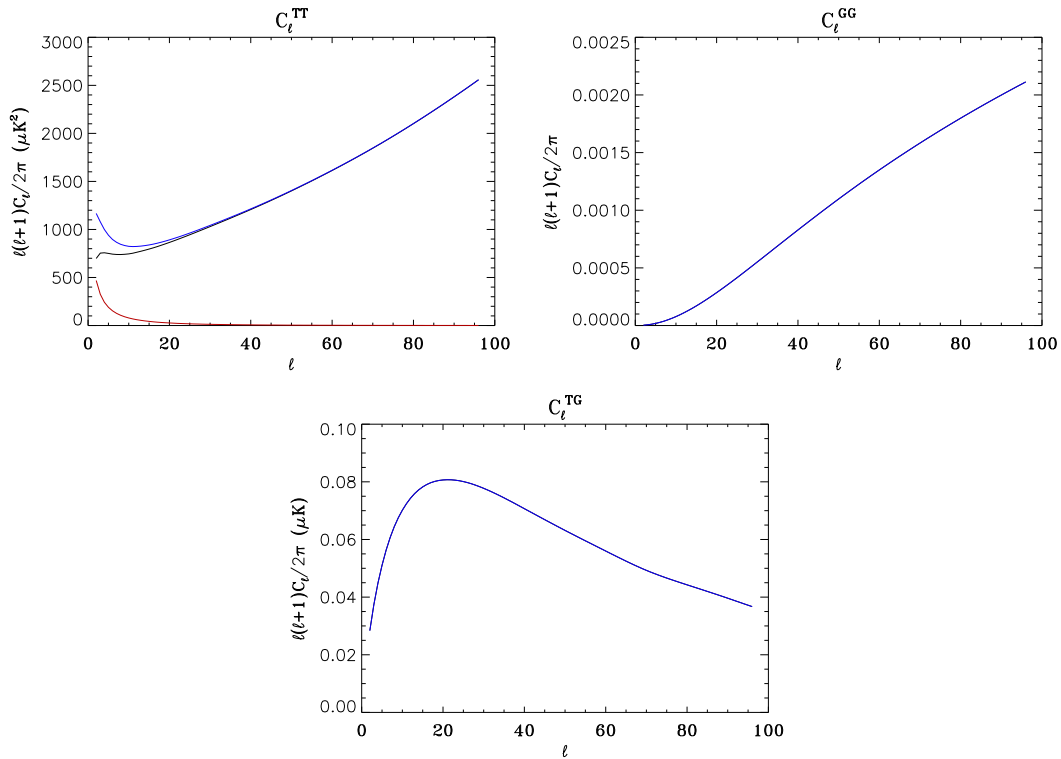


Figure 5.1: The three panels show the theoretical fiducial models for the three spectra TT, TG and GG. In the first panel there are three curves: the black is the power spectrum for which is not ISW; the red curve is the only ISW power spectrum; the blue curve is the power spectrum for the total CMB signal. For all the power spectra in our analysis we choose to plot the temperature in μK and the galaxy number density adimensionless.

- The QML method has *minimum variance*, i.e. it can provide the smallest error bars allowed by the Fisher-Cramer-Rao inequality,

$$\langle \Delta \hat{C}_\ell^X \Delta \hat{C}_{\ell'}^{X'} \rangle = (F^{-1})_{\ell\ell'}^{X X'}, \quad (5.7)$$

where

$$\Delta \hat{C}_{\ell'}^{X'} = \hat{C}_\ell^X - \langle \hat{C}_\ell^X \rangle, \quad (5.8)$$

and the averages, as above, are over an ensemble of realizations. In Sec. 5.4 we will demonstrate the unbiased and minimum variance properties, which therefore constitute the validation of the code.

5.2 BolPol

The original code *BolPol* is a fully parallel implementation (MPI) of the QML method written in F90. Since the method works in pixel space the computational

cost increases as one considers smaller angular resolution for a given sky area, i.e. more pixels. This is the reason why the QML code has been parallelized. The inversion of the covariance matrix \mathbf{C} scales as $\mathcal{O}(N_{pix}^3)$. The number of operations is roughly driven, once the inversion of the total covariance matrix is done, by the matrix-matrix multiplications to build the operators \mathbf{E}_ℓ^X in Eq. (5.3) and by calculating the Fisher matrix $F_{XX'}^{\ell\ell'}$ given in Eq. (5.2). The number of operations that are needed to build these matrices scales as $\mathcal{O}(N_{side}^2 N_{pix}^2)$ and $\mathcal{O}(N_{side} N_{pix}^3)$ respectively. The RAM required is of the order $\mathcal{O}(\Delta\ell N_{pix}^2)$ where $\Delta\ell$ is the number of $\mathbf{C}^{-1}(\partial\mathbf{C}/\partial C_\ell^X)$ (for every X) that are built and kept in memory during the execution time.

Given these kind of scalings, it is clear that it is currently unrealistic to run the QML estimator for all-sky maps of resolution larger than $N_{side} = 8$ (in Healpix language¹ [Gorski et al., 2005]) on a single CPU. To reach higher resolution we use the ScaLapack library² and the BLACS³ routines which are optimized for distributed memory parallel computers. In this way it is possible to run *BolPol* on the WMAP data set with the resolution of $N_{side} = 16$ on a supercomputer. Note that $N_{side} = 16$ is not the highest resolution that *BolPol* is able to consider. Currently *BolPol* is able to process maps of $N_{side} = 32$.

BolPol was applied to the WMAP5 ([Gruppuso et al., 2009]) and WMAP7 ([Gruppuso et al., 2011]) low resolution maps to compute the CMB angular power spectra at large scales for both temperature and polarization.

The six angular power spectrum (TT,TE,TB,EE,EB,BB) estimates have been provided up to $\ell_{MAX} = 48$, taking into account the computational cost due to the considered high number of pixels. In Fig. 5.2 we show the comparison of the estimates obtained with WMAP7 and WMAP5 data for all the six power spectra.

5.3 *BolISW*

The *BolISW* code, implemented in this thesis, stems from *BolPol* and computes three angular power spectra (TT,TG,GG), then it is capable to use higher resolutions with respect to *BolPol*. Currently the code is working with $N_{side} = 32$ and computes - all

¹<http://healpix.jpl.nasa.gov/>. For people not familiar with the Healpix notation, N_{side} is related to the number of pixels N_{pix} by $N_{pix} = 12N_{side}^2$.

²<http://www.netlib.org/scalapack/>

³<http://www.netlib.org/blacs/>

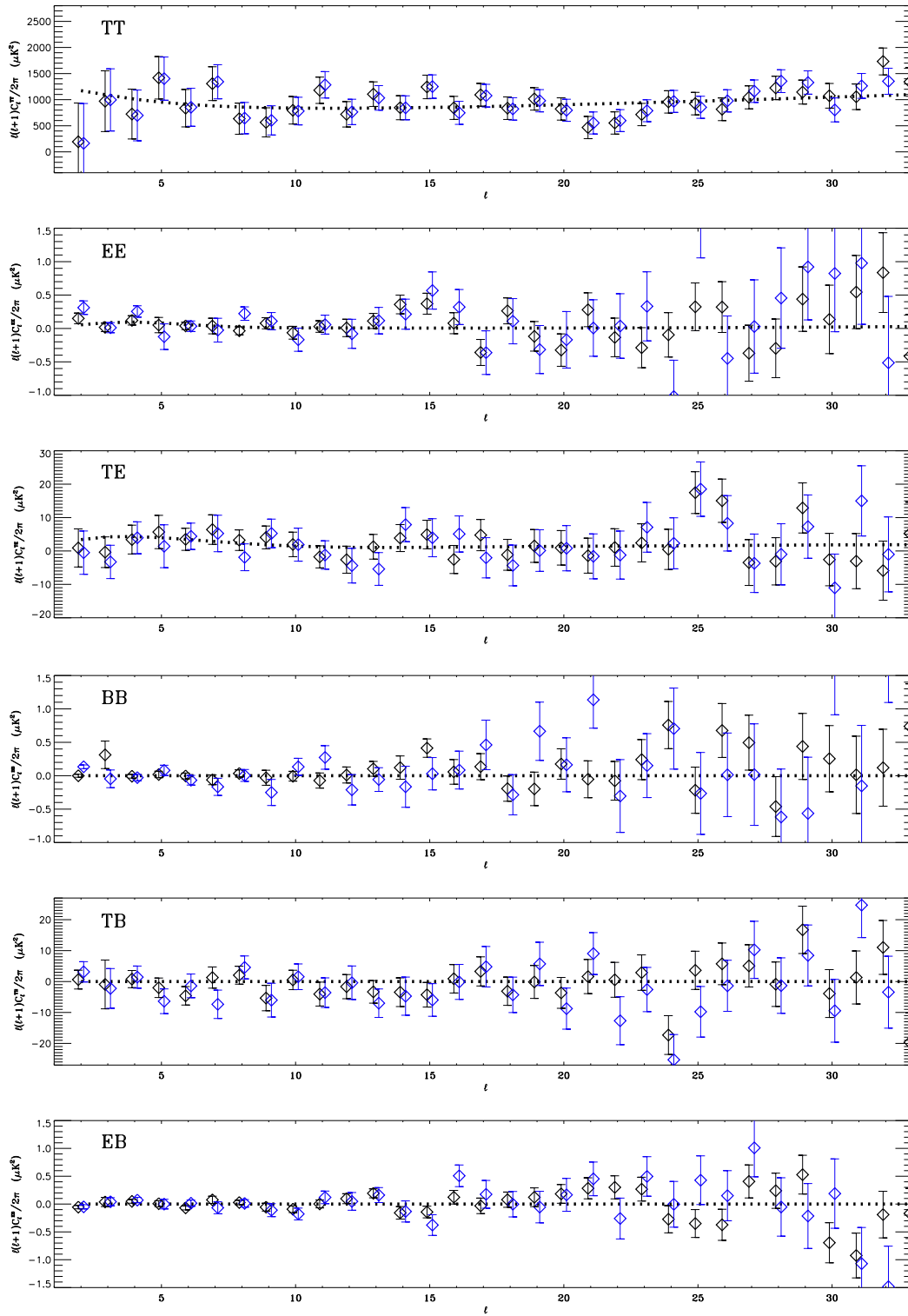


Figure 5.2: The panels show the six power spectra obtained by *BolPol* with two data sets: WMAP5, blue points; WMAP7, black points. In the plots $\ell_{MAX} = 32$. The black dotted line is the correspondent fiducial model.

Table 5.1: Numerical features

Code	<i>BolPol</i>	<i>BolISW</i>	<i>BolISW</i>
Features	$N_{side} = 16$	$N_{side} = 32$	$N_{side} = 64$
$\ell_{MAX} = 3 \text{ (or } 2) \times N_{side}$	48	96	128
$N_{pixel} = 12 \times N_{side}^2$	9 216	24 576	98 304
$N_{processor}$	64	256	512
Computing time (min)	~ 20	~ 40	~ 570 (9.5 hours)
Hardisk (GB)	65	153	671

together - the three spectra; however a code version has been implemented in order to use $N_{side} = 64$, then in this case it is necessary to compute only one spectrum at a time because of the large increasing in the number of pixel.

My code runs on the SP6 supercomputer at CINECA (processor type: Opteron Dual Core 2.6 GHz, with 4 GB per processor), in Tab. 5.1 we summarize some technical features for *BolPol* with $N_{side} = 16$ and *BolISW* with both resolutions $N_{side} = 32, 64$.

5.3.1 Numerical optimization

For the reasons discussed above, the QML method is computationally expensive at high resolution. we discuss here some changes which can improve the numerics and decrease substantially the execution time with a negligible loss of accuracy.

The predicted C_ℓ^{TG} is generally non-zero, and its measurement is the primary goal of our analysis. In the following analysis, we decide to assume $C_\ell^{TG} = 0$ for the fiducial model which is used to build the covariance matrix. This working hypothesis is a good approximation as it is proven in the validation of the code (see Sec. 5.4). Furthermore, the noise matrix \mathbf{N} may be assumed to be uncorrelated between the CMB and the galaxy measurements and then block-diagonal. Under these assumptions, the Fisher matrix becomes block diagonal and the three spectra $\hat{C}_\ell^{TT}, \hat{C}_\ell^{TG}, \hat{C}_\ell^{GG}$ can be estimated independently from each other. This reduces the computation cost of the Fisher matrix by $\sim 50\%$ with respect to the problem with the full covariance. Moreover estimating just \hat{C}_ℓ^{TG} the computational cost of the problem decreases by a further factor of 1/3, as in [Padmanabhan et al., 2005]; we use this reduction when we compute the estimates with a resolution of $N_{side} = 64$.

In order to apply the algebra of the QML method, described in Eq.s (5.1-5.3), one must build the covariance matrix \mathbf{C} in pixel space and the Fisher matrix \mathbf{F} in ℓ space. The latter is the most expensive task at computational level, largely because

it requires the inversion of the pixel space covariance matrix \mathbf{C} . This inversion can also introduce numerical errors since its eigenvalues span several orders of magnitude (which it is visible also among the Fisher matrix blocks, for more details see A 7.2)

To bypass this issue, we have used inversion-routines only on numerically homogeneous blocks thanks to the following expressions. Given a general matrix A in block form,

$$A = \begin{pmatrix} A_{11} & A_{12} \\ A_{21} & A_{22} \end{pmatrix}, \quad (5.9)$$

where A_{11} and A_{22} are non-singular square matrices, then it can be shown that the inverse of A is

$$A^{-1} = \begin{pmatrix} B_{11} & -B_{11}A_{12}A_{22}^{-1} \\ -A_{22}^{-1}A_{21}B_{11} & A_{22}^{-1} + A_{22}^{-1}A_{21}B_{11}A_{12}A_{22}^{-1} \end{pmatrix}, \quad (5.10)$$

with

$$B_{11} = (A_{11} - A_{12}A_{22}^{-1}A_{21})^{-1}. \quad (5.11)$$

For this case, the covariance matrix \mathbf{C} is divided in sub-blocks (TT, TG and GG blocks), so that A_{11} is the covariance related to the CMB temperature sector and A_{22} relates to the covariance of the galaxy sector. Thus, assuming a fiducial model without any cross-covariance simplifies the inversion calculation significantly. This technique is also applied to the Fisher matrix inversion in multipole space (with $A_{11} = F_{\ell\ell'}^{TT}$), obtaining a much better precision with respect to the brute force inversion (~ 3 orders of magnitude)

Note that when the fiducial power spectrum for the cross-correlation C_{ℓ}^{TG} is chosen to be null, then the two aforementioned matrices (both \mathbf{C} and \mathbf{F}) become block-diagonal and their inversion is simply given by the inversion of each of the diagonal blocks. In this particular case of \mathbf{F} , the QML method splits into three independent “smaller” QMLs, for TT , GG and TG ([Ho et al., 2008]).

As we will show in next section with the Monte Carlo validation and later in Chap. 7 where we will apply QML to real data, using the $C_{\ell}^{TG} = 0$ approximation does not change the estimates, but the little fluctuations in the error bars amplitude, between the cases $C_{\ell}^{TG} = 0$ and $C_{\ell}^{TG} \neq 0$, will be visible since amplified in the likelihood analysis.

5.4 Validation

In order to validate the implementation of the QML method, we create simulated CMB temperature anisotropy and galaxy count maps following the recipe described in [Boughn & Crittenden, 1998] (see also [Barreiro et al., 2008] and [Giannantonio et al., 2008]). we employ the HEALPix program *synfast* [Gorski et al., 2005], which allows one to create $a_{\ell m}$ such that

$$\langle a_{\ell m}^Y a_{\ell' m'}^{Y' *} \rangle = C_\ell^{YY'} \delta_{\ell\ell'} \delta_{mm'}, \quad (5.12)$$

where $Y, Y' = T, G$. The total map for the CMB anisotropies $a_{\ell m}^T$ is simulated as the sum of three different maps

$$a_{\ell m}^T = a_{\ell m}^{\text{ISWc}} + a_{\ell m}^{\text{ISWu}} + a_{\ell m}^{\text{prim}}, \quad (5.13)$$

where $a_{\ell m}^{\text{ISWc}}$ represents the fully correlated ISW effect with the galaxy distribution, $a_{\ell m}^{\text{ISWu}}$ is the uncorrelated part of the ISW effect and $a_{\ell m}^{\text{prim}}$ is the primordial CMB signal. These amplitudes are given by

$$a_{\ell m}^{\text{ISWc}} = \xi_a \frac{C_\ell^{\text{TG}}}{\sqrt{C_\ell^{\text{GG}}}}, \quad (5.14)$$

$$a_{\ell m}^{\text{ISWu}} = \xi_b \sqrt{C_\ell^{\text{ISW}} - \frac{(C_\ell^{\text{TG}})^2}{C_\ell^{\text{GG}}}}, \quad (5.15)$$

$$a_{\ell m}^{\text{prim}} = \xi_c \sqrt{C_\ell^{\text{TT}} - C_\ell^{\text{ISW}}}. \quad (5.16)$$

In addition for the galaxy count maps we consider

$$a_{\ell m}^G = \xi_a \sqrt{C_\ell^{\text{GG}}}, \quad (5.17)$$

where ξ 's are Gaussianly distributed complex random numbers, with zero mean and unit variance. They are the seeds of the simulations and satisfy $\langle \xi_a \xi_{a'}^* \rangle = \delta_{aa'}$. In this way it can be proven that

$$\langle a_{\ell m}^T a_{\ell m}^{T*} \rangle = C_\ell^{\text{TT}}, \quad (5.18)$$

$$\langle a_{\ell m}^G a_{\ell m}^{G*} \rangle = C_\ell^{\text{GG}}. \quad (5.19)$$

$$\langle a_{\ell m}^T a_{\ell m}^{G*} \rangle = C_\ell^{\text{TG}}. \quad (5.20)$$

where $C_\ell^{\text{TT}}, C_\ell^{\text{TG}}$ and C_ℓ^{GG} are the fiducials introduced in the previous section.

We have tested the *BolISW* code using these Monte Carlo simulations. In particular, we have performed 1000 realizations for CMB and LSS correlated maps at the HEALPix resolution of $N_{\text{side}} = 32$. For the multipoles, we consider the range $\Delta\ell = [2, 95]$, i.e., up to the Nyquist frequency $3N_{\text{side}} - 1$. By using the particular fiducial power spectra forementioned above, the standard Λ CDM cosmological model [Larson et al., 2011] is assumed, as well a survey characteristics similar to the NVSS catalogue [Condon et al., 1998], namely: a similar sky coverage and a galaxy density number distribution per redshift given by the [Ho et al., 2008] model, and a bias $b = 1.98$ (see previous chapter)

These simulated maps show that *BolISW* leads to unbiased and minimum variance results, as can be seen by comparing the simulations to the projected errors from the Fisher matrix, in Fig. 5.3 with the two auto-spectra and in Fig. 5.4 with the cross-spectrum. In this plot it is shown the Monte Carlo estimates with two different error bars, from the Fisher matrix (1) and from the Monte Carlo variance (2). The *unbiased* issue is proven because the estimates fall exactly on the fiducial model it is used to characterize the simulated maps for all the three spectra. Also the *minimum variance* is proven almost for all the multipoles; in the three spectra a small discrepancy between the error bars computed from (1) and from (2), in particular for multipoles higher than $\ell \sim 64$. We have checked this discrepancy was not due to the $C_\ell^{TG} = 0$ approximation, computing the Monte Carlo for the case with fiducial model different from zero. The two cases result equivalent. Importantly, we confirm that the method is unbiased and has minimum variance when the fiducial cross power spectrum C_ℓ^{TG} is set to zero, i.e. when the code is less computationally expensive.

Further, we have also verified by Monte Carlo that our implementation is optimal when considering the realistic case of a masked sky (thin error bars in Figs 5.5 and 5.6).

It is important to notice that, while on these large-scales the noise contribution in WMAP and future (PLANCK) CMB temperature maps is so low that the CMB noise \mathbf{N} might be safely neglected, this is not true for large scale structure surveys. Depending on the number of sources used as large scale tracers, the galaxy density map could be significantly affected by a Poissonian shot noise, which must be taken into account.

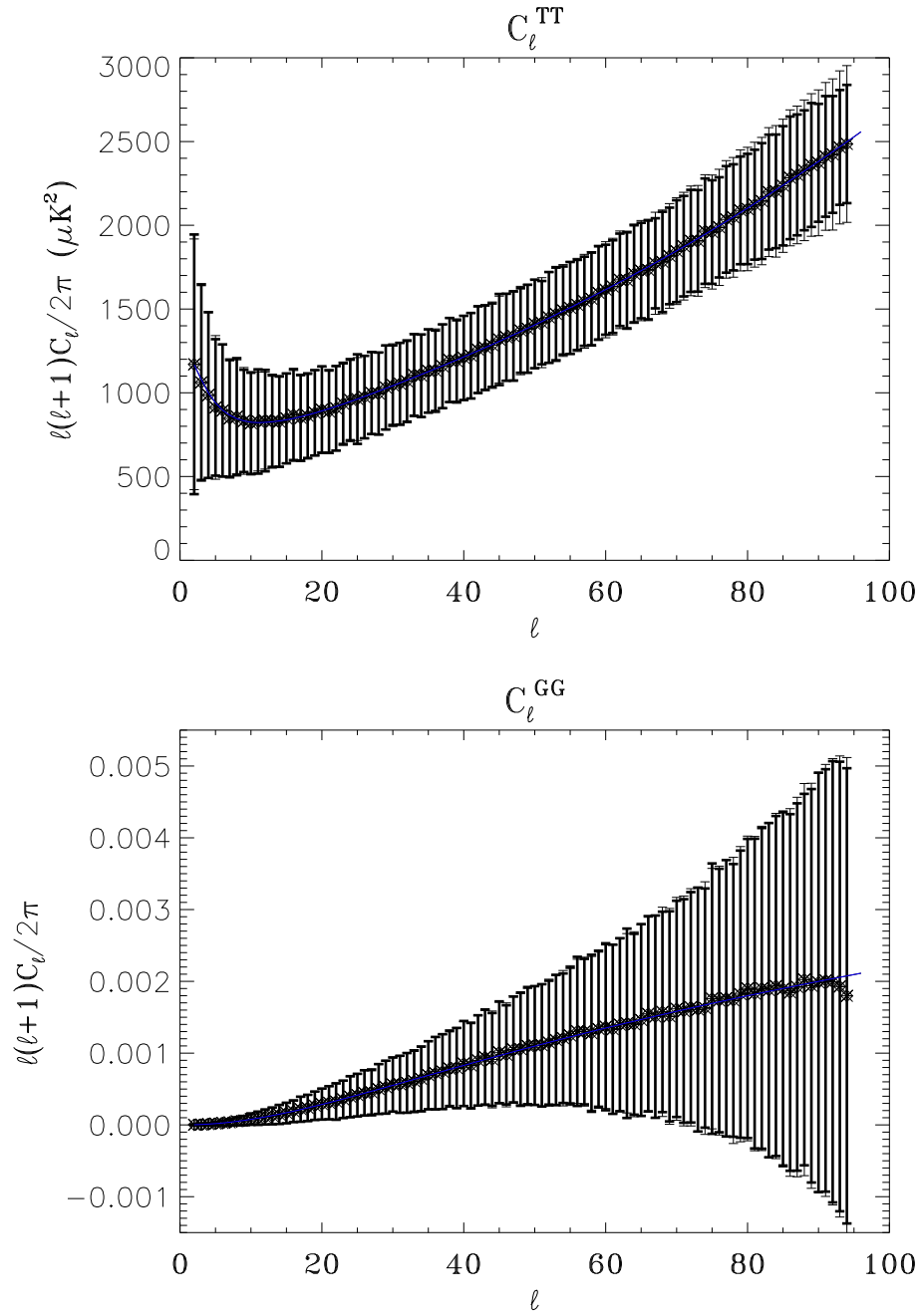


Figure 5.3: The two panels show two error bars of the average estimates for the Monte Carlo validation obtained in two different ways: the thin error bars are given by the inverse of the Fisher matrix; the thick error bars are given by the Monte Carlo variance. The upper and lower panels show the TT and GG auto spectra, respectively. The two error bars are coincident until $\ell \sim 64$, then the error bars obtained by the Fisher matrix become larger.

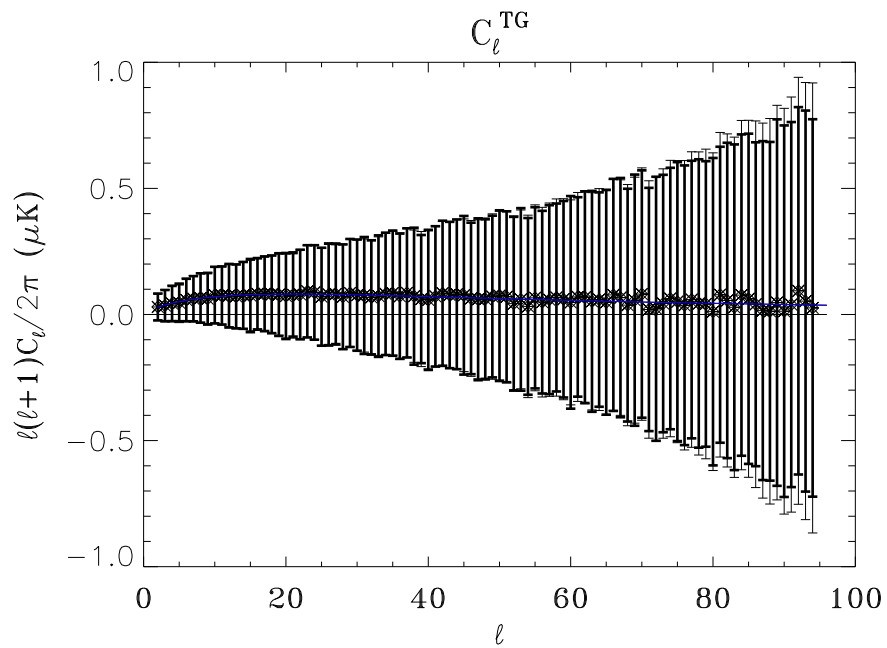


Figure 5.4: The panel shows, in TG cross spectrum, two error bars of the average estimates for the Monte Carlo validation obtained in two different ways: the thin error bars are given by the inverse of the Fisher matrix; the thick error bars are given by the Monte Carlo variance. The two error bars are coincident until $l \sim 64$, then the error bars obtained by the Fisher matrix become larger.

The results from the Monte Carlo validation are summarized in Fig. 5.5 and Fig. 5.6: all the panels consider three different scenarios, all of which provide unbiased averaged estimates in good agreement with the fiducial model (blue lines) as seen above, and they differ only in their error bars. The first case corresponds to a masked sky (accounting for the NVSS sky coverage and the WMAP KQ75 mask) with negligible Poissonian shot noise contribution to the LSS map (given by the thick error bars); second, a full-sky case with a shot-noise like the that expected in NVSS (see the previous chapter) when only sources above 2.5mJy are taken into account (solid line error bars); and finally, a more realistic situation where both, the incomplete sky and the shot noise are included in the analysis (light dark error bars). The error bars increase when the noise level in the LSS map rises and when the fraction of the sky considered is reduced, the latter falling approximatively with the $\sqrt{f_{\text{sky}}^T f_{\text{sky}}^G}$, as expected.

For comparison, the plots also include (dark lines) the average *anafast* estimation for the full-sky case (dark lines), based on the simple HEALPix FFT tool; the *anafast* estimation is slightly biased at high ℓ in the two auto-spectra.

As final validation test the QML code was runned on one simulated map, with masks applied and removing the same shot noise used before. The results are summarized in Fig.s 5.7 and 5.8. In the bottom panel of Fig. 5.8 we binned the \hat{C}_ℓ^{TG} estimates, over $\Delta\ell = 9$.

Since the signal-to-noise for unbinned TG power spectrum is rather poor, we present also the binned power spectrum C_b^{TG} over $\Delta\ell = 9$. The binned estimates are simply the average of the unbinned estimates inside the bin. For plotting purposes, we associate for the uncertainty in the binnes estimate

$$\sum_{\ell \in \Delta\ell} \frac{(F^{-1})_{\ell\ell}^{TGTG}}{N} \quad (5.21)$$

where N is the number of ℓ 's in a bin.

The same binning it is used to bin the estimates from real data in the next chapter. It is important to note how the full sky power spectrum C_ℓ^{TG} is well recover by our QML with the mask applied, of course in agreement with our Monte Carlo validation.

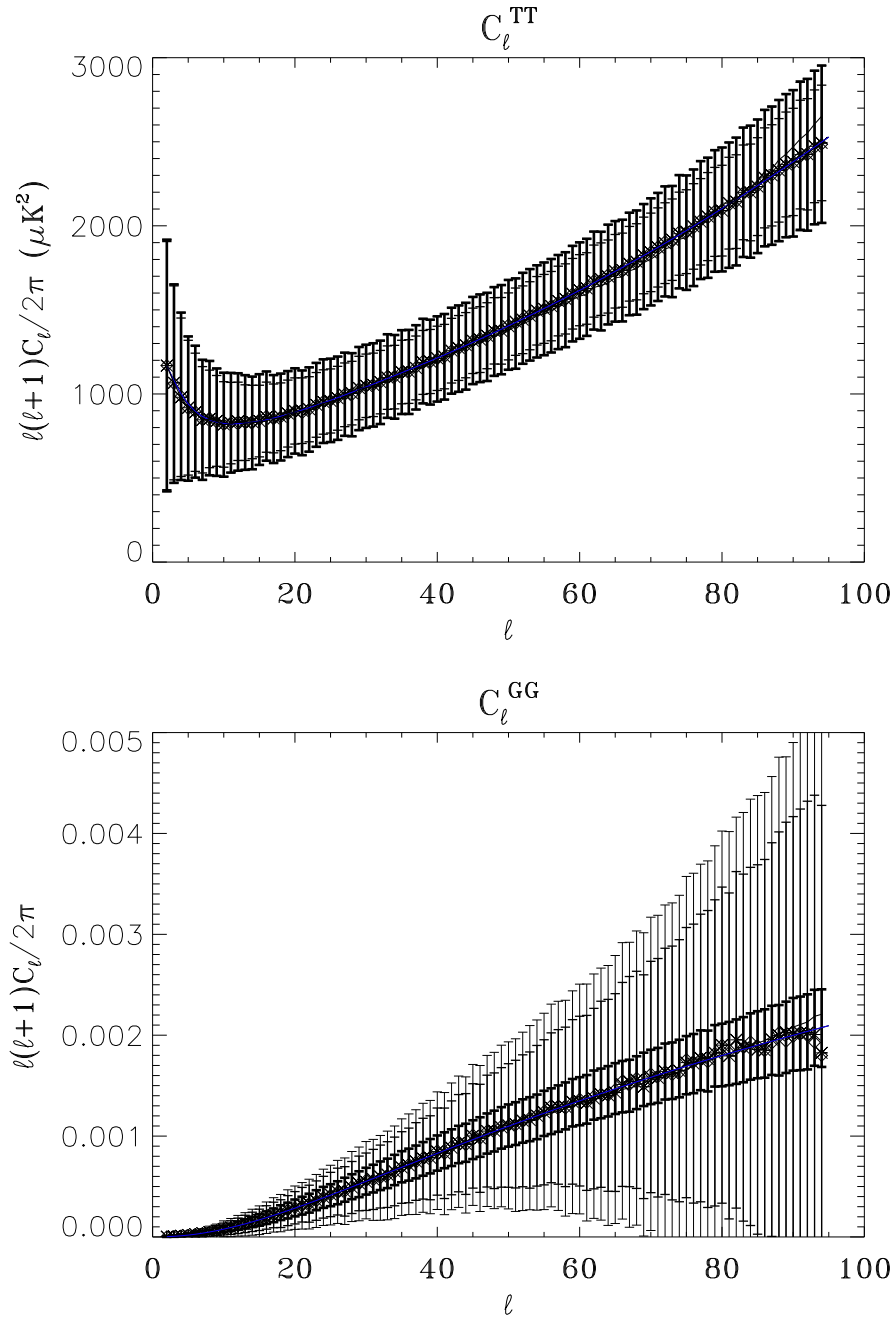


Figure 5.5: The average estimates for the Monte Carlo validation: the upper and lower panels show the TT and GG auto-spectra, respectively. We compare results for three cases: using realistically masked maps without noise in the LSS maps (thick error bars), using full sky maps with NVSS-like shot noise (solid line error bars), and assuming both masked maps and NVSS-like shot noise (light dark error bars). We can see that average power spectra from the QML all agree very well with the underlying fiducial theoretical power spectra (blue lines). The error bars change according to the noise level in the LSS map and the fraction of the sky considered. The dark lines are the average of the *anafast* estimates, which are slightly biased at high ℓ in the two auto-spectra.

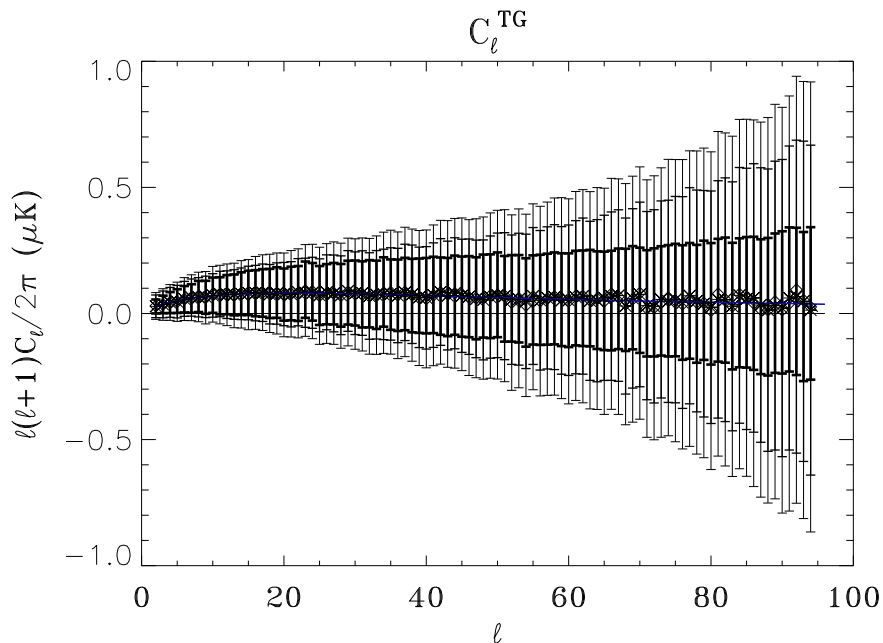


Figure 5.6: The average estimates for the Monte Carlo validation: the TG cross-spectrum. As above we compare results for three cases: using realistically masked maps without noise in the LSS maps (thick error bars), using full sky maps with NVSS-like shot noise (solid line error bars), and assuming both masked maps and NVSS-like shot noise (light dark error bars). We can see that average power spectra from the QML all agree very well with the underlying fiducial theoretical power spectra (blue lines). The error bars change according to the noise level in the LSS map and the fraction of the sky considered. The dark line is the average of the *anafast* estimates, which is not biased at high l like in the two previous auto-spectra.

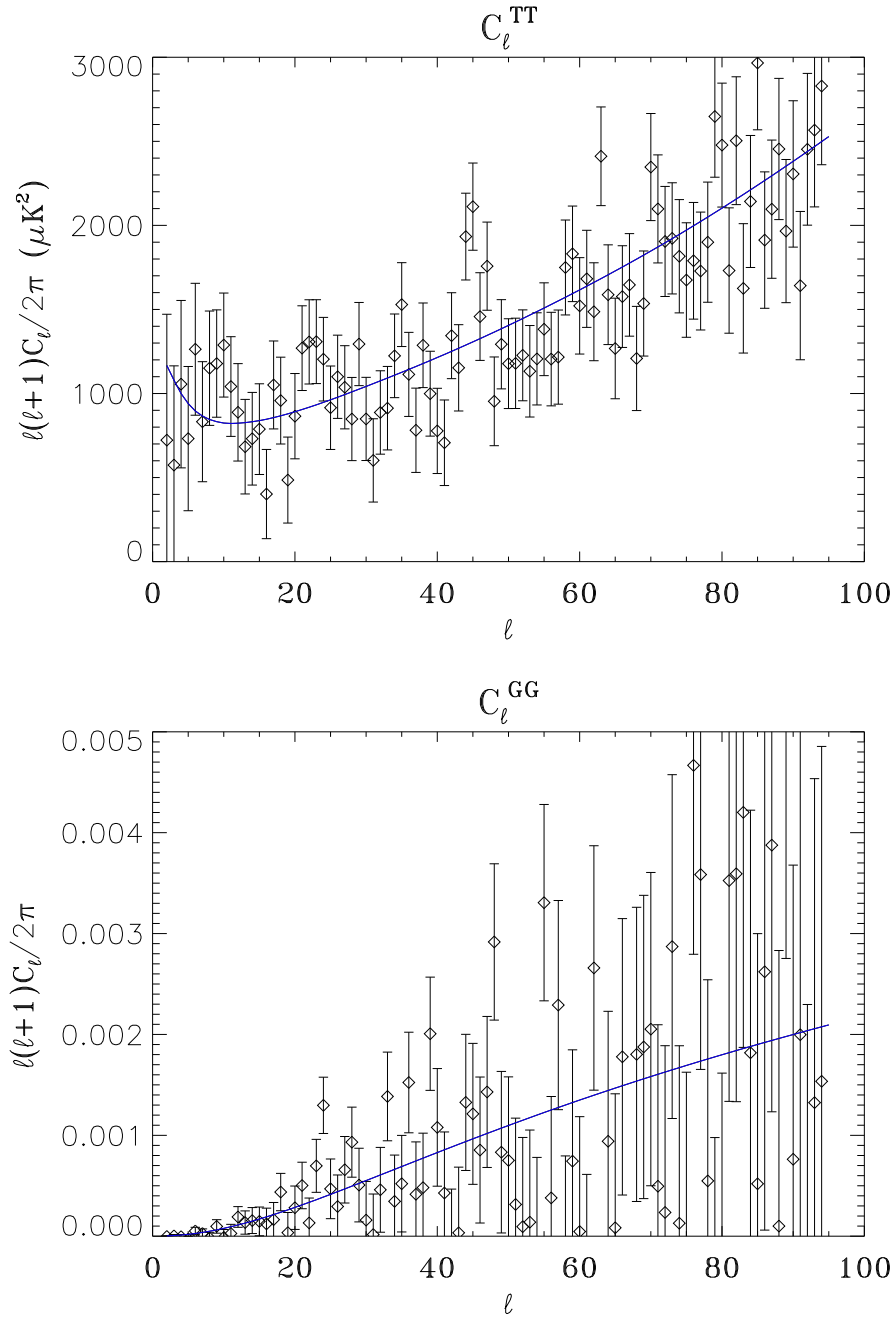


Figure 5.7: The estimates for a single full sky realization: the upper and lower panels show the auto-spectra, TT and GG. The error bars on our estimated points (stars) are estimated by the Fisher matrix. The dark broken lines are the estimates by *anafast* and the blue solid lines are the fiducial power spectra.

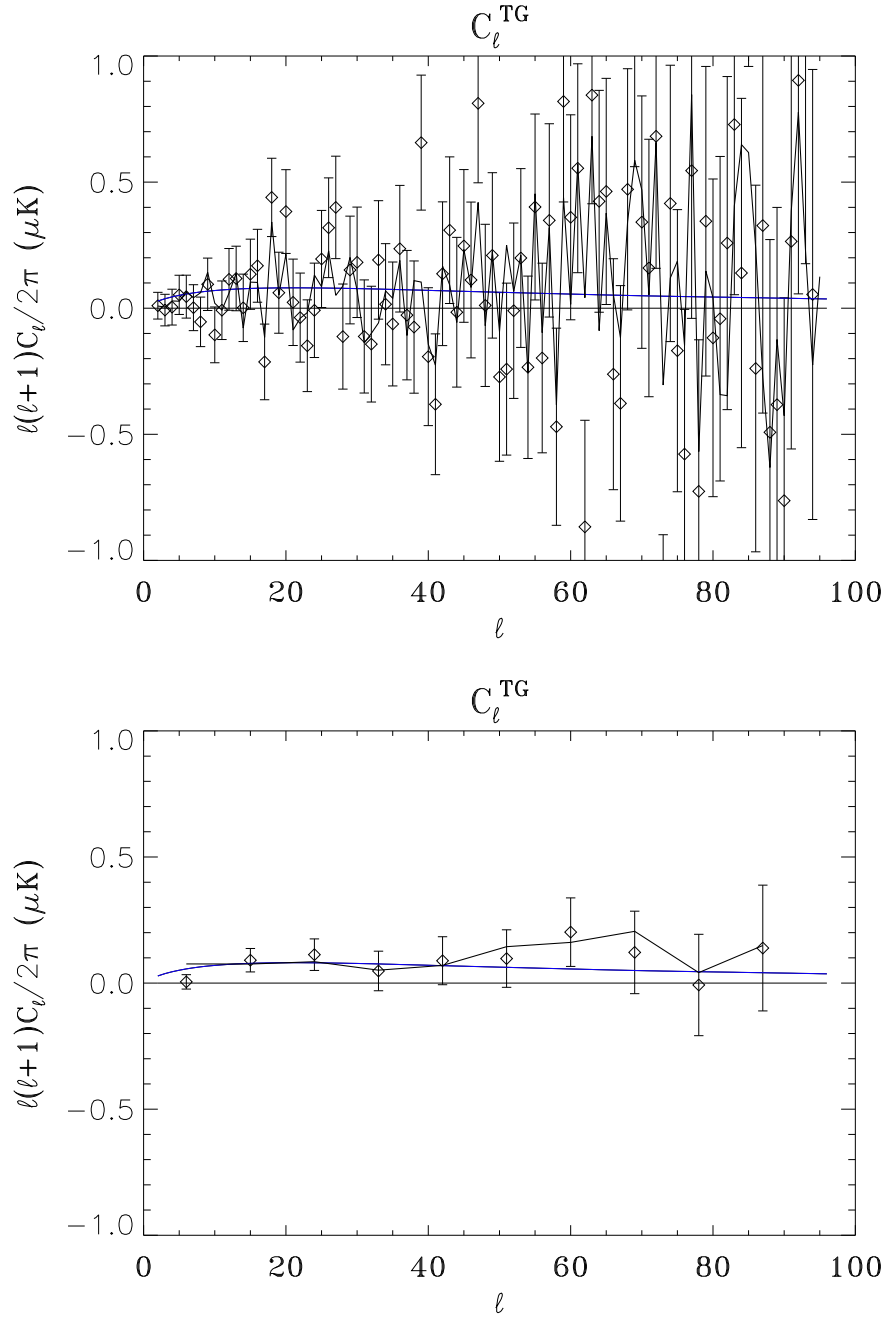


Figure 5.8: The estimates for a single full sky realization: the upper and lower panels show the cross-spectrum, TG, in the unbinned and binned cases. The error bars on our estimated points (stars) are estimated by the Fisher matrix. The dark broken lines are the estimates by *anafast* in the fully sky case and the blue solid lines are the fiducial power spectra.

Chapter 6

Application to WMAP 7 year and NVSS data

In this chapter we describe the application of *BolISW* to estimating the cross-correlation spectrum between the WMAP 7-year CMB maps and the NRAO VLA Sky Survey (NVSS) data, both described in 4. We consider three different flux cuts (2.5, 5, 10 mJy) for NVSS map and two different galaxy distributions to describe the NVSS power spectrum (the fiducial model from [Ho et al., 2008] and from [de Zotti et al., 2010]), in order to investigate potential systematic problems. We present all spectra up to $\ell = 64$ ($= 2 \times N_{side}$), in order to cut the aliasing effect on the largest ℓ 's.

6.1 TT auto-spectrum

The temperature auto power spectrum is the same for all the analysis, because we use always the WMAP 7-year map for CMB temperature and a possible noise on the TT is negligible (as seen in 4.3.3) and therefore we do not consider it here. The map is masked with the same mask used in the code validation. In Fig. 6.1, it is shown the angular power spectrum for the CMB temperature, compared to the fiducial power spectrum which is the WMAP7 year best fit ([Larson et al., 2011]).

6.2 Galaxy distribution model with constant b

In this section we present the TG cross-spectrum and the GG auto-spectrum obtained by the [Ho et al., 2008] fiducial model

$$\frac{dN^{\text{Ho}}}{dz} = \frac{\alpha^\alpha}{z_*^{\alpha+1}\Gamma(\alpha)} z^\alpha e^{-\alpha z/z_*}, \quad (6.1)$$

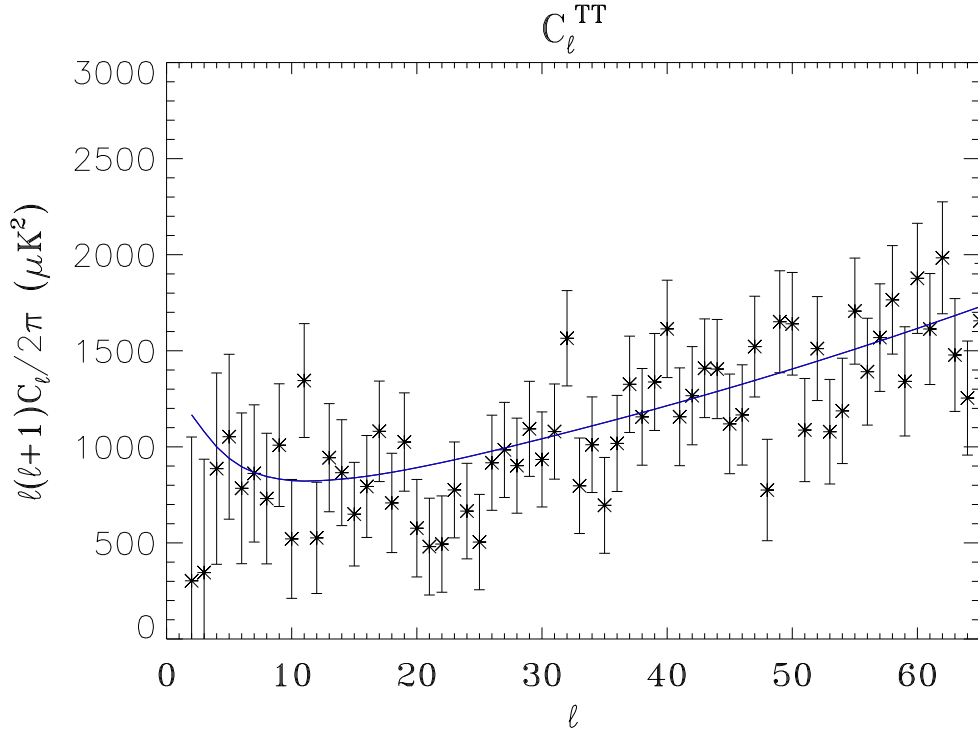


Figure 6.1: Unbinned C_ℓ^{TT} auto spectrum to $l = 64$. The estimates follow the theoretical fiducial model.

with $z_* = 0.79$, $\alpha = 1.18$ and a redshift independent value for the bias as $b = 1.98$ (see Chap. 4).

6.2.1 No shot-noise removal

In some of the literature it is not clear if the shot noise contribution is taken into account and we therefore try to estimate power spectra without removing the shot noise. Follow the unbinned estimates for the 2.5, 5.0 and 10.0 mJy flux cuts of NVSS maps, in Figs 6.2, 6.3 and 6.4.

It is useful comparing the binned estimates in all the three flux cuts, for \hat{C}_ℓ^{TG} and \hat{C}_ℓ^{GG} (Fig. 6.5).

From \hat{C}_ℓ^{GG} , it is clear a large discrepancy between the QML estimates and the fiducial model ([Pietrobon, Balbi and Marinucci, 2006]), in particular the estimates are much higher than the model. Note that the errors are small for the scale of the plot, but are given by the usual Fisher contribution with $N_{GG} = 0$. Considering only the \hat{C}_ℓ^{TG} , this high discrepancy between estimates and fiducial model is not visible.

In order to be sure about the cross-correlation, it is important to supervise also the TT and GG auto-correlations.

The discrepancy in \hat{C}_ℓ^{GG} (not only the distance between the estimates and the model but also the inconsistency among all the three flux cuts) could be due to a wrong fiducial model, to no shot noise removal or some other systematic effect not taken into account. As seen in Chap. 4, the galaxy surveys contain a Poissonian shot noise due to the variance of the observed number of galaxies per pixel; this noise is different for each flux cut and could be the reason of the discrepancy between the three flux cuts. In principle the QML can remove a noise through the noise bias term seen in Eq. (5.1), which can be fully modelled within the noise matrix \mathbf{N}_{GG} . In the first estimate computations the noise is not considered, so the \mathbf{N} matrix is zero. In order to evaluate the impact of the shot noise, a diagonal noise matrix in the GG sector (as done in Eq. 4.3.3, we choose a uniform shot noise) has been taken into account. For the TT sector we still consider a negligible noise.

6.2.2 Shot-noise removal

Here we show how the \hat{C}_ℓ^{GG} and \hat{C}_ℓ^{TG} change removing the shot-noise, as it should be clear in Figs 6.6, 6.7 and 6.8.

Comparing the binned estimates in all the three flux cuts, for \hat{C}_ℓ^{TG} and \hat{C}_ℓ^{GG} in the case of shot-noise removal, we obtain Fig. 6.9.

Removing the shot-noise, different for each flux cut because of the different galaxy number for each flux cut (in Eq. (4.10)) we get the three flux cuts converge to each other and approach towards the fiducial model, either in GG and in TG. A small difference between the theoretical power spectrum C_ℓ^{GG} and the QML estimates \hat{C}_ℓ^{GG} is still visible and we cannot find explanation to that. Our estimates for the NVSS auto-power spectrum agree very well with [Blake, Ferreira & Borril, 2004], who used an optimal estimator similar to ours on a NVSS map of the same resolution of the one used here. The stability of the C_ℓ^{GG} estimates with respect to different flux threshold found in [Blake, Ferreira & Borril, 2004] is also very similar to what we find. [Xia, Viel & Baccigalupi, 2010] estimated a larger discrepancy at lower multipoles and explained this effect as result of non-negligible primordial non-Gaussianity, caused by the large-scale scale-dependence of the non-Gaussian halo bias. However, the value inferred for the coupling non-Gaussian parameter f_{NL}

is much larger than the limits imposed by CMB analyses ([Komatsu et al., 2011, Curto et al., 2011]). However, the f_{NL} constraints derived from the CMB-LSS cross-correlation [Xia et al., 2010] provide lower values, in better agreement with the CMB tests. In addition, these authors also showed that when other LSS data sets are used [Richards, 2009, in particular, the QSOs sample of the SDSS], such non-Gaussian deviation is not found.

At first approximation a constant bias b for the galaxy distribution (same as [Ho et al., 2008]) is assumed; we know it is necessary to take into account a redshift dependent bias $b(z)$.

In the next section we show the analysis with the fiducial model based on the [Brookes et al., 2008] CENSORS galaxy distribution with a $b(z)$ given by [Xia et al., 2010] (see Chap. 4).

In Fig. 6.10, we select the 2.5mJy flux cut to show the large difference with respect to the previous case (no shot-noise removal).

The \hat{C}_ℓ^{TG} estimates show the main differences in the error bar amplitudes. Larger error bars are expected when a shot-noise is removed. The covariance matrix \mathbf{C} in this case is properly made up of the signal matrix $\mathbf{S}(C_\ell)$ and the noise matrix \mathbf{N} , as seen in the Chap. 5. According to the QML algebra the inverse Fisher matrix, from which the error bars are computed, become larger as well as larger is the covariance matrix.

This demonstrates the noise correction can not be neglected.

6.2.3 Declination correction

One of the systematic effects present in NVSS data is the declination correction (see Chap. 4). As seen before, [Blake & Wall, 2002] say the flux cuts lower than ~ 10 mJy are affected by an artificial declination problem. All the maps used in the previous analyses are corrected for this systematic. However we prove how the declination correction influences the estimates by using a 10mJy flux cut map not corrected for declination. In Fig. 6.11 the \hat{C}_ℓ^{GG} and \hat{C}_ℓ^{TG} are shown.

The estimates for TG and GG are very similar because the 10mJy flux cut is not influenced by declination correction, this confirms the statement by [Blake & Wall, 2002]. The other two lower flux cuts (2.5 and 5.0 mJy, mainly

affected by the systematic) which are corrected for declination are consistent with the 10.0mJy flux cut (considering both the results in Figs 6.9 and 6.11). Then it is very important to consider the declination correction in the analysis of the NVSS data.

Hereafter all the maps are corrected for declination and with the short noise removed.

6.2.4 $C_\ell^{TG} \neq 0$ effect on the cross-power spectrum

In the previous chapter we demonstrated the Monte Carlo simulations converge on the fiducial model which characterizes the maps when the $C_\ell^{TG} = 0$ and when $C_\ell^{TG} \neq 0$. Then we choose the $C_\ell^{TG} = 0$ in order to make the computation less heavy.

Here we want to check that the $C_\ell^{TG} \neq 0$ also gives the same estimates of the $C_\ell^{TG} = 0$ case, seen above for the 2.5mJy flux cut. In Fig. 6.12, it is evident the estimates given by $C_\ell^{TG} \neq 0$ (the thin error bars shifted of $\ell = +1$ to the right) are very similar to the previous one. It seems we can be confident on the estimates give by $C_\ell^{TG} = 0$.

6.3 Galaxy distribution model with $b(z)$

In this section we show the estimates obtained using a fiducial model given by CENSORS galaxy distribution presented in Chap. 5 and taking into account the bias dependence on the redshift.

In Fig. 6.13 we compare the estimates for the 2.5mJy flux cut of NVSS.

It is clear how the C_ℓ^{GG} estimates for the [de Zotti et al., 2010] model is more confident to the fiducial model with respect to the previous [Ho et al., 2008] model, although the C_ℓ^{TG} estimates do not change very much.

As the shot noise issue, also the bias characterization (in particular its dependence on the redshift) results very important in the galaxy power spectrum estimation.

Note that the estimates never change in the two models, we confirm the QML implementation is not strongly dependent on the fiducial model.

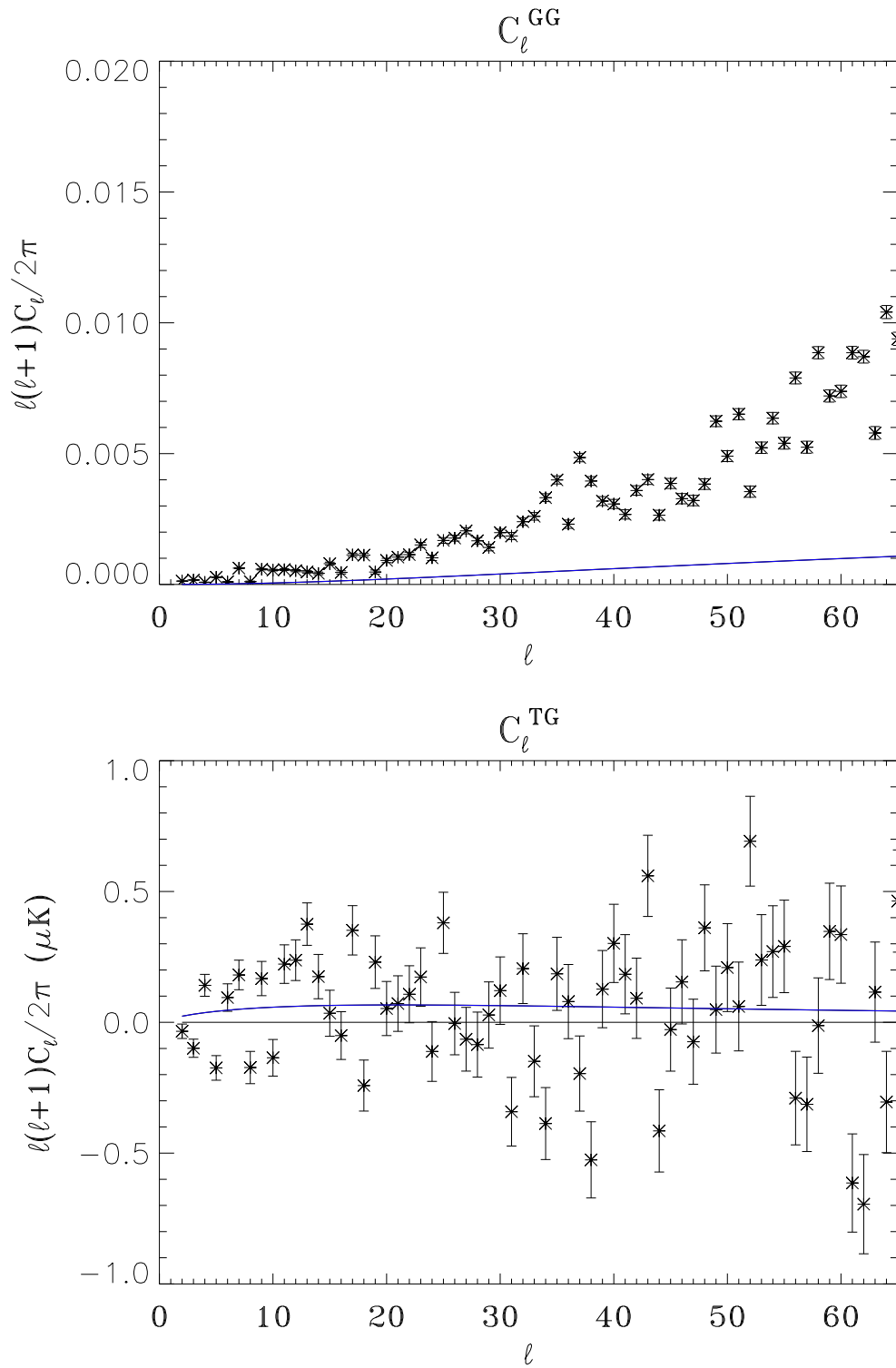


Figure 6.2: Unbinned C_ℓ^{GG} auto spectrum and C_ℓ^{TG} cross spectrum for 2.5mJy flux cut in NVSS, without removing the shot noise.

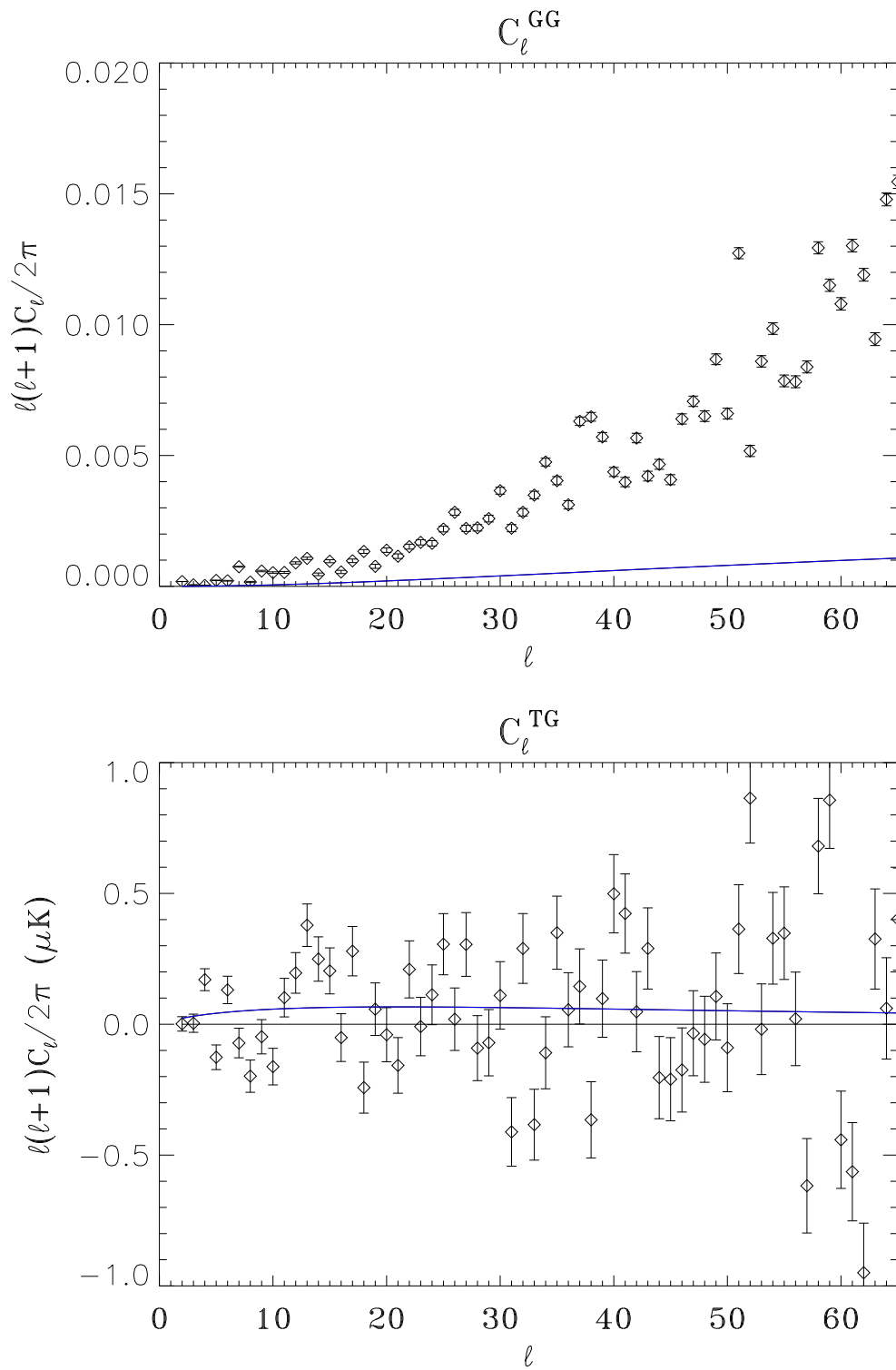


Figure 6.3: Unbinned C_ℓ^{GG} auto spectrum and C_ℓ^{TG} cross spectrum for 5mJy flux cut in NVSS, without removing the shot noise.

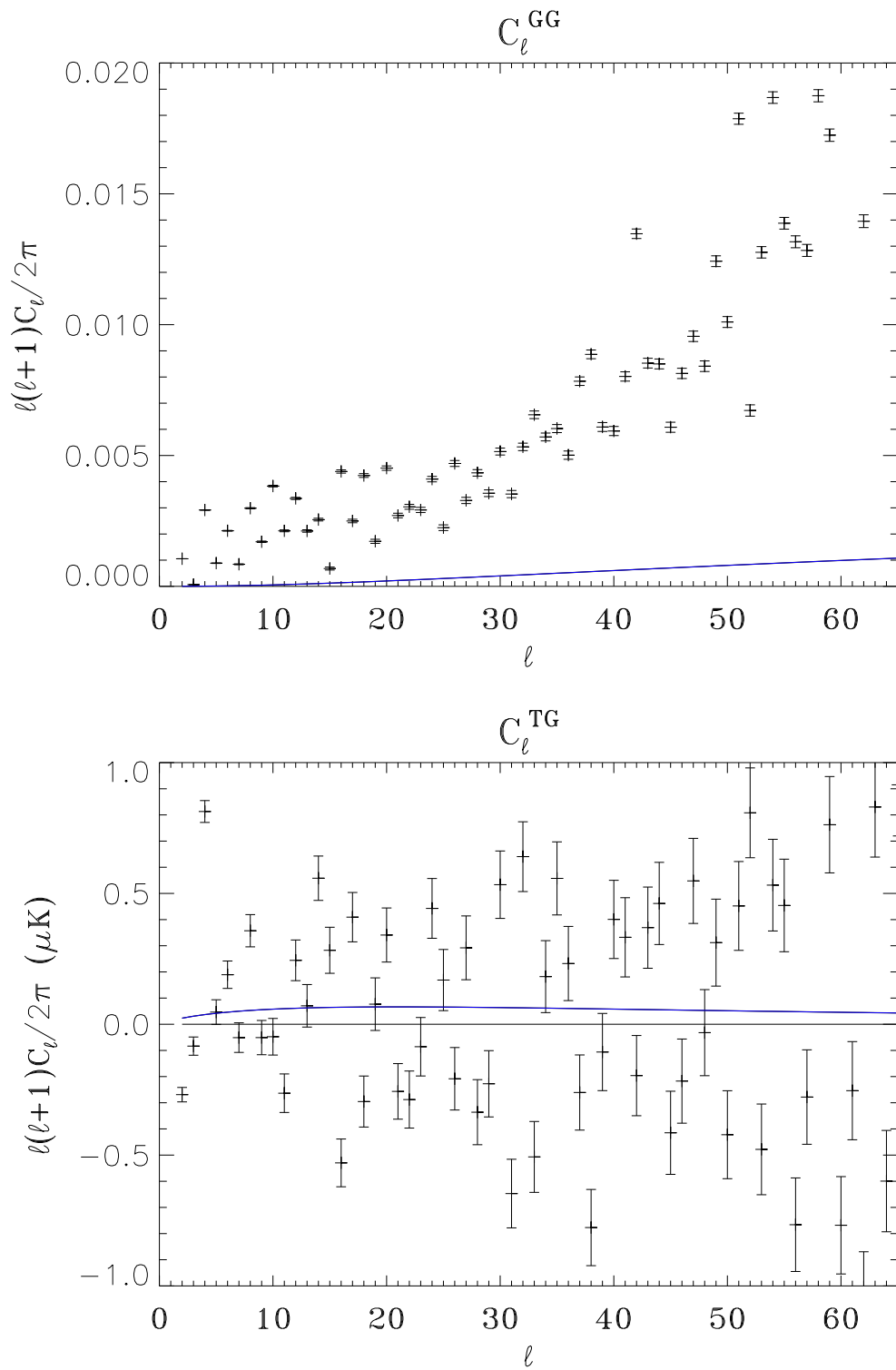


Figure 6.4: Unbinned C_ℓ^{GG} auto spectrum and C_ℓ^{TG} cross spectrum for 10mJy flux cut in NVSS, without removing the shot noise.

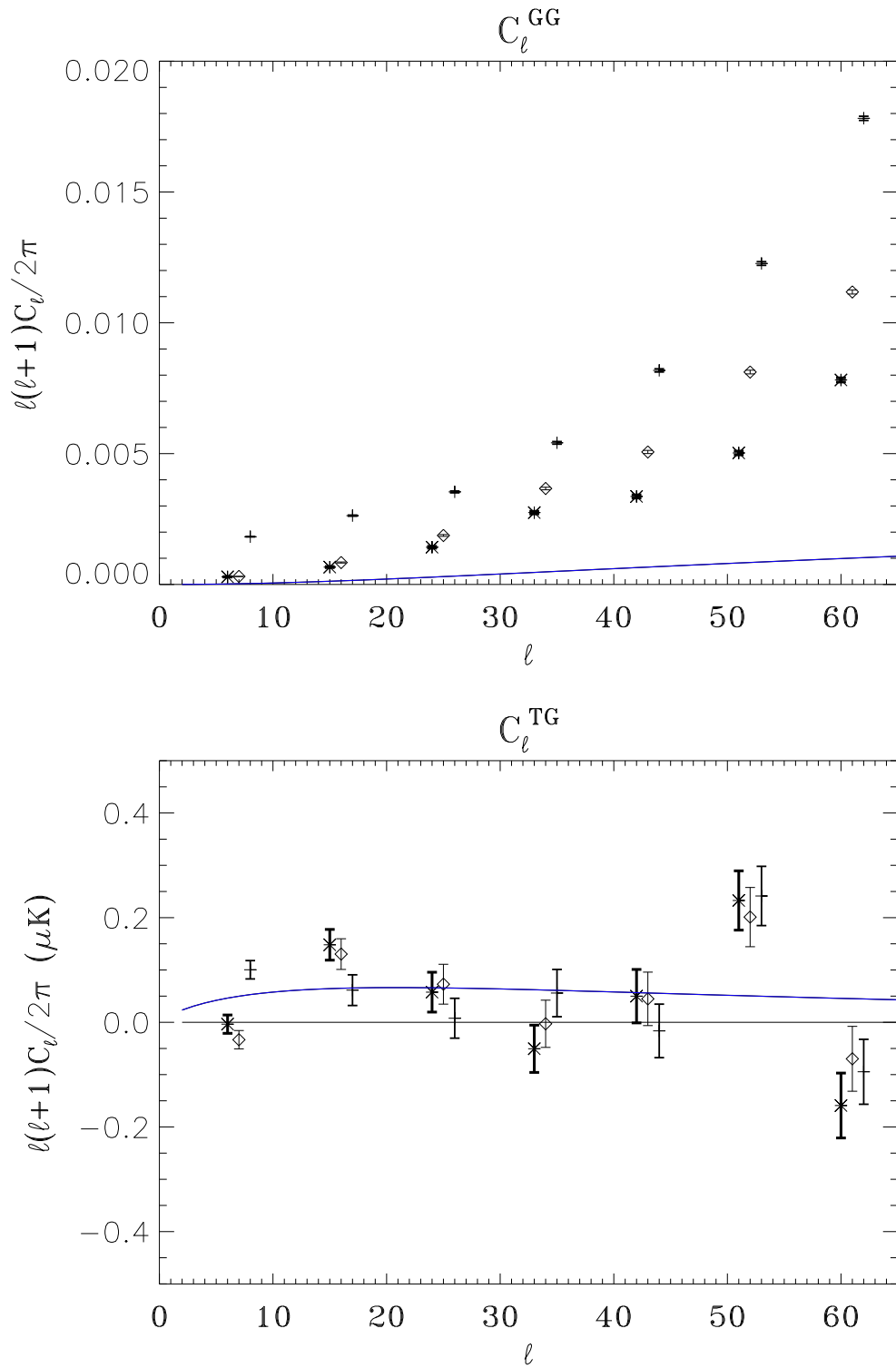


Figure 6.5: Binned comparison between C_ℓ^{GG} auto spectrum and C_ℓ^{TG} cross spectrum for all the three flux cuts, without removing the shot noise.

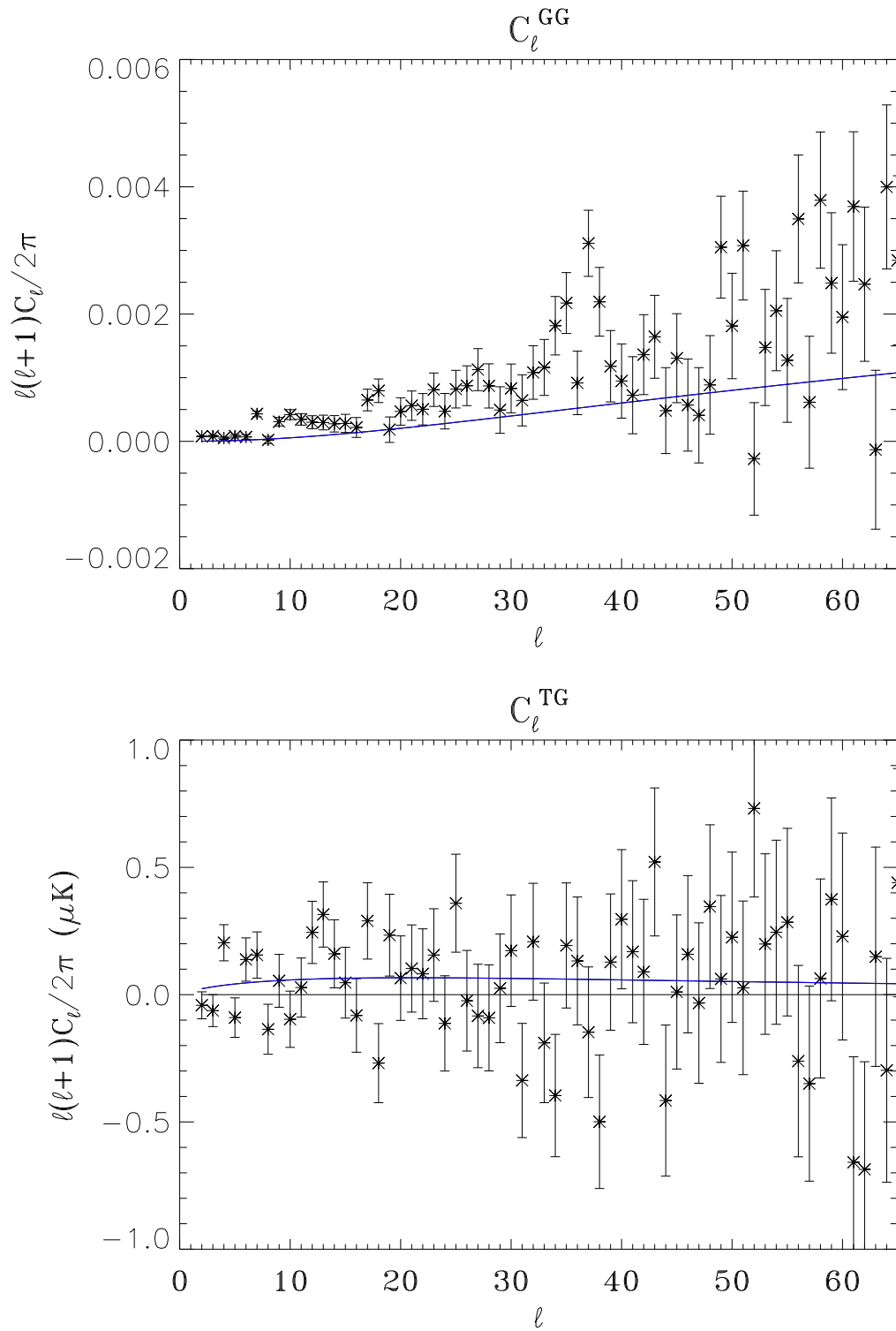


Figure 6.6: Unbinned C_ℓ^{GG} auto spectrum and C_ℓ^{TG} cross spectrum for 2.5mJy flux cut in NVSS, with the shot noise removed.

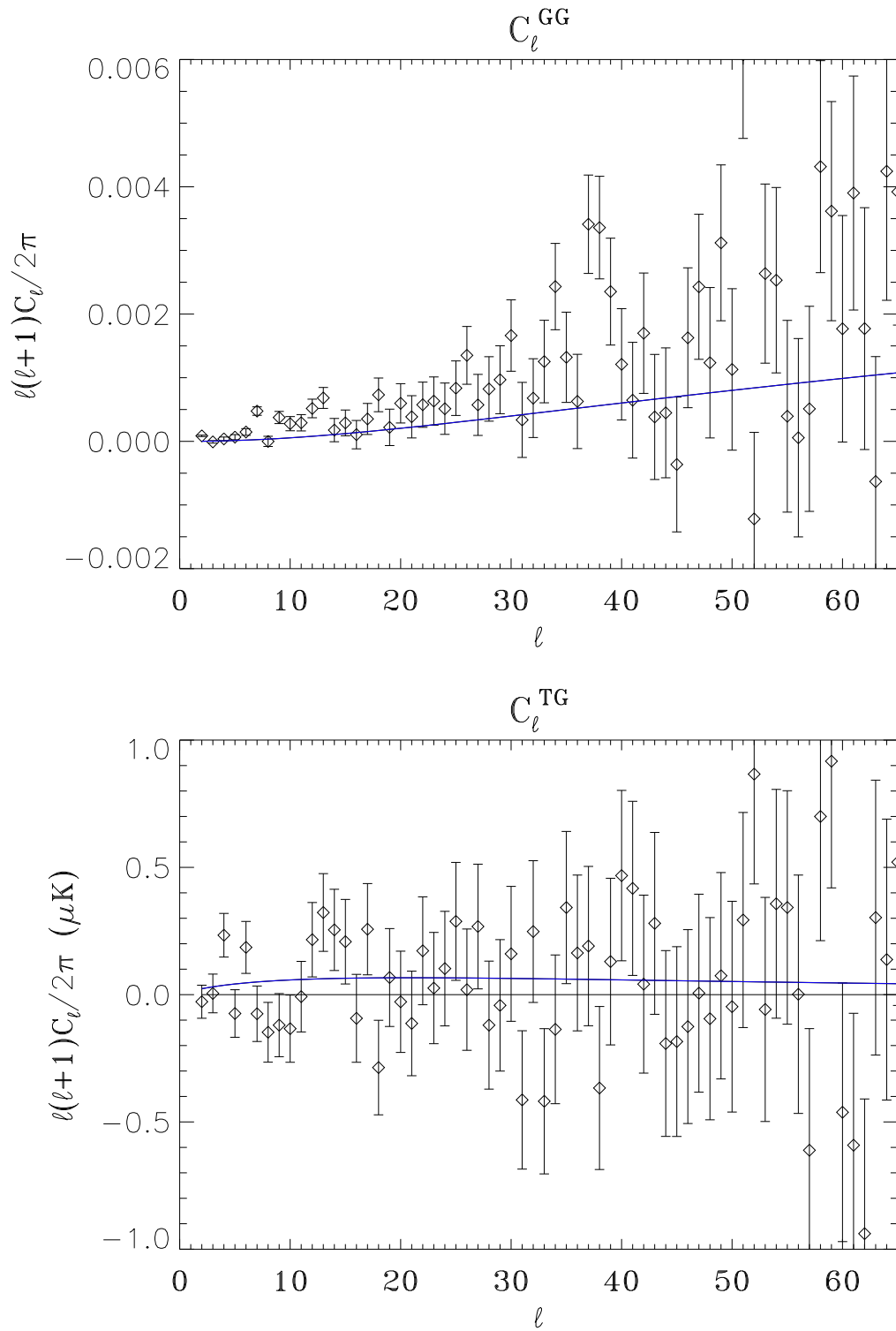


Figure 6.7: Unbinned C_ℓ^{GG} auto spectrum and C_ℓ^{TG} cross spectrum for 5mJy flux cut in NVSS, with the shot noise removed.

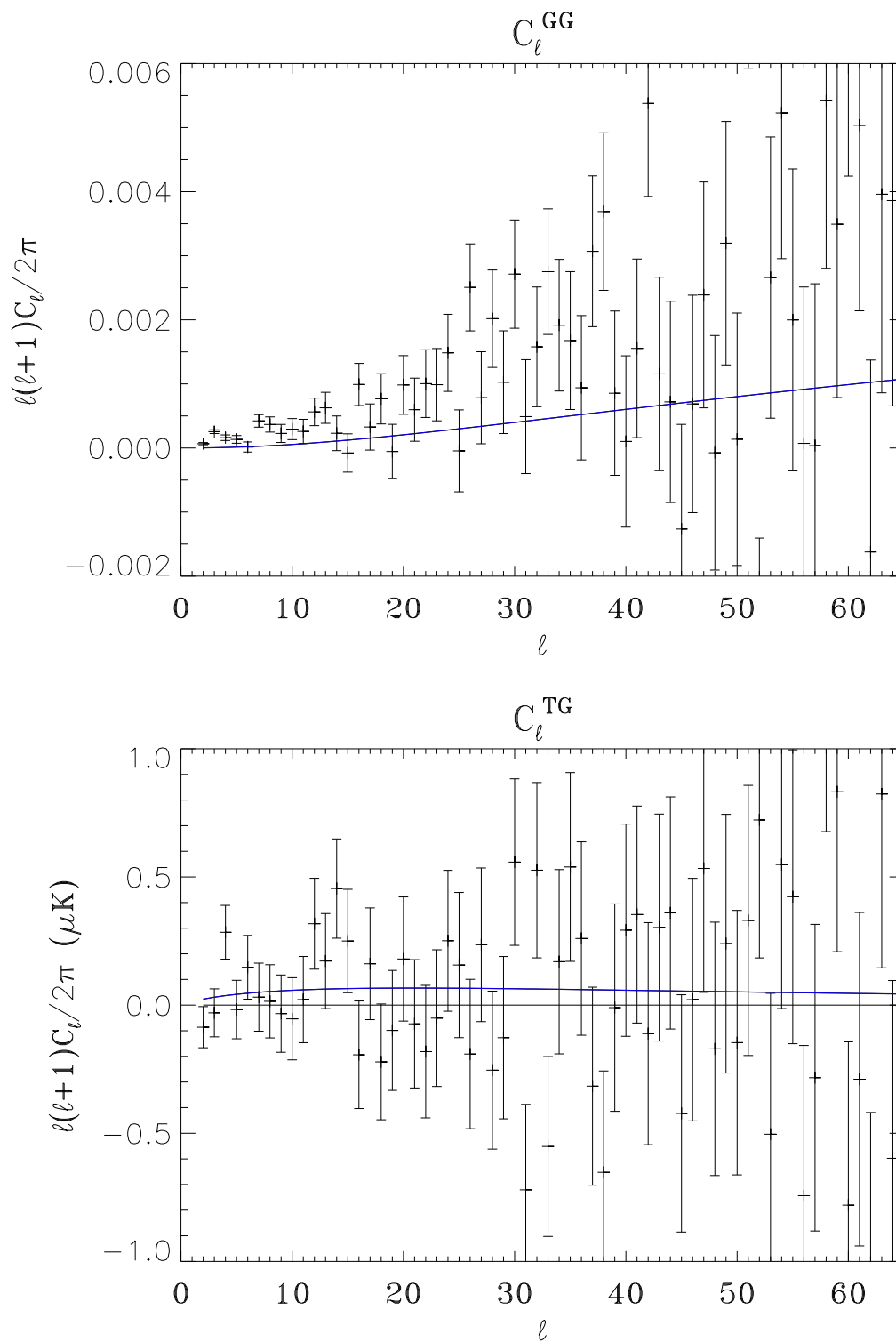


Figure 6.8: Unbinned C_ℓ^{GG} auto spectrum and C_ℓ^{TG} cross spectrum for 10mJy flux cut in NVSS, with the shot noise removed.

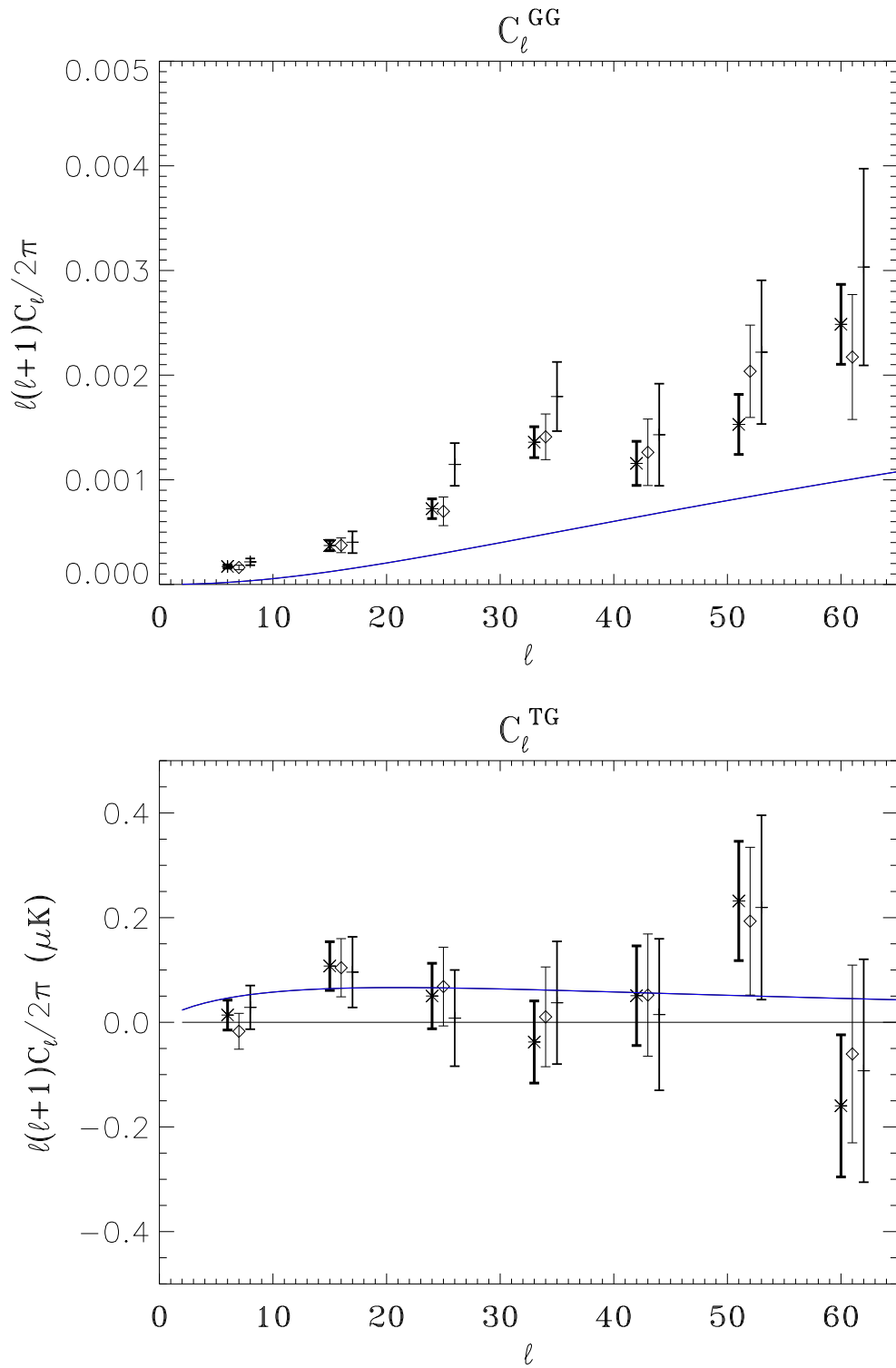


Figure 6.9: Binned comparison between C_ℓ^{GG} auto spectrum and C_ℓ^{TG} cross spectrum for all the three flux cuts, with the shot noise removed.

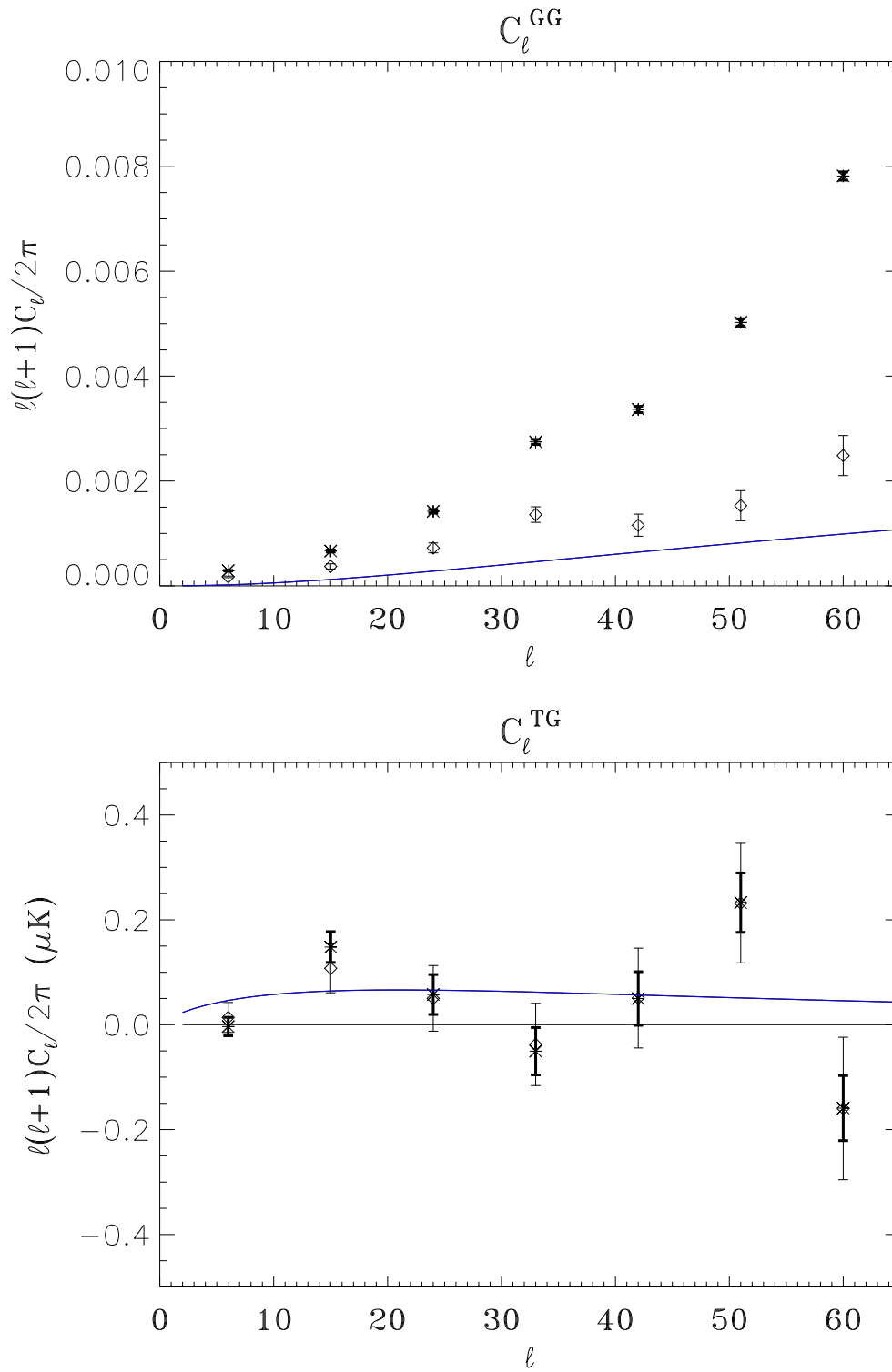


Figure 6.10: Binned C_ℓ^{GG} auto spectrum and C_ℓ^{TG} cross spectrum estimates for 2.5mJy flux cut, where we compare the two cases with (points with thin error bars) and without removing the shot noise (points with thick error bar).

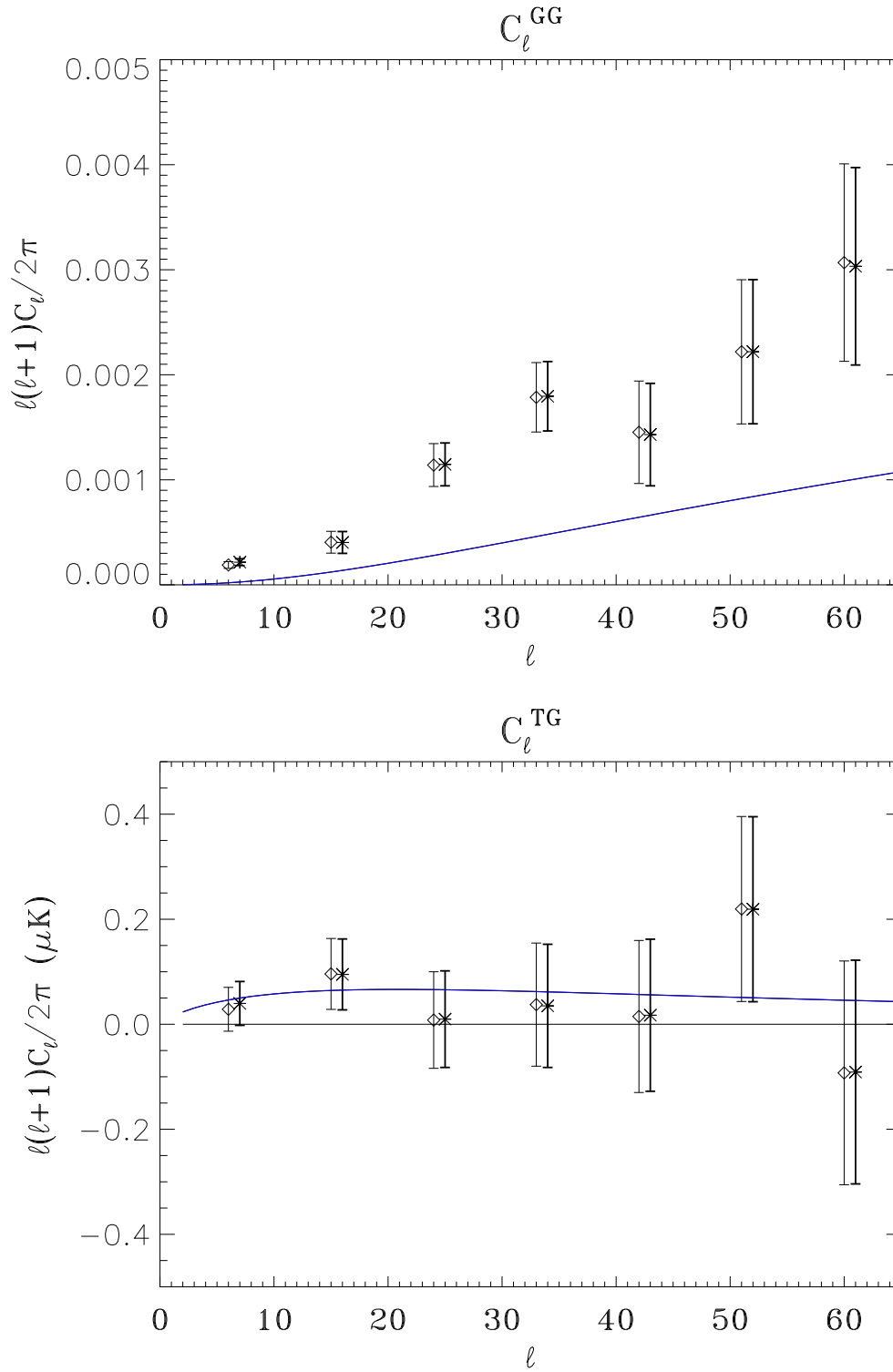


Figure 6.11: Binned C_ℓ^{GG} auto spectrum and C_ℓ^{TG} cross spectrum estimates for 10mJy flux cut, where we compare the two cases with (points with thin error bars) and without declination correction applied to NVSS map (points with thick error bar).

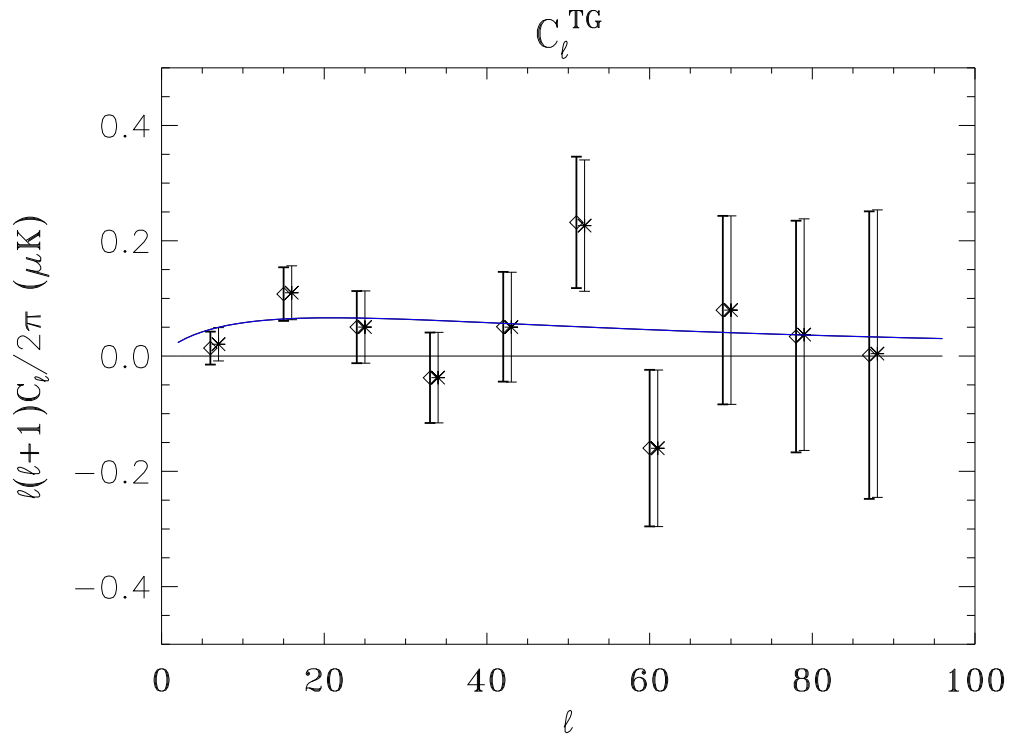


Figure 6.12: Binned C_ℓ^{GG} auto spectrum and C_ℓ^{TG} cross spectrum estimates for $2.5mJy$ flux cut, where we compare the two cases with the fiducial $C_\ell^{TG} \neq 0$ (points with thin error bars) and with the fiducial $C_\ell^{TG} = 0$ (points with thick error bar).

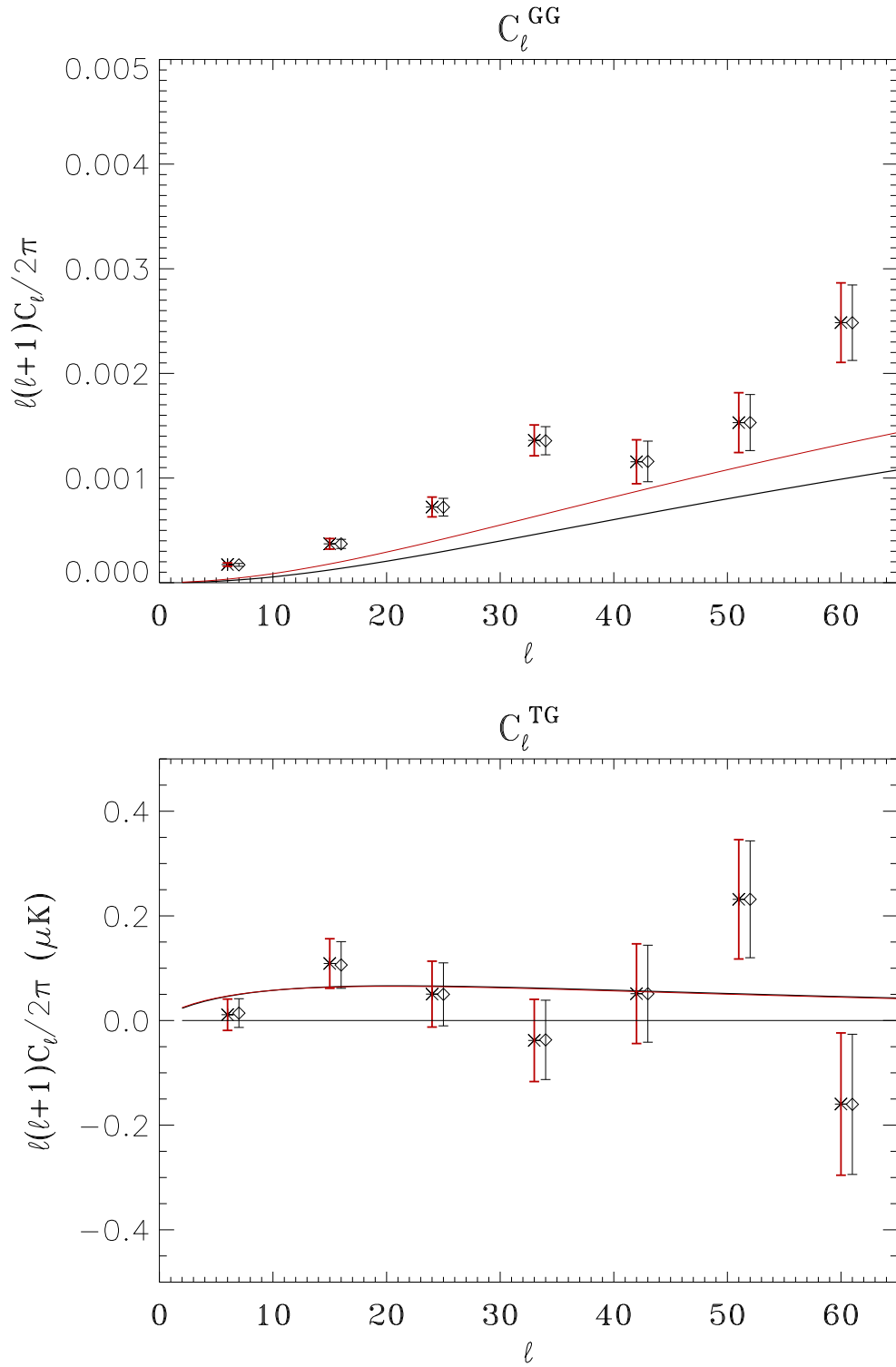


Figure 6.13: Binned C_ℓ^{GG} auto spectrum and C_ℓ^{TG} cross spectrum estimates for $2.5mJy$ flux cut. We compare the two galaxy distribution model with constant b (black curve and points) and with $b(z)$ (red curve and points).

Chapter 7

Quantitative assessment of the cross-correlation detection

In this chapter, we constrain the Dark Energy density parameter Ω_Λ using the information contained in the ISW-LSS cross-correlation power spectrum, estimated through our QML.

7.1 Likelihood computation

In order to obtain this constraint we sample the χ^2 on 20 values of Ω_Λ , $0 < \Omega_\Lambda < 0.95$, with steps of 0.05. We assume the errors on the measured C_ℓ^{TG} are Gaussian and calculate the relative likelihoods of Ω_Λ using

$$-2 \ln[\mathcal{L}(\Omega_\Lambda)] = \chi^2(\Omega_\Lambda) - \chi_{\min}^2. \quad (7.1)$$

where

$$\chi^2(\Omega_\Lambda) = \left[C_\ell^{TG, \text{obs}} - C_\ell^{TG}(\Omega_\Lambda) \right] \mathbf{C}_{\ell\ell'}^{-1}(\Omega_\Lambda) \left[C_{\ell'}^{TG, \text{obs}} - C_{\ell'}^{TG}(\Omega_\Lambda) \right]. \quad (7.2)$$

Here $C_\ell^{TG, \text{obs}}$ are the unbinned estimates of the cross-correlation power spectrum, and $C_\ell^{TG}(\Omega_\Lambda)$ are the theoretical predicted power spectrum. The matrix $\mathbf{C}_{\ell\ell'}$ is the covariance matrix between different ℓ 's, which allows for correlations among non-diagonal terms which arise in the presence of masks. χ_{\min}^2 is the minimum value of χ^2 with respect to Ω_Λ .

We compare the likelihoods obtained by different prescriptions for the covariance matrix. The first prescription is to use the *unbinned* QML estimates and the Fisher matrix as its covariance matrix:

$$\mathcal{C}_{\ell\ell'}^F = (F^{-1})_{\ell\ell'}^{TGTG}. \quad (7.3)$$

An alternative prescription is to construct the covariance matrix \mathcal{C} by averaging over Monte Carlo realisations of the maps. For every model Ω_Λ , we can define the covariance \mathcal{C} with N simulated CMB and LSS maps

$$\mathcal{C}_{\ell\ell'}(\Omega_\Lambda) = \sum_{i=0}^N \frac{[C_{\ell,i}^{TG}(\Omega_\Lambda) - \bar{C}_\ell^{TG}(\Omega_\Lambda)][C_{\ell',i}^{TG}(\Omega_\Lambda) - \bar{C}_{\ell'}^{TG}(\Omega_\Lambda)]}{N}, \quad (7.4)$$

where the $C_{\ell,i}^{TG}$ are the estimates for every single realization i and the \bar{C}_ℓ^{TG} is their theoretical value. We assume the covariance matrix is not strongly dependent on the cosmological model, then we consider the case with $\Omega_\Lambda = 0$ ([Vielva, Martinez-Gonzalez & Tucci2006]), and since $\bar{C}_\ell^{TG}(\Omega_\Lambda = 0) = 0$, the covariance becomes,

$$\mathcal{C}_{\ell\ell'}^{MC} = \sum_{i=0}^N \frac{C_{\ell,i}^{TG} C_{\ell',i}^{TG}}{N}. \quad (7.5)$$

We build $\mathcal{C}_{\ell\ell'}$ in Eq. (7.5) either by using random realisations of only the CMB maps *and the single, true* NVSS map, or by creating a realisations of both CMB and LSS maps. In the former and latter cases, we generate results on 1000 realisations. We also examine how the probability contours for Ω_Λ depend on the various assumptions such as the threshold flux cut used for the NVSS map or the sources redshift distribution.

We evaluate the likelihood with the various different prescriptions by sampling the χ^2 on values of Ω_Λ , $0 < \Omega_\Lambda < 0.95$. The other cosmological parameters are kept fixed to the values determined by WMAP [Larson et al., 2011] for the standard Λ CDM model. As default NVSS description, the Eq. (6.1, dN^{Ho}/dz) model is assumed, with a bias of 1.98, as previously seen in chap. 4. In order to compare the three prescriptions we use the the lowest flux threshold of 2.5 mJy, as it is shown in 7.1.

7.2 Results

By adopting the Fisher matrix prescription (solid black line) in Eq.7.3, we obtain $\Omega_\Lambda = 0.69_{-0.22}^{+0.15} (0.23)_{(0.50)}$ at 1(2) σ confidence level (CL).

An Einstein-de Sitter Universe is disfavoured at more than 2 σ CL for the lowest flux threshold in NVSS, consistent with earlier measurements.

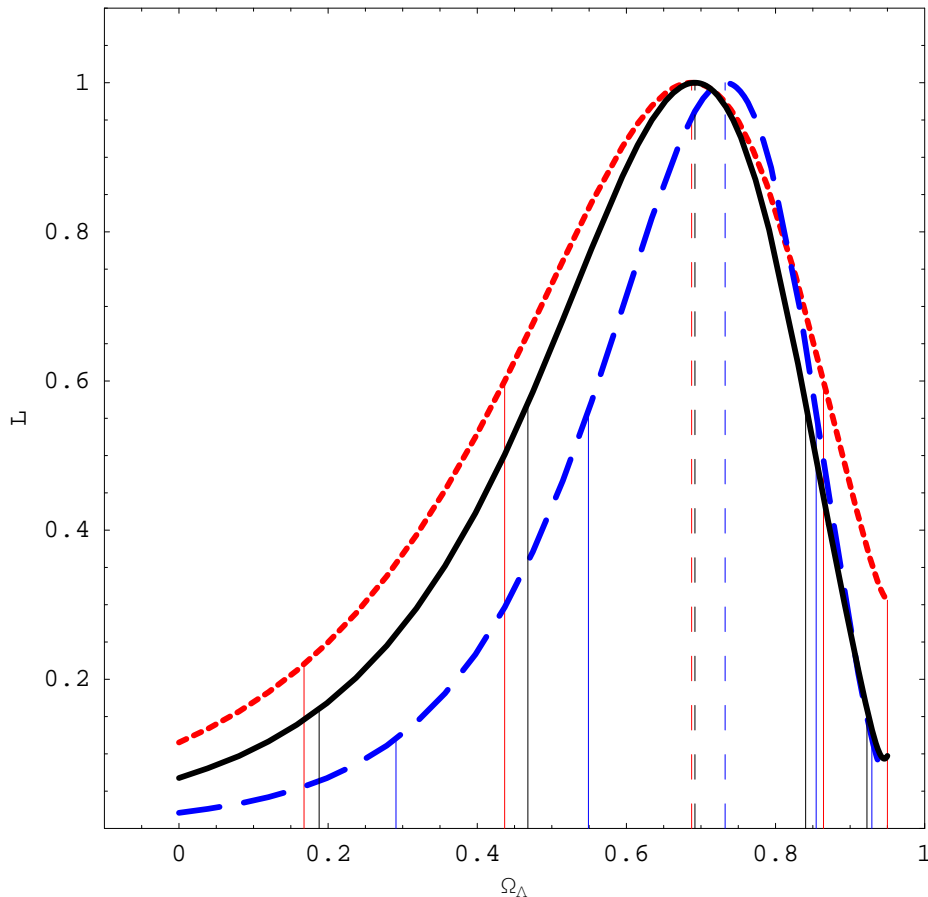


Figure 7.1: Comparison of likelihood contours for Ω_Λ obtained by the Fisher prescription (black solid line), the covariance computed by the Monte Carlo for CMB only (red short dashed line) and for both CMB and LSS (blue dashed line). The threshold flux in NVSS has been chosen to be 2.5 mJy.

By building the covariance through realizations of the CMB maps while keeping the NVSS map fixed, we obtain the probability distribution given by the red dashed line of Fig. 7.1. We find $\Omega_\Lambda = 0.69^{+0.18(0.26)}_{-0.25(0.52)}$ at $1(2)\sigma$ CL. On the other hand, by using the covariance derived from realizations of both CMB and LSS maps, the probability distribution given by the blue dashed line of Fig. 7.1 we find $\Omega_\Lambda = 0.73^{+0.12(0.18)}_{-0.20(0.44)}$ at $1(2)\sigma$ CL. Note that the constraint based on the Fisher covariance is tighter than the one based on a Montecarlo covariance keeping fixed the NVSS map, but looser than the Montecarlo covariance obtained with CMB and LSS uncorrelated maps. Overall, the agreement between the three likelihood prescriptions is good.

Given the agreement among the three different likelihood prescriptions, the Fisher one can be used for the covariance to test other dependences of the analysis, because the Fisher is tightly linked to the QML analysis. It takes into account the estimates errors, influencing the width of the likelihood.

The first step is to compare the conditional probabilities of Ω_Λ for the three different flux thresholds considered, see in Fig. 7.2. The blue line is the 2.5mJy flux cut with Ω_Λ the same as above; the red line is the 5mJy flux cut with $\Omega_\Lambda = 0.62^{+0.18(0.27)}_{-0.28(0.56)}$ at $1(2)\sigma$ CL; the black line is the 10mJy flux cut with $\Omega_\Lambda = 0.77^{+0.17(0.18)}_{-0.30(0.564)}$ at $1(2)\sigma$ CL. As expected from the Fisher algebra, it is evident the estimates with the larger error bars have also the wider likelihood. The 2.5mJy case is the tightest one. In agreement with the power spectrum C_ℓ^{TG} estimates, the tightest constraints we obtain on Ω_Λ gives credit to the attitude of cleaning NVSS data as much as possible from the known systematics which is proposed in our approach. In Fig. 7.3 we verify the importance of taking into account the shot-noise in the NVSS map for the 2.5mJy threshold: by not removing the shot-noise the probability contours for Ω_Λ would be much tighter (blue solid line, $\Omega_\Lambda = 0.65^{+0.10(0.23)}_{-0.12(0.48)}$ at $1(2)\sigma$ CL), because they represent an underestimate of the error in C_ℓ^{TG} , being linked with the Fisher matrix we expect in the case we remove the shot-noise the likelihood is wider, because of the larger estimates error bars (see Fig. 6.10). A careful treatment of the correction to the declination systematics and of the shot noise is essential for an optimal scientific explanation of NVSS data.

In the previous Chap. 6 we compared the 10mJy threshold maps with and without the declination correction, finding no evident differences. In Fig.7.4 we show these two cases, where the solid black line is the case without declination correction. The more evident difference is in the peak position of the likelihoods, but the shape seems not change.

We also verify how the likelihood change when the assumption $C_\ell^{TG} = 0$ is not used in the construction of the signal covariance matrix, i.e. we consider a cross-power spectrum model different from the null hypothesis. In Chap.s 5 and 6, we did not find any differences between the $C_\ell^{TG} = 0$ and $C_\ell^{TG} \neq 0$ cases, but in Fig.7.5 the red line ($C_\ell^{TG} \neq 0$) is evidently shifted and a little bit tigher than the previous case

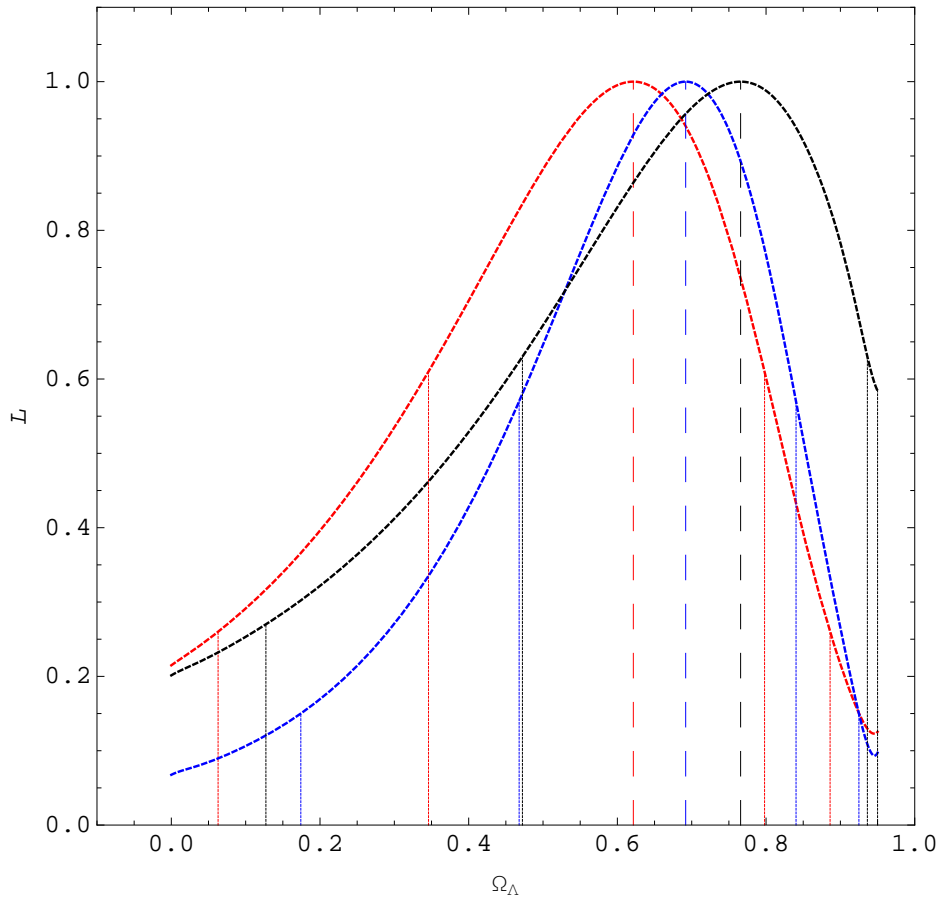


Figure 7.2: The likelihood for Ω_Λ obtained by the Fisher prescription, with the 95 % and 68 % C.L. for the threshold flux of 2.5 mJy (blue), 5 mJy (red), 10 mJy (black) in NVSS, respectively.

($C_\ell^{TG} = 0$).

In the last two analyses we showed how much a very small difference in the estimates and error bar values can be amplified in the likelihood analysis.

In Fig. 7.6 we compare the redshift distribution estimated with CENSORS data by [de Zotti et al., 2010] in Eq. (4.3) with the one adopted by [Ho et al., 2008], considering for the latter a bias dependent from redshift $b(z)$ and for the former a constant bias $b = 1.98$ as an effective bias.

The tightest constraint obtained is $\Omega_\Lambda = 0.73^{+0.12(0.20)}_{-0.18(0.44)}$ at $1(2)\sigma$ confidence level (CL) for the lowest flux threshold of 2.5 mJ and using covariances based on Monte Carlo of both CMB and LSS. This result agrees with that expected from a typical survey with sky fraction and noise property as the NVSS, and agrees

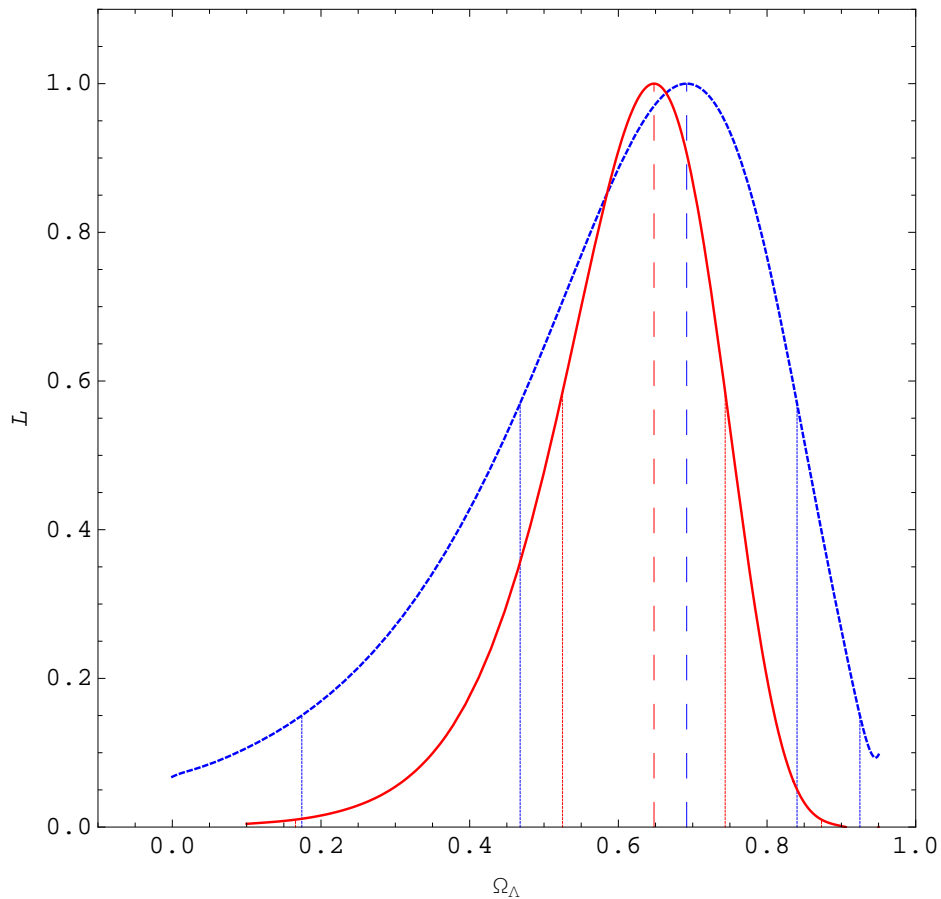


Figure 7.3: Comparison of likelihood contours for Ω_Λ obtained by the Fisher prescription when accounting (blu line) and when not accounting (red line) for shot noise in NVSS data. The threshold flux in NVSS has been chosen as 2.5 mJ.

with [Vielva, Martinez-Gonzalez & Tucci2006], but is somewhat weaker than the one obtained by the non-optimal analysis by [Pietrobon, Balbi and Marinucci, 2006] based on needlets. It is not clear if this discrepancy is due to the lower resolution considered here or the neglect of shot-noise in the NVSS map in the analysis by [Pietrobon, Balbi and Marinucci, 2006].

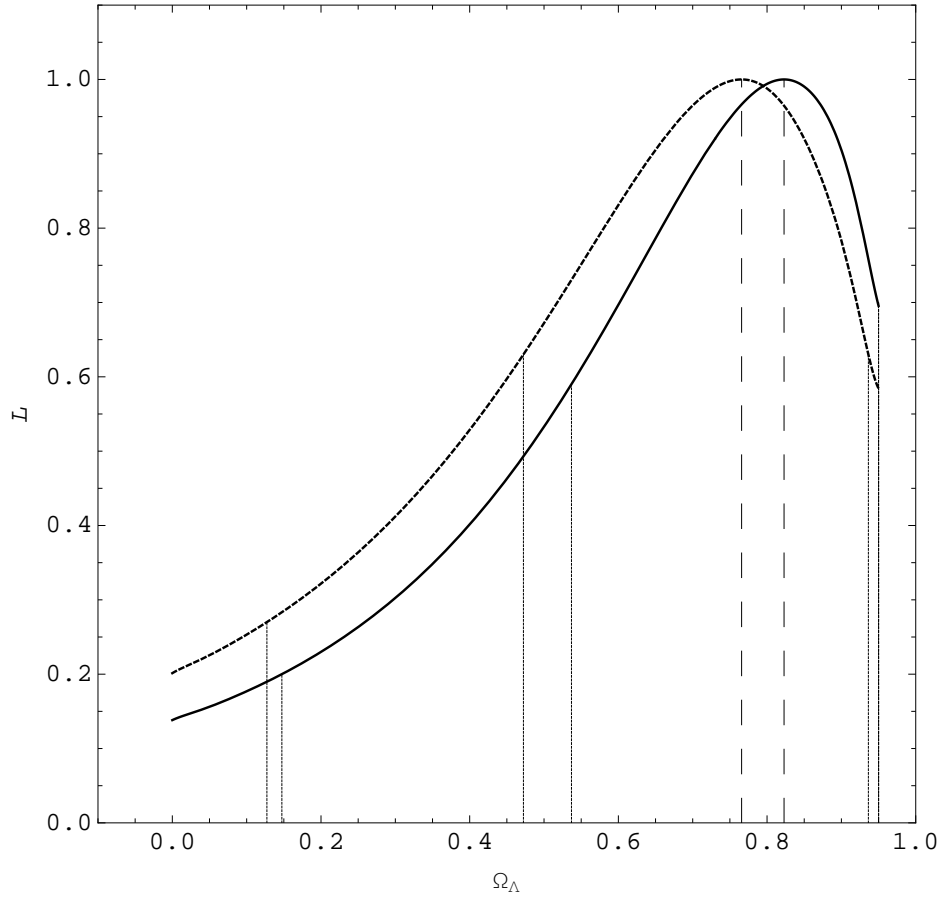


Figure 7.4: Comparison of likelihood contours for Ω_Λ obtained by the Fisher prescription when accounting (dashed black line) and when not accounting (continue black line) for the declination correction in NVSS data for the $10mJy$ flux cut.

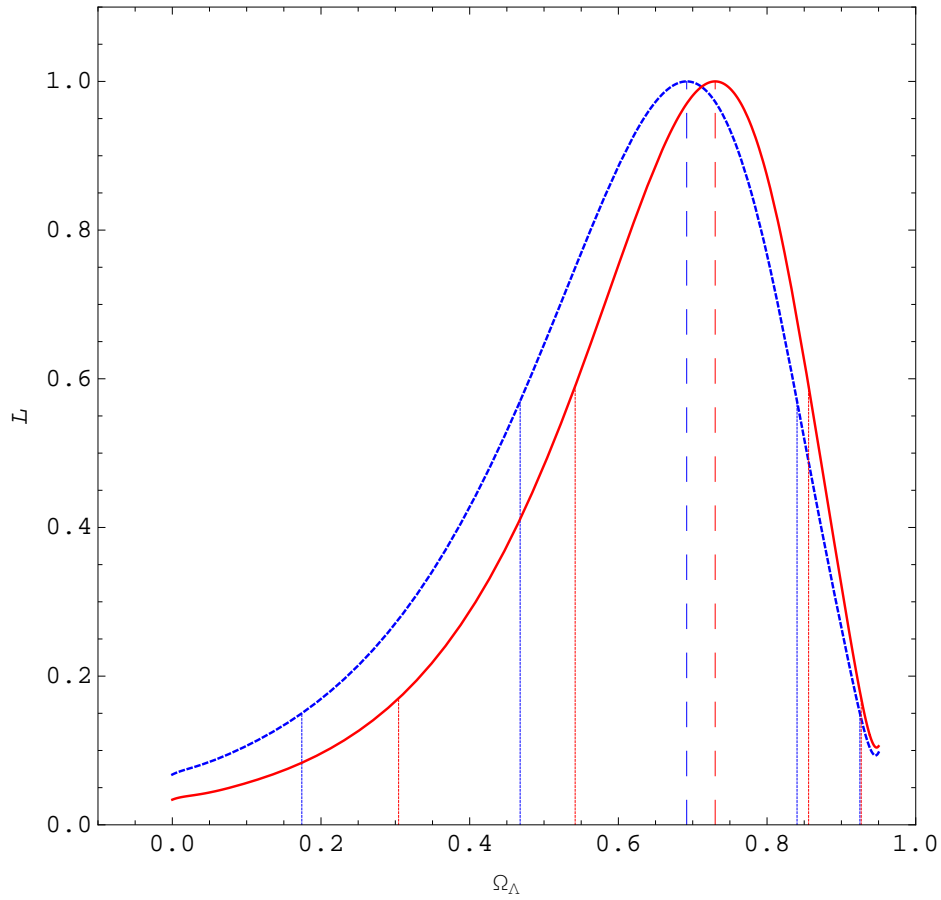


Figure 7.5: Comparison of likelihood contours for Ω_Λ obtained by the Fisher prescription when considering the full covariance (red solid line) and when using the approximation of a block diagonal signal covariance and Fisher matrix. The threshold flux in NVSS has been chosen as 2.5 mJ.

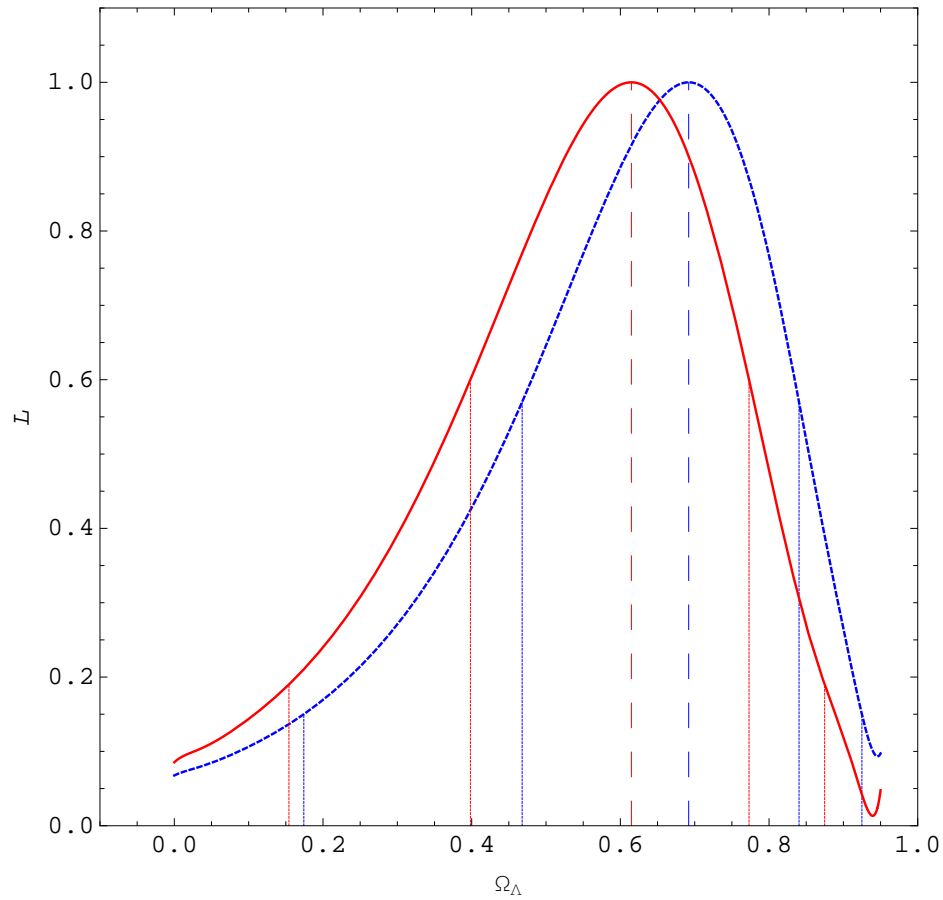


Figure 7.6: Comparison of likelihood contours for Ω_Λ obtained by the Fisher prescription for the two choices of redshift distributions: solid for $b(z)$ and dashed for b constant. The threshold flux in NVSS has been chosen as 2.5 mJ.

Conclusions

The CMB fluctuations created by the late Integrated Sachs-Wolfe effect is one of the key indicators of the presence of the Dark Energy and since [Crittenden & Turok1995], the cross-correlation is the powerful method to detect it. In 2002, Boughn and Crittenden published the first attempt of detecting the ISW effect considering the cross-correlation between COBE data and XRB and NVSS data, but in that case the detection was null mainly because of the poor resolution and sensitivity of COBE map even at large scales. Since then, many papers (see for example [Dupé et al, 2011] and references therein for an excellent compilation of available results) analysing the detection of the ISW effect have been published, considering the cross-correlation between CMB anisotropies and LSS surveys, as suggested by Crittenden and Turok (1996). In this thesis we have developed an optimal estimator for the angular power spectrum of the cross-correlation ISW-LSS, which also estimates their auto-spectra. This has been tested using an ensemble of randomly generated maps, and we have demonstrated the optimal properties of our QML implementation, as the robustness of the estimates for the TT, TG and GG power spectra. The cross-correlation between CMB and LSS can be computed with different methods in the harmonic domain or considering the Wavelet expansion, but none of these method is optimal as a QML, which works in the pixel domain.

We have applied our method to WMAP 7 year and NVSS data, the best public data sets at present for studying the ISW cross-correlations. Our method makes no assumptions, and allows to measure the power spectrum of cross-correlation with minimum variance errors and to exploit the full cosmological information contained in the maps, though our analysis is limited to a pixel resolution of 1.8° .

We detect a non-zero cross-correlation, and have also seen a slight excess in the NVSS auto-angular power spectrum compared to what usually is the theoretical prediction. The estimates are fully consistent with the previous

results in the literature ([Blake, Ferreira & Borril, 2004]). We have translated these measurements into the quantitative constraints on the fraction of Dark Energy in a Λ CDM model which can be obtained only by the cross-correlation of WMAP and NVSS, estimating Ω_Λ while keeping fixed all the other cosmological parameters to the WMAP 7 yr best-fit values [Larson et al., 2011]. We have compared three different prescriptions for estimating the covariances: using the Fisher matrix computed by our QML, on Monte Carlo realisations of the CMB maps keeping NVSS fixed and creating Monte Carlo realisations of both CMB and LSS maps. We have found a good agreement among the Ω_Λ probability contours obtained from these three different likelihood prescriptions.

WMAP data is already signal dominated at the relevant angular scales and therefore what is important for the ISW detection is the goodness of the LSS maps that can be characterized by the sky coverage and the full redshift coverage of the Dark Energy dominated era. We have used three different flux cuts for NVSS maps and we have learnt the accurate description of the noise and systematics present on the LSS maps are very important issues to consider. We have corrected for the NVSS declination systematics and found that these corrections are important only when considering flux thresholds below 10mJy, confirmed by in literature [Blake & Wall, 2002]; considering the angular power spectrum technique, the shotnoise of the LSS map impacts not only the auto-spectrum GG but also the cross-spectrum TG , mainly in terms of error bars associated to the estimates. As a consequence, we found an impact on the width of the likelihood of Ω_Λ and therefore on the significance of the ISW detection. This means that the shotnoise present in the galaxy maps cannot be neglected in the ISW analysis even if it is based on the TG spectrum.

The QML is well suited for the ISW-LSS cross-correlation detection not only because it is an optimal estimator and therefore provides unbiased APS estimates with the smallest error bars allowed by the Fisher-Cramer-Rao inequality, but also because thanks to the built-in capabilities of performing Monte Carlo simulations it makes possible to deeply test and keep under control the LSS maps including their noise characterization. The width of this probability contour depends mainly on the flux threshold and associated level of Poisson noise in the NVSS map, but the signal amplitude seems largely independent of the flux. We have found $\Omega_\Lambda = 0.69^{+0.15(0.23)}_{-0.22(0.52)}$

at $1(2)\sigma$ C.L., a statistical significance for Ω_Λ close to 3σ with a simplified likelihood, by significantly correcting NVSS for its declination systematics and by estimating carefully its shot noise.

This result is to add to all the other ISW detection in Tab. 3.1 of [Dupé et al, 2011].

Most ISW detections reported in Tab. 3.1 are relatively ‘weak’ ($< 3\sigma$), but the some of the higher detections are reported for the NVSS survey [Pietrobon et al. 2006, McEwan et al. 2007, Giannantonio et al. 2008]; they found statistical significances for Ω_Λ , respectively, $> 4\sigma$, $> 2.5\sigma$ and 3.3σ , all consistent with our result.

This thesis includes important international collaborations. R. G. Crittenden (University of Portsmouth, UK) and Patricio Vielva, Enrique Martínez-González and Belen Barreiro (University of Cantabria, Spain) participate to the first application of the optimal QML to WMAP 7 year and NVSS data.

This Ph.D. activities has led to a powerful methodology which has several new and interesting applications.

- In order to consider the whole cosmological information (expected on theoretical ground) included in the cross-correlation power spectrum we plan to extend our analysis to larger multipoles by using a map resolution of $N_{side} = 64$. Afshordi N. 2004, in Fig. 7.7, shows that the enclosed area for the region covered by a survey, multiplied by its sky coverage f_{sky} , gives the optimum $(S/N)^2$ for the cross-correlation ISW-LSS signal. At $\ell > 100$ the signal slowly dies out, but it is not null. Going to higher multipoles allows to take into account all the signal expected.
- In conjunction with the imminent WMAP 9 year final release we plan to consider the CMB cross-correlation with the following LSS maps, taking advantage of ISW-LSS Planck working group :
 - Luminous Red Galaxies (LRG) from Sloan Digital Sky Survey (SDSS) III (<http://www.sdss3.org>)
 - Quasars from SDSS III (<http://www.sdss3.org>)
- In order to obtain a self-consistence estimate of parameters we plan to include in the likelihood analysis a straightforward GG auto-spectrum contribution. In this way it will be possible to estimate not only the Ω_Λ parameter but also

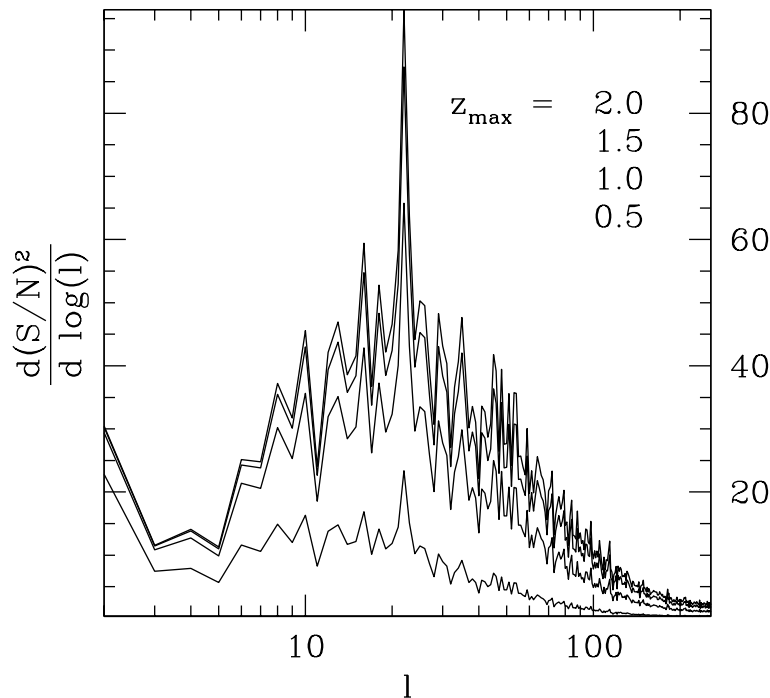


Figure 7.7: $(S/N)^2$ distribution with respect to multipoles.

the galaxy bias. As we have seen in the Chap. 6, the galaxy bias depends on redshift. We plan to use slices of galaxy maps, in order to take into account the redshift dependence of the bias.

As for the analysis of the cross-correlation WMAP 7 - NVSS, the best likelihood prescription will be applied to the three cross-correlation between WMAP 9 year data and the above mentioned data and will be added to the WMAP 9 year one, whose likelihood code will be delivered at the same time of the scientific results and data at the public site <http://lambda.gsfc.nasa.gov/>, as for the previous releases. It is customary to add independently the LSS likelihood to the CMB one to mainly break the degeneracy between the cold dark matter density Ω_m and the Hubble parameter H_0 and have therefore better constraints on all the cosmological parameters (see for instance Finelli et al. 2010 for the impact of the constraints obtained with LRG from SDSS Data Release 7 - i.e. SDSS II - in combination with CMB data on the cosmological parameters). A further step would be to include the cross-correlation between CMB and

LSS self-consistently in the full likelihood: with the robustness achieved in [Schiavon et al., 2012] in the CMB-LSS CC angular power spectrum estimation and likelihood, we are in the position to include such contribution to the full likelihood and discuss the cosmological implications for current data. To our knowledge, this would be the first analysis of this kind. Once published we might also release publicly the modified Markov Chain Monte Carlo COSMOMC and the cross-correlation WMAP-LSS data.

- It has been suggested that the CMB polarization information could increase of the 20 % the SNR encoded in the ISW-LSS cross-correlation (Crittenden 2006, Frommert & Ennslin, 2009). The inclusion of polarization to a pure CMB QML estimator has been already handled successfully (Gruppuso et al. 2009). However, the inclusion of polarization would double the dimensionality of the problem at the map level (from T, G to T, Q, U, G being Q, U the Stokes parameters) and quadruplicate it at the level of covariances. The QML computational time scaling would prohibit the possibility of unbinned estimates from maps at the required angular resolution. To tackle this issue it would be therefore necessary to develop a binned version of the QML code. Such binning procedure would also be useful for the current temperature QML code to increase the angular resolution of the maps (now limited to $N_{\text{side}} = 64$) currently handled by our QML and investigate multipoles $\ell \geq 150 - 200$.

Appendix A

Fisher matrix

In the QML algebra the Fisher matrix is an important component since its inverse matrix provides the smallest error bars allowed by the Fisher-Cramer-Rao inequality 5. The following figures visualize the Fisher matrix.

In order to understand why we do not use the total matrix inversion but the inversion of the blocks (both in the covariance matrix and in the Fisher one), as it is explained in Chap. 5, note the large difference in the order of magnitudes among the blocks of the Fisher matrix. The TT×TT block is of the order of $\sim 10^{-5}$ with respect to the $\sim 10^8$ orders of the GG × GG block.

This matrix inversion trick can be used both when the matrices - \mathbf{C} or \mathbf{F} - are full (fiducial $C_\ell^{TG} \neq 0$ case) and when they are not (fiducial $C_\ell^{TG} = 0$ case). In the latter case, the two matrices \mathbf{C} and \mathbf{F} are also block diagonal, then it is possible to invert their diagonal blocks independently.

The Fisher matrix is directly computed by fiducial power spectra, then the shot noise removal influences the matrix. The differences are very small and not visible in the Fisher matrix visualization.

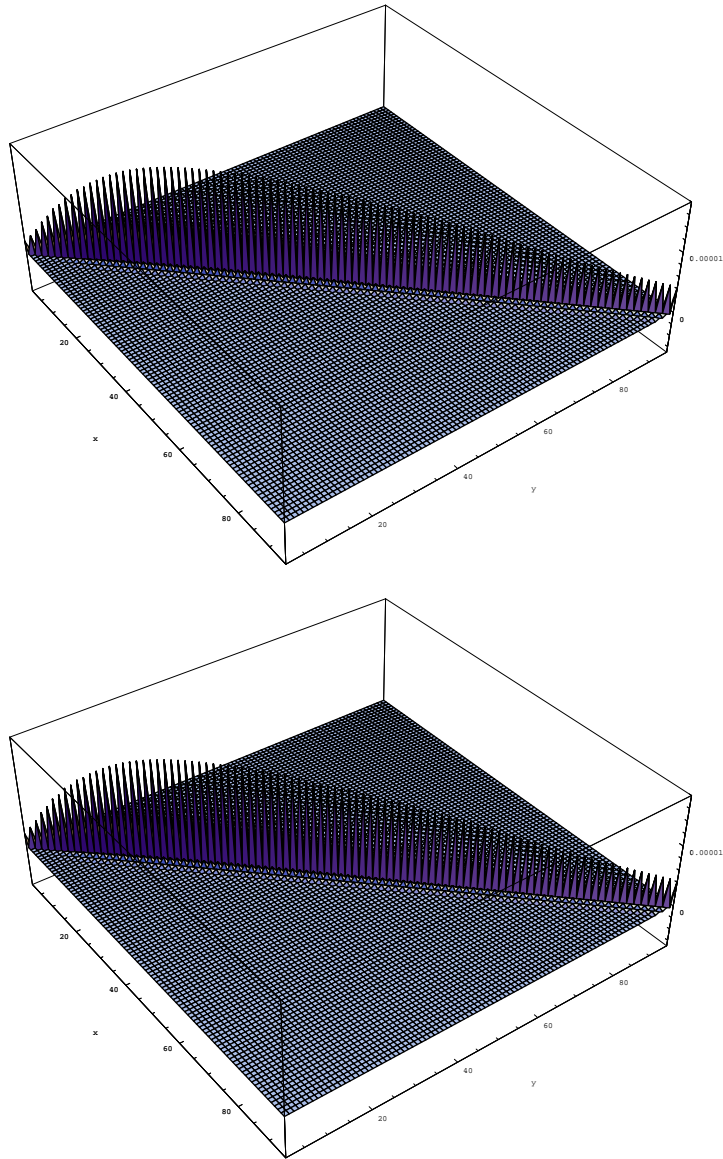


Figure A.1: The Fisher matrix block $TT \times TT$ in two cases: the up panel is the case when the fiducial $C_\ell^{TG} = 0$ and the bottom one is the case $C_\ell^{TG} \neq 0$.

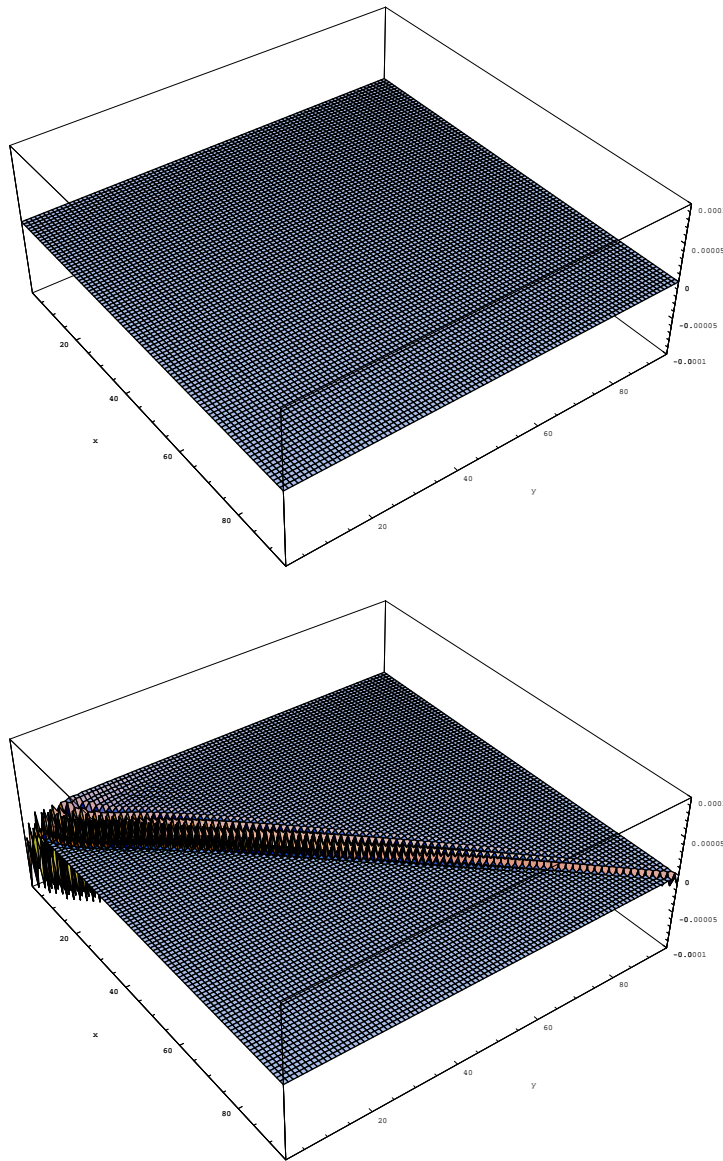


Figure A.2: The Fisher matrix block $\text{TT} \times \text{TG}$ in two cases: the up panel is the case when the fiducial $C_\ell^{TG} = 0$ and the bottom one is the case $C_\ell^{TG} \neq 0$.

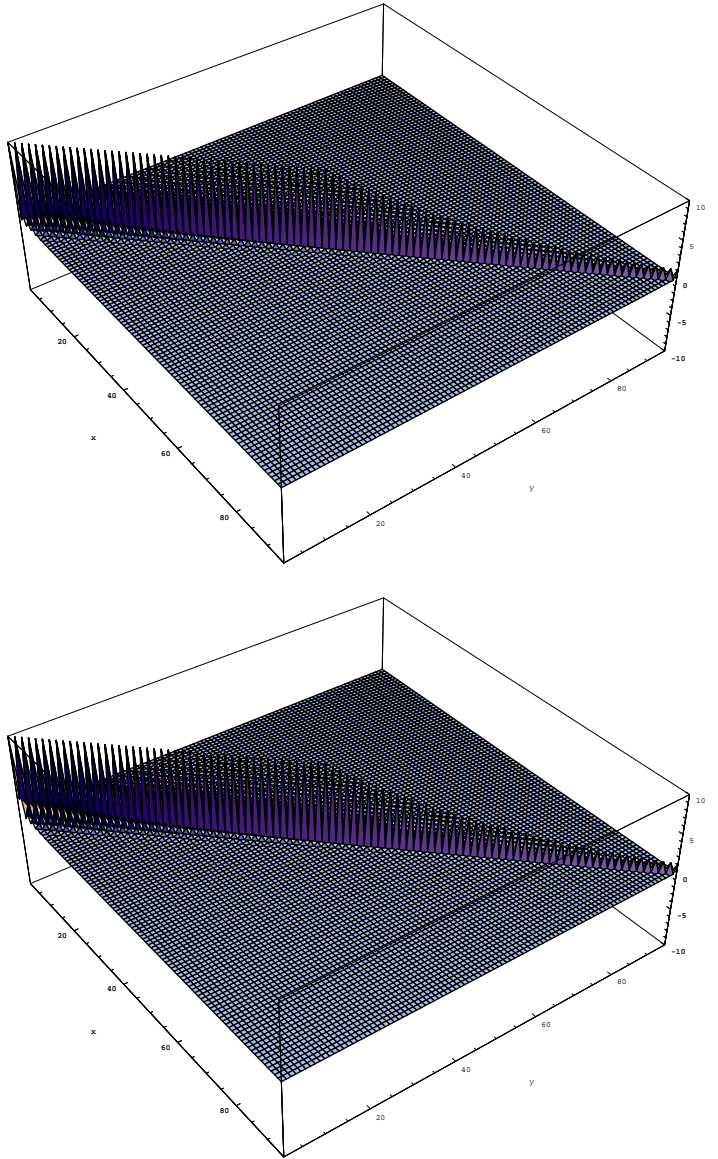


Figure A.3: The Fisher matrix block $TG \times TG$ in two cases: the up panel is the case when the fiducial $C_\ell^{TG} = 0$ and the bottom one is the case $C_\ell^{TG} \neq 0$. This block is not null when the fiducial $C_\ell^{TG} = 0$ since it is computed by the fiducials C_ℓ^{TT} and C_ℓ^{GG} .

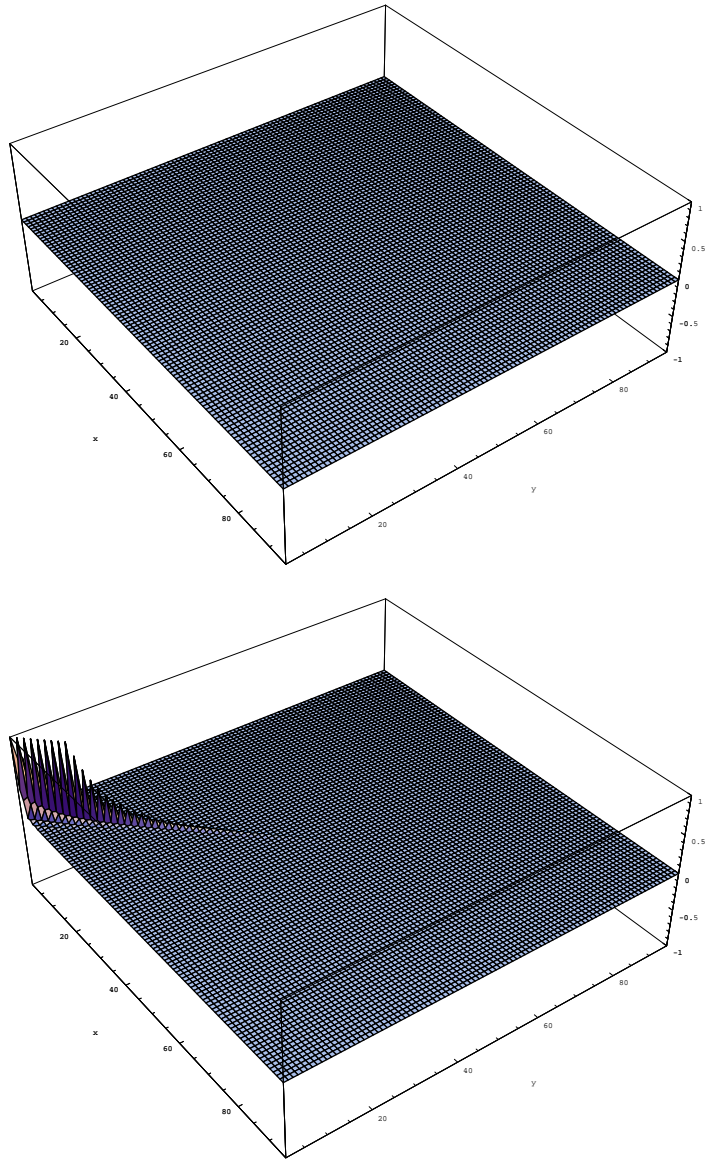


Figure A.4: The Fisher matrix block $TT \times GG$ in two cases: the up panel is the case when the fiducial $C_\ell^{TG} = 0$ and the bottom one is the case $C_\ell^{TG} \neq 0$

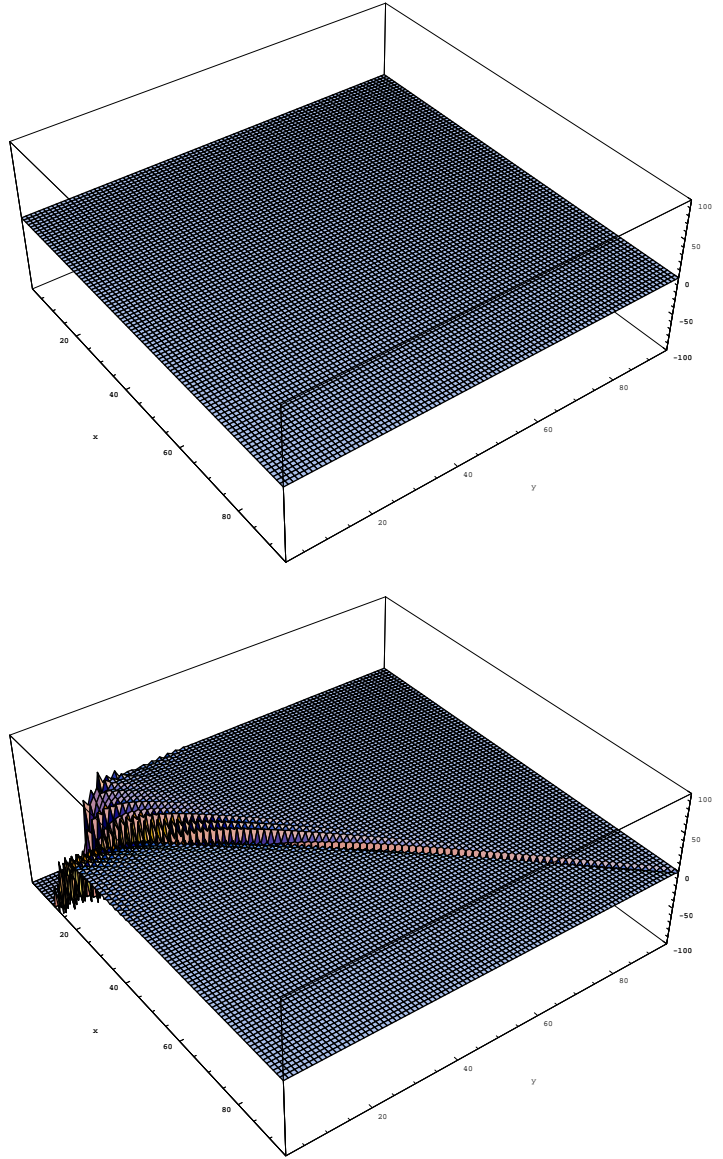


Figure A.5: The Fisher matrix block $TG \times GG$ in two cases: the up panel is the case when the fiducial $C_\ell^{TG} = 0$ and the bottom one is the case $C_\ell^{TG} \neq 0$.

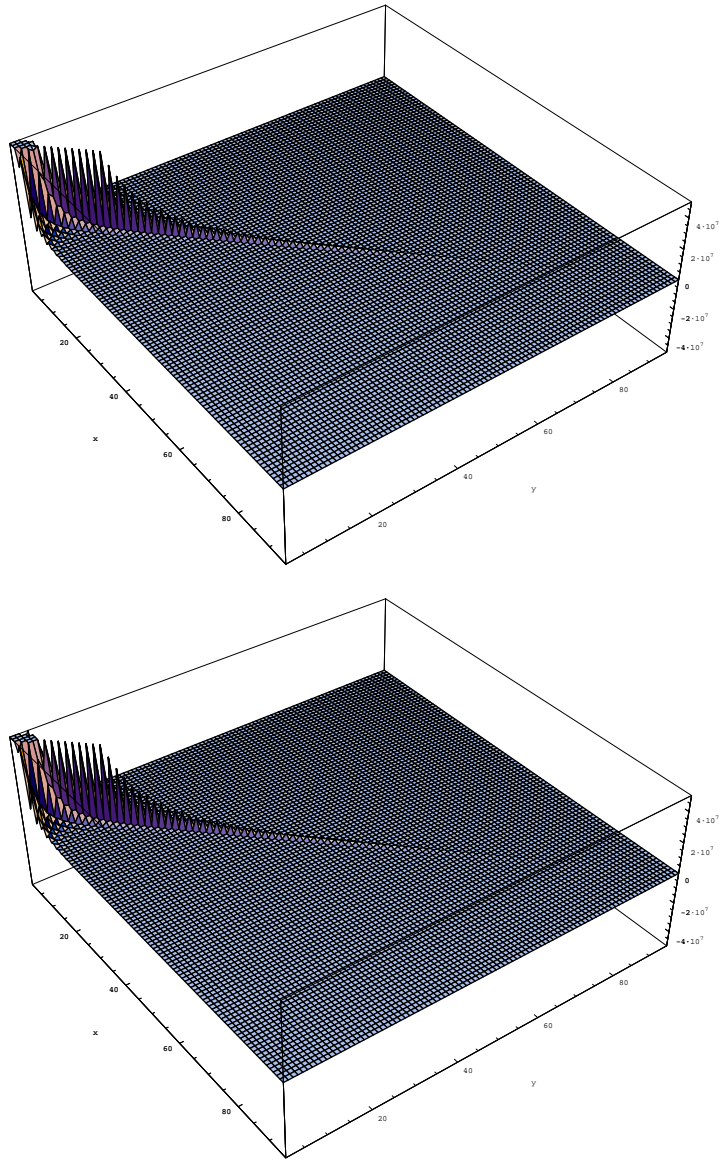


Figure A.6: The Fisher matrix block $GG \times GG$ in two cases: the up panel is the case when the fiducial $C_\ell^{TG} = 0$ and the bottom one is the case $C_\ell^{TG} \neq 0$.

Bibliography

- [Afshordi, Loh & Strauss2004] N. Afshordi, Y. S. Loh and M. A. Strauss, Phys. Rev. D **69** (2004) 083524
- [Alpher & Herman, 1998] Alpher R., Herman R., 1948 1948Natur.162..774A
- [Abramo, Finelli & Pereira, 2004] Abramo R.L., Finelli F. Pereira S., 2004 Phys. Rev. D **70**, 063517
- [Barreiro et al., 2008] Barreiro R. B., Vielva P., Hernandez-Monteagudo C., and Martínez-González E., 2008 IEEE Journal of Selected Topics in Signal Processing 2, 747
- [Bento et al, 2004] Bento, Maria C.; Bertolami, Orfeu; Sen, Anjan A. 2005tmgm.meet.1776B
- [Birkinshaw & Gull, 1983] Birkinshaw M, Gull SF. 1983. *Nature* 302:315–317
- [Blake, Ferreira & Borrill, 2004] Blake, C., Ferreira, P. G., Borrill, J., Mon. Not. Roy. Astron. Soc. 351, 923 (2004)
- [Blake & Wall, 2002] Blake, C. & Wall, J., Mon. Not. Roy. Astron. Soc. **329**, 37 (2002)
- [Boughn & Crittenden, 1998] Boughn, S. P., Crittenden, R. G., and Turok, N. G. New Astron. **3**, (1998) 275
- [Boughn & Crittenden, 2002] Boughn S. P. and Crittenden R. G., Phys. Rev. Lett. **88** (2002) 021302
- [Boughn & Crittenden2004] Boughn S. P., Crittenden R. G., 2004, Nature, **427**, 6969, 45

- [Brookes et al., 2008] Brookes, M. H., Best, P. N., Peacock, J. A., Rottgering, H. J. A., Dunlop, J. S., *Mon. Not. Roy. Astron. Soc.* **385**, 1297 (2008)
- [Buras et al., 1978] Buras A.J., Ellis J., Gaillard M.K., Nanopoulos D.V. (1978). *Nuclear Physics B* 135 (1): 66–92
- [Carroll et al., 1992] Carroll S.M., Press W.H., Turner E.L., 1992, *ARA&A*, 30, 499
- [Condon et al., 1998] Condon J. J., Cotton W. D., Greisen E. W., Yin Q. F., Perley R.A., Taylor G. B. and Broderick J. J., *Astron. J.* **115** (1998) 1693.
- [Corasaniti et al., 2005] Corasaniti, P., Gannantonio, T., Melchiorri, A., 2005, *Phys. Rev. D* **71** (2005) 123521
- [Crittenden & Turok1995] Crittenden R. G. and Turok N., *Phys. Rev. Lett.* **76** (1996) 575
- [Crittenden, 2006] Crittenden R.G., 2006 *Cosmology, Galaxy Formation and Astroparticle Physics on the pathway to the SKA*
- [Curto et al., 2011] Curto, A., Martínez-González, E., Barreiro, R. B., Hobson, M. P., 2011, *Mon. Not. Roy. Astron. Soc.* in press
- [de Bernardis et al, 2000] de Bernardis P, Ade PAR, Bock JJ, Bond JR, Borrill J, et al. 2000. *Nature* 404:955–959
- [de Zotti et al., 2010] de Zotti, G., Massardi, M., Negrello, M., Wall, J., 2010, *The Astronomy and Astrophysics Review* 18, 1.
- [Doroshkevich et al, 1978] Doroshkevich AG, Zel'Dovich YB, Sunyaev RA. 1978. *Soviet Astronomy* 22:523
- [Dunlop & Peacock, 1990] Dunlop J. S., Peacock J. A., *Mon. Not. Roy. Astron. Soc.* **247**, 19 (1990)
- [Dupé et al, 2011] Dupé F.X., Rassat A., Starck J.L., Fadili M.J. *A&A* , 534, A51+, 2011
- [Giannantonio et al., 2008] Giannantonio T., Scranton R., Crittenden R. G., Nichol R. C., Boughn S. P., Myers A. D. and Richards G. T., 2008

- [Gold et al.2011] Gold B. et al., *Astrophys. J. Suppl.* **192** (2011) 15
- [Gorski et al., 2005] Gorski K. M., Hivon E., Banday A. J., Wandelt B. D., Hansen F. K., Reinecke M. and Bartelmann M., 2005, *Ap.J.*, 622, 759-771
- [Gruppuso et al., 2009] Gruppuso A., De Rosa A., Cabella P., Paci F., Finelli F., Natoli P., De Gasperis G., Mandolesi N., *Mon. Not. Roy. Astron. Soc.* **400**, 1 (2009)
- [Gruppuso et al., 2011] Gruppuso A. et al., *Mon. Not. Roy. Astron. Soc.* **411**, 3 (2011)
- [Gunn & Peterson, 1965] Gunn JE, Peterson BA. 1965. *ApJ* 142:1633–1636
- [Guth & Pi, 1985] Guth AH, Pi SY. 1985. *Phys. Rev. D* 32:1899–1920
- [Fixen & Mather, 2002] Fixen D.J., Mather J.C. 2002. *ApJ* 581:817-822
- [Hawking, 1982] Hawking SW. 1982. *Phys. Lett.* B115:295–297
- [Ho et al., 2008] Ho S., Hirata, C., Padmanabhan, N., Salijak, U. and Bahcall N. A., *Phys. Rev. D* **78**, 043519 (2008).
- [Hu & Sugiyama, 1996] Hu W, Sugiyama N. 1996. *ApJ* 471:542–570
- [Kamionkowski et al, 1994] Kamionkowski M, Spergel DN, Sugiyama N. 1994. *ApJ* 426:L57–L60
- [Knox, 1995] Knox L. 1995. *Phys. Rev. D* 52:4307–4318
- [Kofman & Starobinskii, 1985] Kofman LA, Starobinskii AA. 1985. *Soviet Astronomy Letters* 11:271
- [Komatsu et al., 2011] Komatsu E. et al., *Astrophys. J. Suppl.* **192** (2011) 18
- [Larson et al., 2011] Larson D. et al., *Astrophys. J. Suppl.* **192** (2011) 16
- [Lewis et al, 2000] Lewis GF, Babul A, Katz N, Quinn T, Hernquist L, et al. 2000. *ApJ* 536:623–644
- [Miller et al, 1999] Miller AD, Caldwell R, Devlin MJ, Dorwart WB, Herbig T, et al. 1999. *ApJ* 524:L1–L4

- [Nolta et al. 2004] Nolte M. R. *et al.* [WMAP Collaboration]
- [Padmanabhan et al., 2005] N. Padmanabhan, C. M. Hirata, U. Seljak, D. Schlegel, J. Brinkmann and D. P. Schneider, *Phys. Rev. D* **72** (2005) 043525
- [Peacock, 1991] Peacock JA. 1991. *MNRAS* 253:1P–5P
- [Peebles & Yu, 1970] Peebles PJE, Yu JT. 1970. *ApJ* 162:815–836
- [Percival et al, 2001] Percival W, et al. 2001. *MNRAS* In Press. [astro-ph/0105252](#)
- [Perlmutter et al.,1999] Perlmutter S. et al., *Astrophys. J.* **517** (1999) 565
- [Penzias & Wilson, 1965] Penzias AA, Wilson RW. 1965. *ApJ* 142:419–421
- [Pietrobon, Balbi and Marinucci, 2006] Pietrobon D., Balbi A. and Marinucci D., *Phys. Rev. D* **74** (2006) 043524
- [Richards, 2009] G.T. Richards et al., *Astrophys. J. Suppl.* 180 (2009) 67
- [Riess et al.1998] Riess A. et al., *Astron. J.* **116** (1998) 1009
- [Sachs & Wolfe, 1967] Sachs RK, Wolfe AM. 1967. *ApJ* 147:73–90
- [Schiavon et al., 2012] Schiavon F., Finelli F. Gruppuso A., Marcos Caballero A., Vielva P., Crittenden R.G., Barreiro R.B., Martínez González, 2012 [arXiv:submit/0436977](#)
- [Seljak & Zaldarriaga, 1999] Seljak U, Zaldarriaga M. 1999. *Phys. Rev. D* 60:043504
- [Seljak & Zaldarriaga, 2000] Seljak U, Zaldarriaga M. 2000. *ApJ* 538:57–64
- [Seljak, 1997] Seljak U. 1997. *ApJ* 482:6–16
- [Silk, 1968] Silk J. 1968. *ApJ* 151:459–471
- [Smoot et al, 1977] Smoot GF, Gorenstein MV, Muller RA. 1977. *Phys. Rev. Lett.* 39:898
- [Sunyaev & Zel'dovich, 1972] Sunyaev R, Zel'dovich Y. 1972. *Comm. Astrophys. Sp. Phys.* 4:173
- [Tegmark & de Oliveira-Costa, 2001] Tegmark M. and de Oliveira-Costa A., *Phys. Rev. D* **64** (2001) 063001

- [Tegmark, 1997] Tegmark M., Phys. Rev. D **55**, 5895 (1997)
- [Tegmark et al.2004] Tegmark M. et al., Phys. Rev. D **69** (2004) 103501
- [Vielva, Martinez-Gonzalez & Tucci2006] Vielva
P., E. Martinez-Gonzalez, M. Tucci, Mon. Not. Roy. Astron. Soc. **365**, 891
(2006)
- [Wetterich, 1988] Wetterich C., 1988, 1988NuPhB.302.668W
- [White & Hu, 1997] White M, Hu W. 1997. *A&A* 321:8–9
- [Xia et al., 2010] Xia, J.-Q., Bonaldi, A., Baccigalupi, C., De Zotti, G., Matarrese, S., Verde, L., Viel, M. 2010, JCAP, **8**, 13
- [Xia, Viel & Baccigalupi, 2010] Xia, J.-Q., Viel, M., Baccigalupi, C., 2010, Astrophys. J. **717**, L17